Seasonal signals of trace elements and stable isotopes in snow and firn at Kohnen station, Antarctica

Master thesis in course 'Marine Geosciences'

Faculty of Geosciences

Universität Bremen

Alexander Weinhart

Bremen, 1.April 2016

1st reviewer: Prof. Dr. Olaf Eisen

2nd reviewer: Dr. Torsten Bickert

TABLE OF CONTENTS

LIST OF FIGURES & TABLES

ABSTRACT

Ice cores provide several environmental archives that give us insights into the history of the climate of the earth. Stable water isotopes can be used for long term temperature trends during Holocene and young Pleistocene while trace elements indicate seasonal patterns on short term and glacials on long term scales. Nevertheless, syn- and postdepositional processes influence the originally deposited signal of those proxies. As there is lack of continuous data-based annual accumulation distribution in Antarctica, it is still not clear, how single species are deposited in snow and how the signal can be interpreted. Especially the temporal variability of deposition dependent on seasonal accumulation is a fact that needs to be unterstood. Therefore, in this master thesis we try to explain, how the deposition of proxies is coupled with accumulation and show implications for an interpretation of distinct proxy signals. For this purpose, snow profiles with a length of 50 cm were taken at four different locations, which are along a path of 40 m. The main site was sampled 41 times within a period of 53 days, while the other three locations were used as reference for spatial variance. With that setup, especially the temporal resolution was in the focus of interest. The liner were cut into distinct samples of 1 cm (0-30 cm depth) and 2 cm (30-50 cm depth) and analyzed on several trace elements (Na^+, Cl^-, NO_3^-, SO_4^{2-}, Ca^{2+}, Mg^{2+} and MSA) using a Dionex IC 2100 ion chromatograph. $\delta^{18}O$ and δ^2H measurements were conducted using cavity ring-down spectroscopy (CRDS) and an Picarro analyzer. Study area is the EPICA drill site Kohnen (75°0' S; 0°4' E) in Dronning Maud Land, Antarctica with an accumulation rate of 64 mm w.e. per year and upward tendency towards higher values.

We performed a time-depth-correlation taking recent ablation stake measurements into account and plotted the isotopic and aerosol record on the basis of an estimated accumulation distribution. We used a value of 0.5 cm a^{-1} snow per winter month which is, based on density data from the snow liner, about 1.83 mm w.e. The validity of the temporal correlation was done by conservative aerosol records of sea salt components Na^+ and Cl^-. In general, the case study reveals poor correlation between isotopic record and surface temperature on the small temporal and special scale. We observed a lack of summer signal and high dependence on short term climate fluctuations like high precipitation events during extended winter season. Nevertheless, those small scale variations cannot be seen in the isotopic record as smoothing exceeds the temporal resolution. ^2H-excess in uppermost snow layers and the trend of $\delta^{18}O$ versus δ^2H confirms high influence of evaporation and sublimation effects on the snow surface that alter the real deposition signal. The allocation of summer and winter to ice core data therefore seems to be based on a high noise influence. Furthermore we showed that local and short time intervals can drastically influence the deposited tracer signals. Wind erosion by strong wind events or squalls may highly disturb the continuous stratigraphy of snow and firn. Finally, we state the urgent need of continuous accumulation distribution in Antarctica to verify patterns shown in this thesis and carry out further observations in higher resolution.

INTRODUCTION

Background of ice core studies

Ice and snow from polar regions represent a unique archive to obtain detailed information about climatic conditions from the past. Compared to regions with high influence by local geological, biogenic or anthropogenic sources, Arctic and especially Antarctic regions provide the cleanest atmosphere on this planet because of their isolated geographical situation (LEGRAND & MAYEWSKI, 1997). Polar sites are often considered to represent global scale climate signals as large atmospheric circulation patterns transport air masses towards the poles. Additionally, the stable climatic conditions and low chemical reactivity are exceptional characteristics that make Antarctica and Greenland highly attractive for environmental research. Little amounts of natural or artificial components disturb the signals, which are incorporated from the atmosphere into the snow and ice matrix. Nevertheless, anthropogenic influences on the global climate, like air pollution from burning fossil energy sources, are detectable in polar regions as well (ETHERIDGE et al., 1996).

To obtain insights into the climate history and to profit from the continuous stratigraphy of ice, drilling cores is a key aspect in glaciological research. In contrast to other environmental archives, such as marine sediments or tree rings, ice provides a higher temporal coverage and resolution (FISCHER, unpublished). One of the most ambitious ice core projects so far has been the European Project for Ice Coring in Antarctica (EPICA), a multinational research project funded by the European Science Foundation, which started in 1996. Two deep ice cores from two different locations in East Antarctica should be drilled. The intention was to extent the available climatic record and get insights on the climate stability and development from present day until the middle Pleistocene and the Cromerium, which comprises several glacial and interglacial phases, respectively (EPICA COMMUNITY MEMBERS, 2004, 2006; WILHELMS et al., 2014). One site was chosen at Dome Concordia (further Dome C) (s. Fig. 3) located in the Indian/Pacific sector of Antarctica, where a 3260 m ice core was drilled with a time span of almost 800,000 years (JOUZEL et al., 2007; LUTHI et al., 2008) covering eight glacial cycles (EPICA COMMUNITY MEMBERS, 2004), four cycles more than previous drilled ice cores (PETIT et al., 1999; SIEGENTHALER et al., 2005). This core at Dome C was meant to give results about mechanisms of global climatic changes (STAUFFER et al., 2004). Additionally, at Kohnen station another ice core with a final length of 2774 m was drilled, which represents the first deep ice core in the Atlantic sector of Antarctica. Although it covered only about 150,000 years (RUTH et al., 2007), due to a 2.5 times higher accumulation rate the core at Kohnen (abbreviated 'EDML') provided a higher temporal resolution than at Dome C (OERTER et al., 2000). Because of its location and resolution, the EDML-core is considered as an important key for the link between Northern and Southern hemisphere climate evolution (EPICA COMMUNITY MEMBERS, 2006; OERTER et al., 2004). Both EPICA ice cores stopped only meters above the bedrock at each location. Nevertheless, to get insights even deeper into the past and earth's climate history, during the last years glaciologists set

their sights on finding a new drill site that reveals even older ice than found in framework of EPICA at Dome C. Recent estimates based on ice and heat flow modelling incorporating geophysical and glaciological data reveal up to 1.5 million years old ice in East Antarctica (FISCHER et al., 2013), which is almost the interval of the Quartenary. The potential drill site has to meet criteria like low horizontal ice flow, medium ice thickness to avoid either basal melting or too little ice records and low geothermal heat flux. The region between Dome Fuji and Dome C (s. Fig. 3) in East Antarctica seems to have high potential for this endeavor (FISCHER et al., 2013).

Transformation from snow to ice

A unique feature to investigate in ice cores, which no other environmental archive can offer, are entrapped air inclusions providing direct records of the paleo-atmosphere (RAYNAUD et al., 1993). The trapped gases are stored in the ice matrix and are closed off from the atmosphere. Other tracers used in environmental studies, like trace elements and stable isotopes, are integrated into the firn matrix and provide a continuous record of the paleo-environment until they are finally sealed in ice (PETIT et al., 1999). However, until that stage, the porous space of the firn matrix is connected with the air above surface, which causes for dating and interpretation of ice cores. For that reason, the transformation process from snow to ice and has to be understood as much in detail as possible.

Fresh snow, directly after deposition, usually has a density between 50 and 200 kg m⁻³, dependent on location and dampness. In polar regions the density of fresh snow may even exceed 200 kg m⁻³ (FREITAG, 2016, pers. commun.). It initially has a high amount of pore volume. By settling and sintering snowflakes get rounded, condensed and are called firn with ongoing metamorphosis and increase of density. After deformation and recrystallization processes the firn-ice transition is reached at densities around 830 kg m⁻³ (CUFFEY & PATERSON, 2010) (s. Fig. 1). The remaining gases in the ice structure are sealed and no exchange with the air of the overlying atmosphere is possible any more. Consequently enclosed air is much younger than the surrounding ice.

The depth of this close-off (s. Fig. 1) and also the age difference between ice and air varies strongly. One of the deepest firn-ice transitions is estimated from a firn core at Wilkes Land, East Antarctica (s. Fig. 3) in about 110 m depth with age differences up to 2,000 years (FREITAG, 2016, pers. commun.). At cold locations with low accumulation rates, the age difference can even exceed this range by the factor of two, as it was likely in glacials (SCHWANDER et al., 1997).

Therefore, for precise reconstructions – including dating the age differences of air bubbles – and usage of parameters derived from ice cores, an adequate age scale for each core drilled has to be applied. This time-function assigns continuous depth values to time values, mainly dependent on the accumulation rate and on the thinning of the ice layers due to macroscopic flow. For this purpose absolute markers are necessary that can be assigned to a specific date. Absolute dating is done mainly via reference horizons of, for instance, volcanic eruptions like Tambura in 1815 or Pinatubu in 1991 (PALMER et al., 2001) or natural and artificial occurring radionuclides (POURCHET et al., 2003). In the

firn column the concentration of trace elements can also visualize annual layers by changing their color or brightness, respectively. As long as these layers are clearly recognizable, these are helpful for dating as well (FREITAG et al., 2013b; TAYLOR et al., 2004).
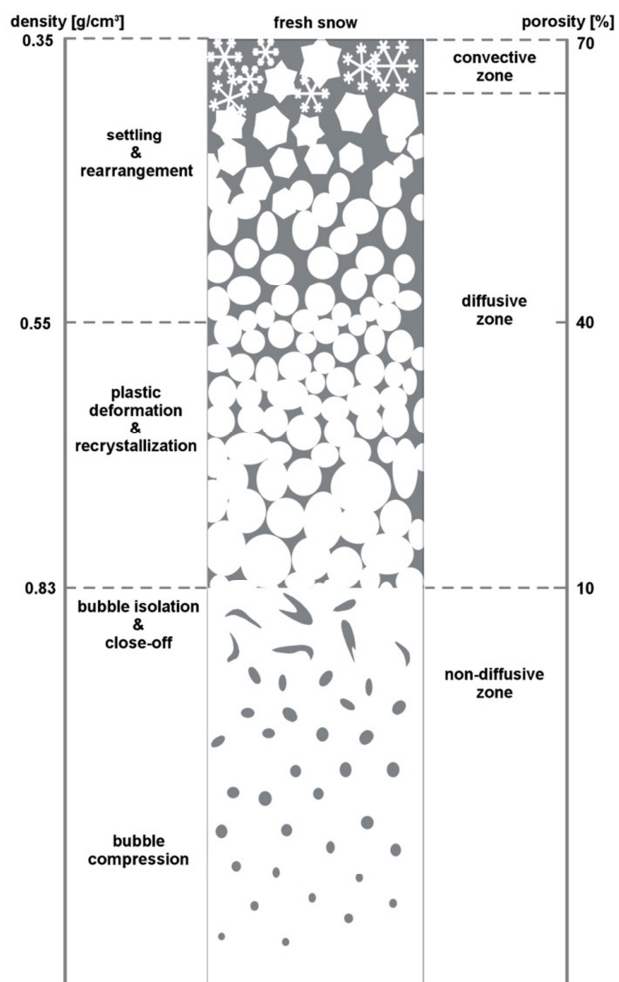
Fig. 1: The snow metamorphism is a complex interaction between different processes acting on macro- and microscale in different stages, which are summarized in the left panel of the sketch. Very important physical parameters for classification are density (left vertical axis) and the pore volume (right vertical axis). After deposition, density steadily increases with depth while pore volume decreases. Densification of the firn column is mainly a function of temperature, accumulation (HERRON & LANGWAY, 1980) and – to a smaller part – impurities (FREITAG et al., 2013b; HÖRHOLD et al., 2012). Dashed lines in grey symbolize critical densities where dominance of microscale processes changes. Settling and rearrangement of snowflakes are the first dominating processes up to a density of 550 kg/m³, where sphere packing is reached (NISHIMURA et al., 1983). Afterwards, microscale processes like recrystallization and dislocation creep occur (EBINUMA & MAENO, 1987). At that stage the exchange with the atmosphere is driven by diffusional processes (SCHWANDER et al., 1997) until the pore closure around 830 kg/m³. In deeper strata, bubbles are isolated and deformation takes place. Below the pore close-off no exchange with the atmosphere is possible any more. Age differences between enclosed air and surrounding ice are of high importance for paleoclimatic research.

State of the art

Ice cores are used to give access to fundamental parameters for paleoclimatic reconstructions and models. Several physical properties can be determined including density and pore volume, for instance with non-destructive radioscopic imaging (FREITAG et al., 2013a), and microstructure properties (BENDEL et al., 2013; WEIKUSAT et al., 2009). While these parameters give insights about the transformation from snow to ice and ice deformation, different chemical species can either be used as direct or indirect indicators for past climate. Proxies store information about temperature and precipitation as well as the chemical composition of the paleo-atmosphere and its transport paths with marine, terrestrial, cosmogenic and anthropogenic origin (LEGRAND & MAYEWSKI, 1997; PETIT et al., 1999).

Stable water isotopes are used as proxies for short and long term temperature reconstructions. The quantitative interpretation of hydrogen and oxygen isotopes is based on fractionation processes and their dependence on local air temperature (CRAIG, 1961a; DANSGAARD, 1964). In ice cores both isotope signals give us good estimates for Holocene and Pleistocene temperature trends (OERTER et al., 2004; PETIT et al., 1999). For instance, glacial and interglacial periods can be inferred from isotopic signals and total dust input (s. Fig. 2) (EPICA COMMUNITY MEMBERS, 2004) as well as grain size in the firn matrix (LAMBERT et al., 2008; WEISS et al., 2002). Correlated records from Greenland and Antarctica also reveal a close coupling between Northern and Southern hemisphere climate (EPICA COMMUNITY MEMBERS, 2006).
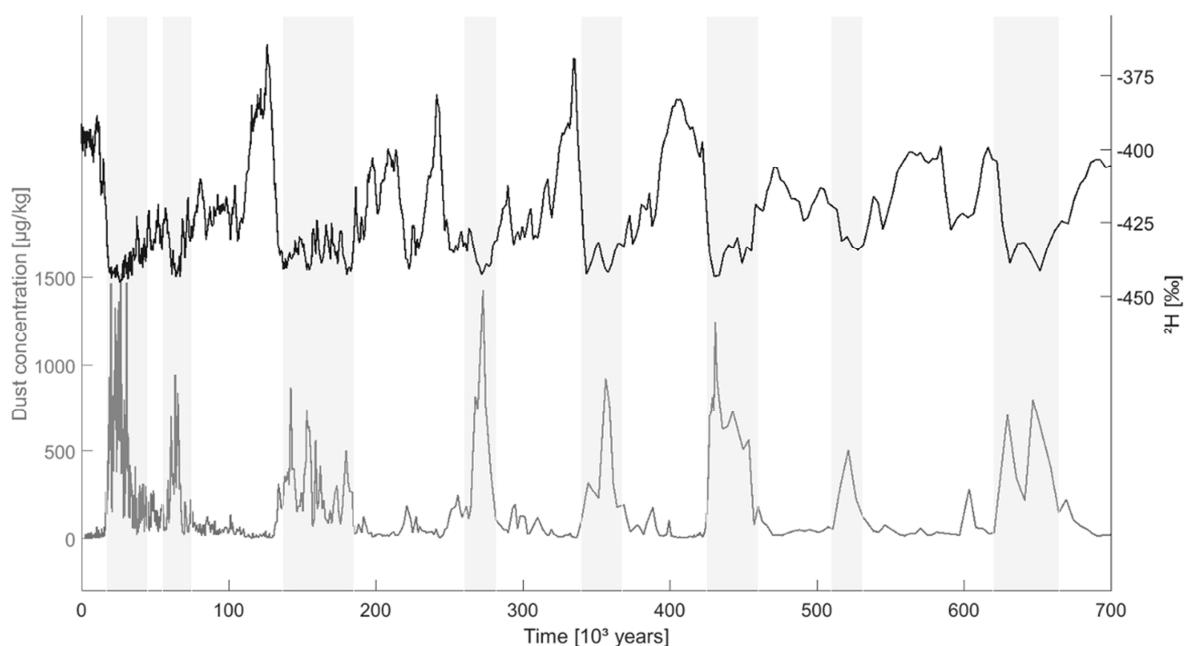
Fig. 2: The anti-phase correlation between total dust input (lower section; grey line) and δ²H (upper section; black line) from the EPICA ice core at Dome C (s. Fig. 3) enabled the identification of eight glacial cycles during the last 700,000 years. The abscissa represents the time interval from present day (left) to 700,000 years in the past (right). The scale of total dust input in µg kg⁻¹ is depicted on the left, the scale of relative abundance of deuterium isotopes on the right vertical axis. High dust input is characteristic for glacial periods since increased aridity and wind strength lead to higher physical erosion on the continents and increased transport energy. Low δ²H values in glacials results from linear dependence with temperature as low temperatures cause fractionation in favor of lighter isotopes. To underline the correlation grey shaded areas represent glacial periods. Dataset used for this figure is published by EPICA COMMUNITY MEMBERS (2004).

Although these results seem solid, several processes in the upper snow and firn layers have to be considered influencing the original deposited signal. Snow drift and wind scouring are two possible pre- or syndepositional impacts that alter not only the isotopic signal but also the whole snow and firn column (FISHER et al., 1983). On the other hand postdepositional processes occur, which normally are more complex and difficult to observe. Among those, for instance, are sublimation and condensation processes (STEEN-LARSEN et al., 2014). These take place at phase transitions where natural fractionation may alter the isotopic signals $\delta^{18}O$ and δ^2H. Recent field observations prove that fact.

Directly measured fresh snow samples had shown different δ^{18}O signals than the same samples after some days of storage (KIPFSTUHL, 2014, pers. commun.). These (re)condensation and (re)sublimation processes may influence the original isotopic signal dramatically. Additionally diffusional processes, first discovered by LANGWAY (1970), controlled by water vapor ventilation are able to change the isotopic fingerprint while an exchange with the atmosphere is possible (TOWN et al., 2008). New publications even focus on the diffusion length of stable water isotopes (VAN DER WEL et al., 2015). Furthermore, seasonal δ^{18}O and δ^2H signals can be completely overprinted (HOSHINA et al., 2014) or get smoothed, whereas the dispersion in pore space is stronger for oxygen than for hydrogen isotopes (JOHNSEN et al., 2000). These effects seem to be dependent on accumulation rate (HOSHINA et al., 2014). Especially in single ice cores from low accumulation sites in relatively stable periods like the Holocene, the natural climate variability often does not exceed the intrinsic noise (MÜNCH et al., 2015).

Similar effects also concern trace elements, mostly deposited as aerosols, that can either be measured by a continuous measuring tool like CFA (continuous flow analysis) (BIGLER et al., 2011; KAUFMANN et al., 2008) or as discrete samples with tools like ion chromatography or ICPMS (inductively coupled plasma mass spectrometry) (MÜLLER et al., 2011). It is obvious that the same pre- and syndepositional processes as mentioned above do not only affect isotopes but every species that is stored in the snow matrix including trace elements. Concentrations of aerosols have been analyzed for quite a while now (SAVOIE et al., 1993; WAGENBACH et al., 1998a; WAGENBACH et al., 1998b) to discuss back trajectories (REIJMER et al., 2002), sea ice extent or marine productivity (WOLFF et al., 2006). Windblown aerosols with continental origin in the Vostock ice core revealed that the dust input to Antarctica was maximum during pleniglacial periods and minimum in interglacials (s. Fig. 2) (PETIT et al., 1999). Those aerosol signals seem not to be solely dependent on loading of the boundary layer (s. Fig. 5); more recent investigations in layers above the firn-ice transition reveal diffusion and dissemination processes that significantly influence the signal which is later stored in the ice (WELLER et al., 2004; WELLER & WAGENBACH, 2007). Especially anions, such as Cl$^-$, NO$_3^-$ and methane sulfonate (MSA) are affected by postdepositional losses (WELLER et al., 2004), dependent on different parameters like, for instance, accumulation (KARLOF et al., 2005). Additionally, some species are mobile with changing chemical milieu. In acidic conditions Cl$^-$ and NO$_3^-$ change their species by chemical reaction and get volatile (WELLER, 2015, pers. commun.). Moreover, these particles that are incorporated into the snow matrix influence the densification of the snow and firn column. Recent studies reveal a close parallelism between the density variability and impurities in deeper firn and ice. Ions like calcium weaken the firn and ice structure as they reduce the activation energy for deformation and enhance the possibility for compaction (FREITAG et al., 2013b; HÖRHOLD et al., 2012).

Scientific questions & hypothesis

Profound knowledge of snow metamorphism and how various tracers are incorporated into the firn structure is of high importance as it has influence on proxies stored in snow, firn and ice and their interpretation. Therefore one need is to clarify the relation between precipitation and deposited proxies, especially as there is still lack of continuous data-based records of annual accumulation distribution in Antarctica. In this context we need to know how trace elements and stable isotopes are deposited, how the signals are characterized and what they really tell us. This master thesis focuses on seasonal characteristics in aerosol concentrations and stable isotopes as well as their link to atmospheric and physical parameters at a medium accumulation site in Dronning Maud Land, Antarctica. The thesis is done in section glaciology of Alfred Wegener Institute, Helmholtz Centre for Polar and Marine Research, Bremerhaven.

As it is still not clear, how especially isotopic signals are incorporated into the snow and firn structure, during the field campaign 2013/14 at Kohnen station several snow profiles of 50 cm depth were taken to investigate the depositional patterns. The objective was to identify and confirm seasonal-specific trends and patterns in snow chemistry and aerosols, which enable us to adjust a correct time scale for the samples. With the time-referenced data, we try to explain depositional behavior of isotopes and trace elements and what processes play a major role in it. Additionally, we investigate the formation of annual snow layers as well as the temporal variability of analyzed species. Incorporating weather data, e.g. temperature, will give information about seasonal and general sensitivity of those proxies. Furthermore, we link the isotopic and trace element record to snow density data and clarify the overall dependence between those species, as suggested, for instance, in FREITAG et al. (2013b). In this thesis we will distribute new findings on the temporal resolution of proxies, their variation in depth and how the deposition of trace elements and isotopes is associated with accumulation, as suggested, for example, by KARLOF et al. (2005). We will further show whether patterns in seasonal signals can be expressed in a linear correlation of major aerosol species and isotopic ratios.

Although more data for a reasonable analysis are needed, we try to discuss the aerosol concentration and isotope ratios in terms of postdepositional losses or alteration. Diffusion (VAN DER WEL et al., 2015; WELLER et al., 2004) and fractionation processes (STEEN-LARSEN et al., 2014) may be evidenced by unexpected changes in aerosol concentrations, element ratios or isotopic signals.

During the last years and centuries, investigations of ice cores at different locations were carried out. As part of that, recently the focus changed over to the question, how reliable a signal from one single core or site can be (MÜNCH et al., 2015). In that context, we try to discuss the results regarding temporal and spatial variability of discrete samples from a finite region comparing and calculating variance and using correlation functions. In the end we will show, that the temporal variability at Kohnen station with that specific setup exceeds the spatial variability on a small scale area.

Finally, we will feedback the approach including the sampling setup in the field and suggest improvements for further field campaigns and analyses.

Study area

Samples that are analyzed in this study are taken in season 2013/2014 at Kohnen station (75°0' S; 0°4' E) (s. Fig. 3). Alfred-Wegner-Institute for Polar and Marine Research in Bremerhaven (AWI) has the logistic leadership and responsibility. It was established in 2001 in the framework of EPICA. It provides space for 20 scientists and is only available in austral summer seasons (usually December to February). Kohnen station is partly built from old container boxes from the former Filchner station at the Southern Weddel Sea, which was salvaged in 1999 from a drifting iceberg of the Filchner-iceshelf (DRÜCKER et al., 2002).
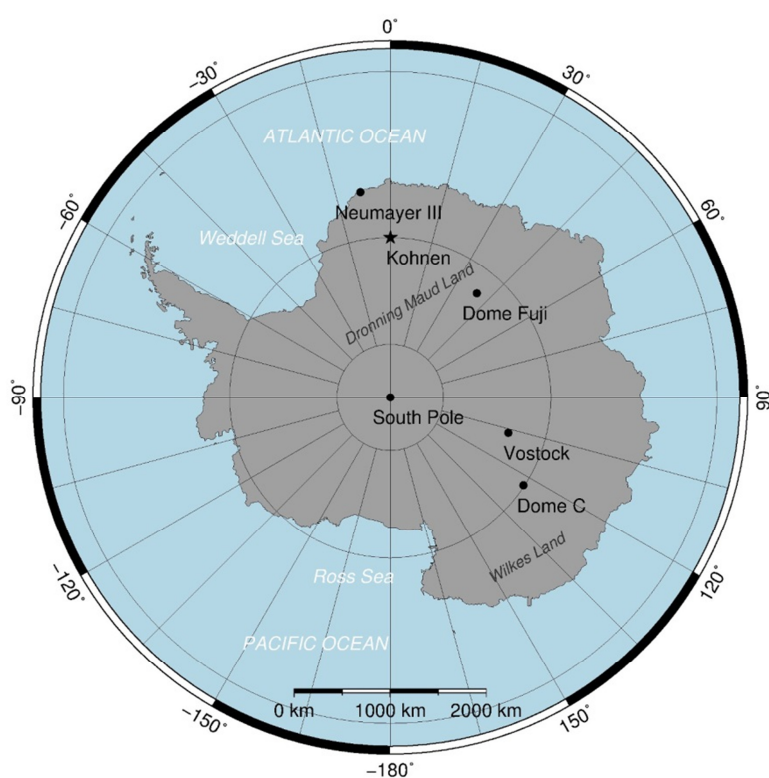
Fig. 3: This overview map shows the Antarctic continent in grey with surrounding oceans and largest marginal seas (white annotations). Indicated with black dots are exemplary inland research stations including the EPICA drill sites at Kohnen and Dome C. The black star symbolizes Kohnen station (75°0' S; 0°4' E), study area of this thesis. Logistically important as starting point for traverses and supply for Kohnen station is coastal research site Neumayer III. It is located in the Atlantic sector like Kohnen. Both research stations are organized by AWI. Map was created with software GMT (WESSEL & SMITH, 1991).

Kohnen station is located in Eastern Dronning Maud Land, Antarctica, in Amundsenisen, part of the East Antarctic plateau. It is at 2892 m a.s.l., roughly 550 km away from the Atlantic sector coast with a mean annual air temperature of -46°C (OERTER et al., 2009) (comp. Fig. 24). At Kohnen station and large parts of Dronning Maud Land there is a net accumulation of roughly 64 kg m^{-2}a^{-1} (OERTER et al., 1999). Compared to other areas on the Antarctic continent the accumulation can be interpreted as intermediate. Recent ablation stake measurements from January 2013 to January 2014 revealed increasing accumulation at Kohnen (KIPFSTUHL, 2015, pers. commun.). Medium ice thickness at Kohnen station is 2782 ±10 m (STEINHAGE, 2001).

Additionally, at Kohnen station an automatic weather station is installed. Parameters like temperature,

atmospheric pressure, precipitation, wind speed and solar insulation are recorded on hourly basis. Mean temperature between November 2013 and February 2014 according to the weather station was -27.8°C. Dominating wind direction at Kohnen is mainly Northeast to East (65° true North) (DRÜCKER et al., 2002; TURNER et al., 1995). Trajectory models have shown that predominantly air masses from the South Atlantic reach Kohnen station (REIJMER et al., 2002), also carrying mineral dust from Patagonia (BICKERT, 2014, pers. commun.).

THEORY

Aerosols

A dispersion of tiny solid or liquid particles in a gaseous phase is called aerosol. Many different aerosol particles are produced all over the world and transported with the wind over high distances also to polar regions. Particles that are emitted directly into the atmosphere are called primary aerosols. Sources can either be sea spray in marine areas, terrestrial material from soil and deserts or sulfuric species as indicator for productivity of marine algae or volcanic and anthropogenic emissions (WOLFF, 1996b). Secondary aerosols are produced in the atmosphere during oxidation of trace gases involved in the sulfur, nitrogen, halogen and carbon cycles (LEGRAND & MAYEWSKI, 1997).

The most abundant aerosol source is sea salt with the main components sodium and chlorine. It is produced by bubble bursting and wave crest dispersion (MONAHAN et al., 1986). About 1000 Mt sea salt per year are brought into the air via dispersion (FISCHER, unpublished). In polar regions the formation of sea salt aerosol from frost flowers is an additional possible source (RANKIN et al., 2000). The second largest aerosol species are mineral aerosols from continental regions, mainly deserts. From those areas annually up to 500 Mt are brought into the air via physical erosion, especially in arid regions. Examples for terrestrial aerosols are aluminum, silicon and calcium as well as carbonate. Smaller amounts of biogenic, volcanic and anthropogenic sulfur, nitrate and ammonium species complete the major aerosol components (LEGRAND & MAYEWSKI, 1997; WOLFF, 1996b).

Two main wind types bring aerosols to the Antarctic continent. These are inlands and katabatic winds. The two wind types differ in composition of aerosols as they have different source regions. Inland winds tend to bring close distance primary aerosols with high amounts of marine particles while katabatic winds are loaded with aged aerosols and secondary aerosols from the stratosphere (s. Fig. 4). As precipitation lowers the atmospheric residence of particles, aerosols are more durable in upper troposphere than in the lower marine or continental boundary layer. Therefore aerosols from troposphere are older and may travel longer distances. Stratospheric aerosols tend to arrive during austral summer seasons as in polar winters the circumpolar vortex is well established (WAGENBACH, 1996).
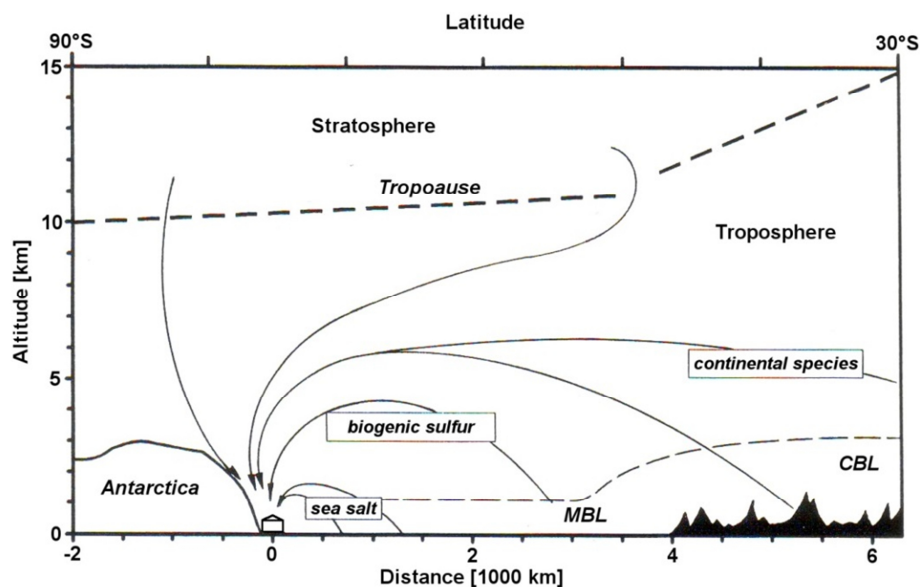
Fig. 4: Different transport pathways of several aerosol species to the Antarctic continent are drawn in this sketch. On the horizontal axis the geographic position on the Southern hemisphere is depicted and the relative distance, respectively. The vertical axis represents the height over sea level in kilometers. The continent in left bottom corner is Antarctica with a symbolized research station at the coastal part. Arrows symbolize typical wind patterns that arrive in Antarctica. Four inland winds and one katabatic wind arriving in inverse direction from central Antarctica towards the coast are shown. Inland winds carry the major primary aerosols like sea salt, continental dust and biogenic sulfur species. Winds coming from stratosphere are loaded additionally with secondary aerosols. They have a higher residence time as precipitation lowers the amount of aerosols in tropospheric areas. Primary aerosols are produced in the marine boundary layer (MBL) and continental boundary layer (CBL). Sketch is drawn after WAGENBACH (1996).

In general the ion concentration in snow is a direct signal of the constitution of the atmosphere. The main factor that controls the ion concentration is the source strength. The more aerosols are created, the more are deposited on the snow surface. Nevertheless, several factors are described that alter the original signal during or after deposition. Non constant scavenging ratios, efficiency of transport and deposition as well as postdepositional losses influence the trace element concentration in snow (WHITLOW et al., 1992; WOLFF, 1996b). In general the agreement between snow chemistry and aerosol chemistry may be more likely in austral summer as the surface inversion is minimal.

Sodium and chlorine are the most abundant aerosol particles, especially in Antarctica which is completely surrounded by oceans. In general 2-50 µg m⁻³ sea salt aerosol can be produced, dependent on the wind speed (WAGENBACH et al., 1998a). The primary input of the main sea salt components is during austral winter season between July and October as cyclonic activities favor intrusions of marine air (WELLER & WAGENBACH, 2007; WHITLOW et al., 1992). Sodium and chlorine clearly show the largest spatial and temporal variability (WAGENBACH, 1996). WHITLOW et al. (1992) published data showing 11.1 ng g⁻¹ sodium and 34.1 ng g⁻¹ chlorine average concentration at South Pole between 1955 and 1988. Especially sodium is considered as a reliable tracer as it is quite unreactive and shows low evidences for postdepositional alteration or diffusion (WOLFF, 1996a). It is the only counterpart to the otherwise dominating acidic species SO_4^{2-}, MSA and HNO_3 (WAGENBACH et al., 1998a). Chlorine

14

is also considered to have conservative behavior as sodium but can react to hydrochloric acid under acidic conditions and get volatile (WELLER et al., 2004). Due to higher residence time the ratio of chlorine to sodium can be used as indicator of aged sea-salt aerosol and long-range transport (LEGRAND & DELMAS, 1988).

Sulfuric aerosol species can either be of biogenic, geogenic or anthropogenic origin. Dependent on the oxidation state aerosols are present as methane sulfonate (MSA), sulfur dioxide (SO_2) or sulfate (SO_4^{2-}). While sulfate to a smaller part can be present as sea salt component, biogenic sulfur emissions dominate natural sulfur cycle in polar regions. Metabolism of marine algae produces mainly dimethyl sulfate (DMS) that gets oxidized in the atmosphere either to SO_2 or via photochemical oxidation to MSA (AYERS et al., 1991; BOTTENHEIM & BARRIE, 1996). Both sulfate species therefore can be indicators for marine biogenic activity and tracers for austral summer when biological activity is at its maximum. MSA shows in phase correlation with non-sea-salt sulfate (WOLFF, 1996a), which is again a good evidence for same biogenic origin. At Neumayer III usually MSA concentrations between 100 and 350 ng m^{-3} are measured, non-sea-salt SO_4^{2-} concentrations range from 250-700 ng m^{-3} (WAGENBACH, 1996). As MSA has a low residence time and is deposited fast, concentrations decrease with ongoing inland transport (WELLER & WAGENBACH, 2007). Aerosol input of MSA and sulfate is highly regular. Maximum concentrations are measured in coastal areas around the 20th January with an uncertainty of about eight days (WELLER & KIPFSTUHL, 2015, pers. commun.). Yearly low is observed around the at 18th July (WAGENBACH, 1996). All sulfur species are affected by postdepositional movements and losses (WELLER et al., 2004).

Two common nitrogen species are present as aerosols, which are nitrate (NO_3^-) and ammonium (NH_4^+). Nitrate is a typical spring signal which is caused by denitrification of Antarctic stratosphere (WAGENBACH, 1996). In coastal sites it arrives from October to November in the air and is deposited in December to January. It is very soluble and reactive and may cause high contamination effects (KIPFSTUHL, 2014, pers. commun.). Additionally HNO_3 is produced by photolysis in upper firn layers and is volatile (WELLER et al., 2004). On the other hand NH_4^+ is produced by combustion and bacterial decomposition (LEGRAND et al., 1998). NH_4^+ is often below detection limits, but also shows numerous artefacts. Ammonium has its minimum in winter (April to September) and maximum in summer (November to February) in air, deposition is delayed similar to nitrate (WAGENBACH, 1996). Together with calcium carbonate and sodium chloride, ammonium controls acidity of the atmosphere (WAGENBACH et al., 1998a).

Some aerosols like NH_4^+, Cl^- and non-sea-salt SO_4^{2-} shift their transport into upper troposphere and tend to intrude via katabatic winds. Increased vertical mixing at South Pole favors katabatic winds and the transport from stratosphere to troposphere (WHITLOW et al., 1992). Annual layering can best be observed in SO_4^{2-}, MSA, Na^+ as well as Na^+/Cl^--ratio.

Depositional processes

In general, three different deposition types are distinguished based on chemical and physical processes. They are strongly dependent on meteorological boundary conditions and each of them is present in arctic regions. Predominant type in polar regions is wet deposition, especially in high accumulation areas, at low accumulation sites the amount of dry deposition increases (DAVIDSON et al., 1996).

Dry deposition is – in contrast to wet and fog deposition – not dependent on any kind of precipitation and discrete time intervals. It can be expressed mathematically as $F_d = v_d(z) \, c_a(z)$ in [g cm^{-2}s^{-1}] with F_d as dry deposition flux, $v_d(z)$ as dry deposition velocity and $c_a(z)$ as airborne concentration. Via aerodynamic transport driven by eddy diffusion, particles are carried to the area of deposition. Within a small boundary layer just above the snow surface, aerosols travel according to temperature or humidity gradients or are affected by several processes of particle deposition. Dependent on snow conditions, particle characteristics and concentration as well as wind speed, particles remain in the snow surface or rebound into the boundary layer (DAVIDSON et al., 1996).
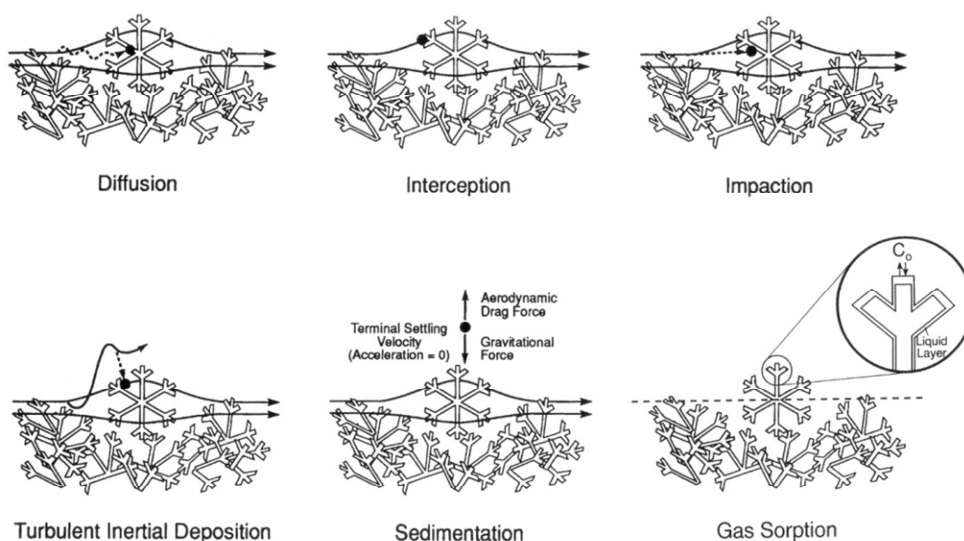
Fig. 5: Six major processes of dry deposition that are possible to take place within the boundary layer slightly above the snow surface are shown above. In the poorly packed snowflakes, physical and chemical microscale processes are responsible for the deposition of an aerosol particle. The transportation within the boundary layer is driven by temperature or humidity gradients as well as wind pumping. Figure is taken from DAVIDSON et al. (1996).

Wet deposition of particles is dependent on the presence of water molecules in form of liquid droplets, ice crystals, rain drops or snowflakes. Aerosols are incorporated into water molecules by different processes either while or after nucleation. On the one hand aerosol particles can serve as condensation nuclei themselves. Hygroscopic particles like Na$^+$, Cl$^-$ or SO$_4^{2-}$ are in favor of forming droplets while particles with crystal lattice structure are more likely to form ice crystals, also dependent on air

temperature. Alternatively, aerosols are scavenged by water droplets or snowflakes in or below clouds by boundary layer processes as mentioned above (s. Fig. 5). Single droplets or flakes can evolve and aggregate to larger particles up to 30 µm (BORYS et al., 1992). The flux can be mathematically expressed as $F_W = \rho_W\, P\, c_s$ in [g cm^{-2}s^{-1}] with ρ_W as meltwater density, precipitation rate P and the concentration of chemical species c_s. Transportation processes are as the same as in dry deposition (DAVIDSON et al., 1996).

Fog deposition happens in presence of water in liquid or solid phase at the earth's surface. In polar regions it mainly occurs in summer with supercooled water droplets. The size of the droplets is similar to wet deposition. Fog deposition can be much more effective than dry deposition due to higher settling velocities (BERGIN et al., 1995; BORYS et al., 1988). Mathematically it can be expressed as $F_f = v_s(t)\, c_f(t)$ in [g cm^{-2}s^{-1}] with $v_s(t)$ representing settling velocity of fog droplets and $c_f(t)$ the concentration of aerosol species (DAVIDSON et al., 1996).

Isotopes

Variants of chemical elements with constant atomic number but different mass are called isotopes. They have the same amount of protons but a different amount of neutrons in their nucleus. According to the following notation ^{M}E, mass number (M) gives information about the sum of protons and neutrons in nucleus of the element (E). Most elements have a natural variety of isotopes which occur in a certain ratio. The most abundant isotope for hydrogen is ^{1}H (99.984% abundance) followed by deuterium (^{2}H) (0.016%) and tritium (^{3}H) ($<10^{-15}$%). Oxygen also has three naturally occurring isotopes, which are ^{16}O (99.76%), ^{17}O (0.04%) and ^{18}O (0.20%) (GAT, 1996). Dependent on their inner energy equilibrium, isotopes can be stable or radioactive. All above mentioned isotopes are stable except tritium, which decays with a half-life of 12.32 years.

Both elements are combined in the water molecule (H_2O). The absolute isotopic fingerprint (a) of one element in a distinct sample is calculated via heavy isotopes over light isotopes. It is common to present it in a relative value (δ) in per mill [‰]. The δ-value expresses the ratio of heavy to light isotope within the measured sample in relation to a defined standard. Samples with negative δ-values therefore contain a higher number of lighter isotopes, while samples with positive δ-values contain more heavier isotopes of the investigated element than the reference standard. The mathematical expression is

$$\delta = {}^{a_{sample} - a_{standard}} \big/ a_{standard} \times 1000 \, [‰] \qquad (\text{DANSGAARD, 1964}).$$

The commonly used reference standard for water isotopes is the Vienna standard mean ocean water (VSMOW), which per definition is zero and representing today's mean ocean water (CRAIG, 1961b).

Changes of the isotopic fingerprint occur at phase transitions like condensation and evaporation. Thermodynamic effects cause a separation process, which is called fractionation. Heavier isotopes behave more sluggish than lighter ones and are prone to remain in condensed phase, while light isotopes tend to fractionate into the evaporating phase. If the condensate phase is separated from the vapor phase and no equilibrium is established, the process is called Rayleigh fractionation (DANSGAARD, 1964). Additionally temperature effects have to be taken into account, which happen during cooling in the vapor phase. A scheme which simplifies the condensation process in nature best is shown in Fig. 6.
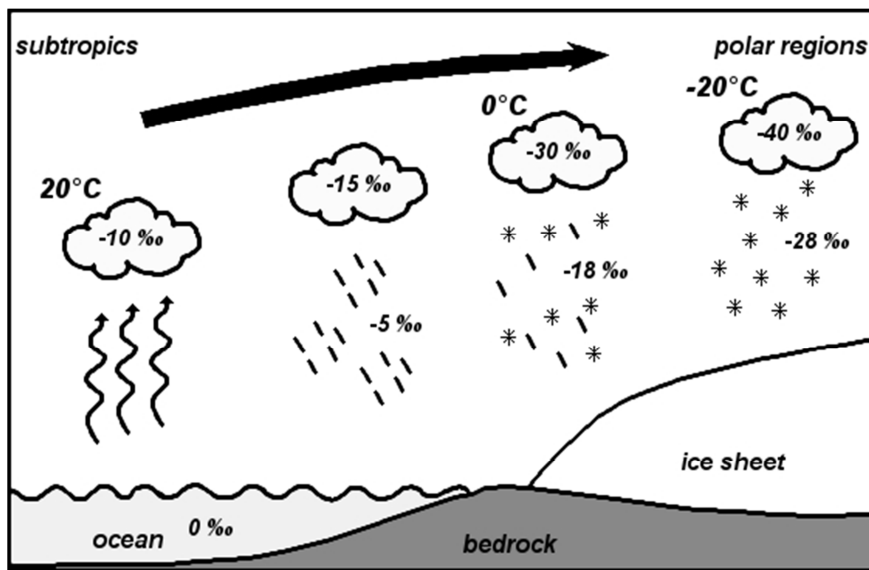
Fig. 6: In this sketch an example for a fractionation sequence with cloud forming and following precipitation from mid to high latitudes is schematically shown. The numbers indicate the δ-value of the respective phases. Exemplary air temperature values are also mentioned in the sketch. In general, lighter isotopes are favored in the evaporating phase, heavier isotopes in the condensate phase. Therefore, the initial cloud contains relatively higher amounts of lighter isotopes than ocean water which per definition has a $\delta^{18}O$-value of 0‰. Precipitation always shows a heavier isotopic signature than the cloud in the related stage. With increasing distance to the source region, precipitation constantly gets more and more depleted in heavy isotopes. As vapor and condensate phase are separated from each other after fractionation the process is called Rayleigh fractionation. Figure is drawn after VAN DER WEL (2012).

Fractionation processes are temperature dependent what enables scientists to derive paleo-temperatures from stable hydrogen and oxygen isotopes. For this purpose, different equations are used dependent on area of interest and environmental conditions, mainly on mean air temperature. For Greenland ice cores for example this was done by JOHNSEN et al. (2001).

With decreasing temperature, the fractionation factor between light and heavy isotopes increases (DANSGAARD, 1964). Compared to Fig. 6, if the temperature was lower over the Antarctic ice sheet than mentioned in the sketch, the precipitation had lower $\delta^{18}O$values. A strong coherence between $\delta^{18}O$ and δ^2H is expressed in the equation

$$\delta\,^2H = 8 \times \delta^{18}O + d \ [‰]$$ (CRAIG, 1961a).

The equation is called the global meteoric water line (GMWL) and combines isotopic composition of all meteoric waters. Each hydrogen and oxygen isotope pair forming a water molecule plots on or close to the GMWL, dependent on warmer (higher δ-values) or colder (lower δ-values) temperature of the source region. Variable d is called deuterium excess and has a value around 10‰ for most isotopic compositions of water. It can be seen as deviation from the GMWL. The deuterium excess is sensitive to the evaporation of water and reflects the slower movement of $^1H_2^{18}O$ in contrast to $^1H^2H^{16}O$. Deuterium therefore is enriched in the less strongly bound phase (evaporating phase) (PFAHL & SODEMANN, 2014). This effect can only be seen if there is not sufficient time for both phases to reach equilibrium. Seasonal effects in deuterium excess variations can be seen in Fig. 7. As the fractionation factors of hydrogen and oxygen are different, deuterium excess is subject of temperature dependent variations. For instance, deuterium excess can be used to characterize atmospheric circulation (PETIT et al., 1991) and source regions of precipitation (CIAIS et al., 1995; FERNANDOY et al., 2012). Relative humidity affects the isotopic composition of the water vapor. Arid regions are characterized by high deuterium excess, humid regions with low values. In polar regions the deuterium excess can also give information about evaporation and sublimation processes at the snow surface. While fresh snow usually shows high deuterium excess values, after deposition and interaction with surrounding air δ^{18}O tends to more positive and ^{2}H-excess to more negative values due to fractionation during sublimation (STEEN-LARSEN et al., 2014).
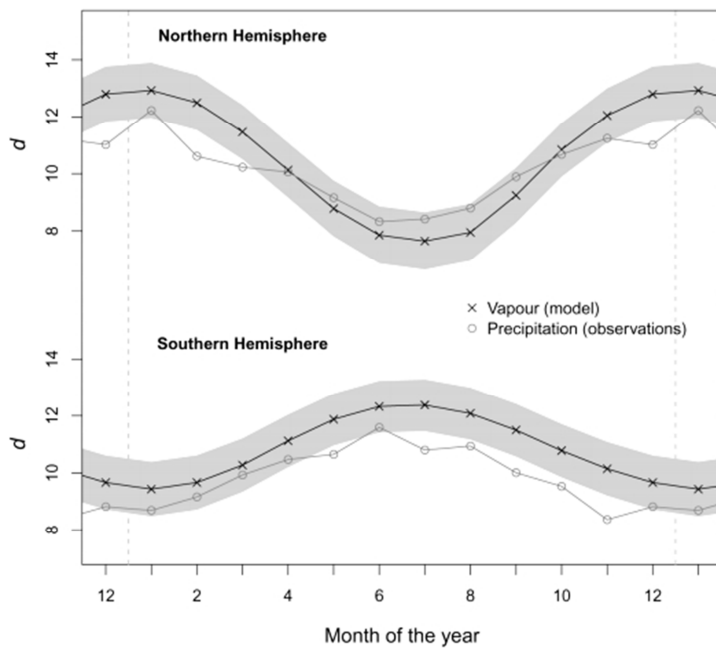
Fig. 7: The seasonal behavior of deuterium-excess can be seen in this figure. The upper panel shows the development on the Northern, the lower panel on the Southern hemisphere. The horizontal axis represents a time span of a year in monthly steps (number 1 is equal to January, number 12 is equal to December), the vertical axis shows the deuterium excess in per mill. D-values in summer months are lower than in winter months as $^1H_2^{18}O$ thermodynamical mobility is relatively higher at warmer temperatures. $^1H^2H^{16}O$ in contrast gets relatively depleted in the vapor phase. Amplitude of seasonal cycles is larger for Northern than for Southern hemisphere. Dark lines with crosses symbolize model results, grey lines with open circles observations from precipitation. Illustration is done after PFAHL & SODEMANN (2014).

19

MATERIAL & METHODS

Sampling procedure

Snow profiles were taken in austral summer months December and January in scientific season 2013/14 near Kohnen station (s. Study area & Fig. 3). For this purpose a contamination-free area is needed with an undisturbed snow surface. Snow profiles are collected using a fiberglass-pipe with a diameter of four inches (ca. 9.8 cm), further referred as snow liner. The pipe was manually rammed into the snow to a depth of 50 cm and dug out with a shovel manually. The snow core collected within the pipe was further processed in the field. It was cut into single samples using saw blades and an aluminum tray with default slots at the sides (s. Fig. 8). The top 30 cm of the snow liners were sampled in intervals of 1 cm, the bottom 20 cm in intervals of 2 cm. This procedure equals 40 distinct samples per snow liner. The fiberglass pipe was not cleaned after each sampling as this would have caused additional contamination. During work any skin contact with the snow liner was avoided by wearing gloves. After processing the samples were immediately filled in whirl pack plastic bags, stored in a cooling box and transported to AWI.

The sampling procedure was carried out at four profile positions, labeled IP1 to IP4. Location IP1 is the main location and was sampled most frequently in intervals of 24 or 48 hours for 53 consecutive days. Sampling of IP1 started on the 4th December 2013. Subsequent samples were collected in distance of 20 cm against wind direction. In total, at location IP1 41 snow liners were collected (s. Fig. 8). Locations IP2 to IP4 were sampled only three times each during the season with some days gap in between. Samples were taken on the 26th and 31st of December 2013 as well as on the 7th of January 2014. Subsequent samples at each location also had a distance of 20 cm and were collected in same direction as IP1 (s. Fig. 8). First samples of each location have a distance of 10 m between each other.
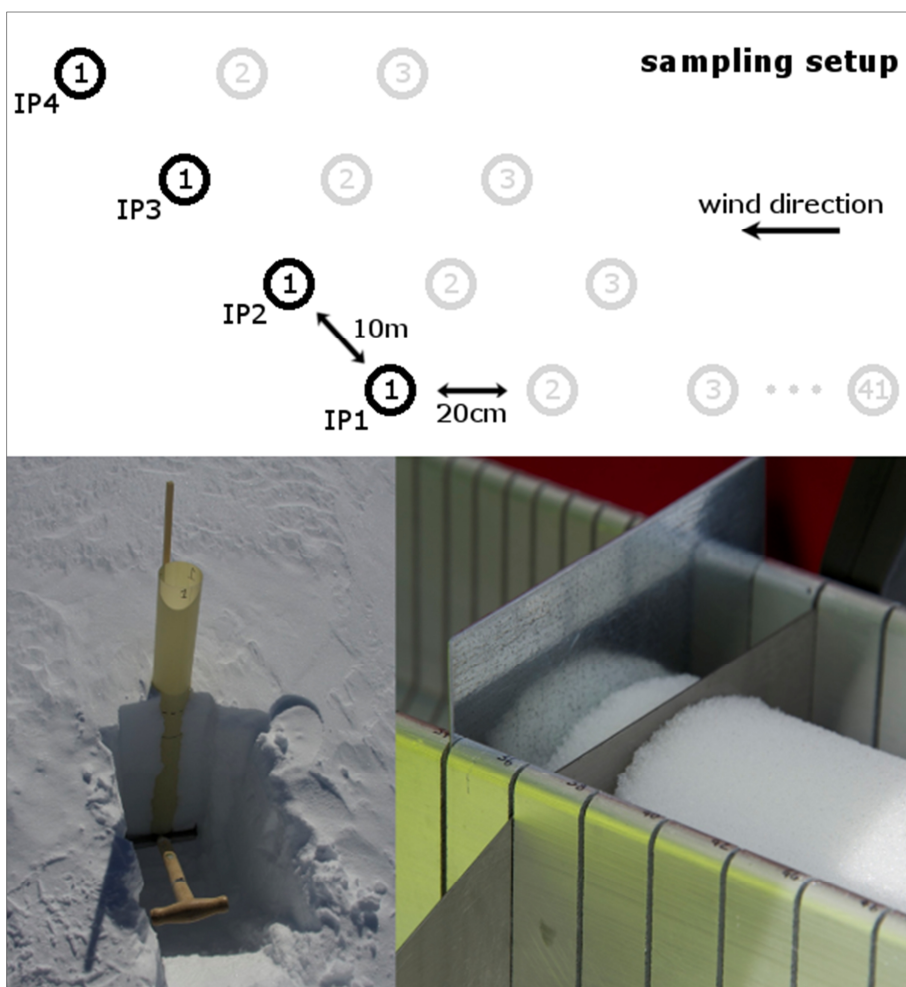
Fig. 8: Sampling setup in the field with four sampling locations (IP1 to IP4) is drawn in this sketch (upper panel). Distance between locations IP1 to IP4 is 10 meters. Between samples at one location there is spacing of 20 cm against wind direction. In total at IP1 a profile of 8 meter was accomplished. Acquisition of one snow liner is shown in the left bottom picture. The carbon fiber pipe is rammed into the snow and dug out with a shovel. The cutting tray is shown on the bottom right picture. Pre-sawn slots help generating equal-size samples from the snow liner cutting with saw blades. Upper 30 cm have a resolution of 1 cm, bottom 20 cm a resolution of 2 cm.

Measuring procedure

Trace elements

Chromatography is defined as a separation process which uses the affinity of molecules to specific phases. For the separation, a mobile and a stationary phase are used that are not soluble. The sample to be analyzed is transported in a carrier medium (mobile phase) through or over a retention medium (stationary phase). Dependent on the physico-chemical features, like adsorption and polarity, the samples need a certain time to be transported through the stationary phase. This retention time is characteristic for each molecule and is measured in a chromatograph (SCHWEDT, 1994).

For this study a Dionex IC2100 system was used. This system uses suppressed or non-suppressed conductivity detection for analyzing the sample concentration. Although inductively couples mass

spectrometry (ICPMS) can afford more precise measurements with lower detection limits (BARBANTE et al., 1999; MÜLLER et al., 2011), the high workload for preparation and analysis is not in relation to better results compared to chromatographic measurements. Additionally contamination, which is definitely the case for some samples, does exceed the precision of ICPMS by far. Therefore ICPMS is not recommended as tool for this subject.
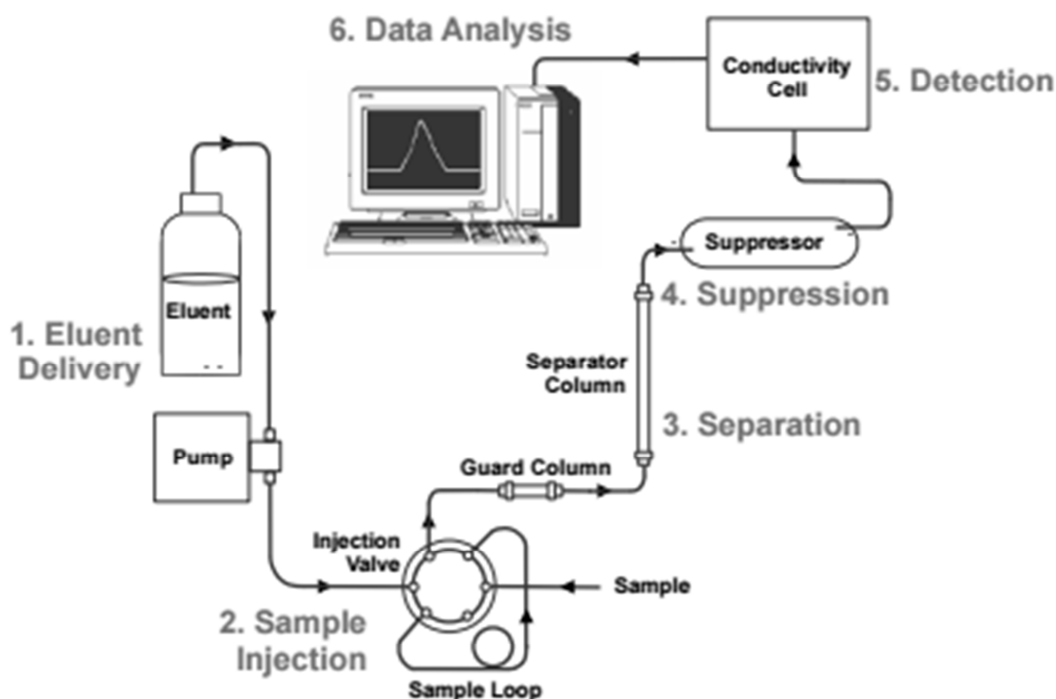
Fig. 9: A simplified illustration of the Dionex IC 2100 system is shown above. Steps of measurement are marked with numbers 1 to 6. Main chromatographic processes take place in the separation unit, which is the stationary phase. The eluent, representing the mobile phase, transports the sample through the different stages. Species identification takes place via specific retention time in the separation column, concentration of samples is identified via conductivity measurements. Illustration is done after DIONEX (2015).

The IC setup in general consists of an eluent pump with autosampler unit, a separation column, a suppressor and the detector unit (s. Fig. 9). The carrier medium (eluent) is pumped into the sample loop, where a defined volume of the sample is injected. The sample is taken by the autosampler and transported further by the eluent. In the separator column the main chromatographic process takes place. In this case it is fulfilled by an ion exchange unit. Dependent on the affinity of ions, which is based on the ionic radius and charge, individual ions are retained more or less strong within the exchange material. Species are identified by the specific retention time in the exchange column. The suppressor decreases the background conductivity of the eluent and enhances detection of single species, which is important for molecules or elements with low concentrations. A conductivity cell in the end measures the electrical conductance. The signal strength is analyzed with the integral of conductivity signal in the chromatogram and gets transferred into concentration by referencing it with

a known standard. Before each sample run, pathways are cleaned with a rinse to avoid contamination of previous samples. Background noise is determined by measuring blank samples.

Measurements were conducted with potassium hydroxide (KOH; concentration = 20 mMol/l) as eluent for anions, using a Dionex AS 18 (2 mm) separation column. With this setup inorganic anions and organic acids with low molecular weight can be measured. Usual analyzed species are fluoride, chloride, nitrate, carbonate, bromide and sulfate. For cations methane sulfonate (MSA, concentration = 21 mMol/l) was used as eluent. Separation column was a Dionex CS12a (2 mm) for analyzing lithium, sodium, ammonium, potassium, magnesium and calcium. Suppressor in the IC unit is a Dionex ERS 500.

Stable isotopes

Measurements of stable water isotopes were carried out with a Picarro analyzer using cavity ring-down spectroscopy (CRDS). In contrast to mass spectrometry - which is based on mass-dependent deflection during acceleration - CRDS refers to the natural infrared spectrum of gases. Advantages of CRDS over mass spectrometry are simultaneous measurement of ^{18}O and ^2H while water samples do not have to be separated and converted before, the possibility to apply continuous flow analysis as well as direct measurements of sublimation products (GKINIS et al., 2010).

Most gas molecules - including water - have a unique infrared spectrum consisting of narrow lines at a characteristic wavelength. This spectrum rests upon different energy levels in the atomic orbitals. Electrons being initialized jump between these levels and emit photons that absorb energy. This process is visible in spectra, which are unique for each molecule, element or – at low pressure – even isotope. The concentration can be analyzed by measuring the intensity of absorption.

In broad outline the CRDS analyzer consists of a laser diode, a cavity piston and a detector unit. The cavity piston is surrounded by insulating material to provide thermal stability. Inside the cavity three mirrors are installed facing each other in a triangular setup (s. Fig. 10). As the laser enters the cavity mirrors create a continuous travelling light wave. The light wave is reflected several times in the cavity which has a length of 25 cm. The real travelling pathway of the wave using the mirrors can be up to 20 km. After a threshold intensity level is reached, the laser beam is abruptly turned off. The light in the cavity still circulates being reflected by the mirrors with exponential intensity decay as reflexivity of the mirrors is slightly below 100%. This intensity decrease is called 'ring-down'.

Analyzed samples are now transferred into gaseous phase and injected into the cavity. Dependent on the gas filling in the cavity and its specific energy absorption, the decrease in intensity and time (ring-down) of the laser beam is characteristic. The ring-down time for this measurements depends on the reflexivity of the mirrors, length of the cavity and the absorption coefficient of the sample. For these measurements 120 μl from the molten samples were prepared and filled in vials, which are taken by an

autosampler unit. For more information see GKINIS et al. (2010) and PICARRO INC. (2016).

Analyzes are calibrated using a reference standard with known isotopic composition. Isotopic fingerprints are determined by average of four measurements. High advantage of the CRDS is the high precision and sensitivity. Due to a high pathlength, gases can be monitored in seconds or less, even in parts per trillion scale (PICARRO INC., 2016).
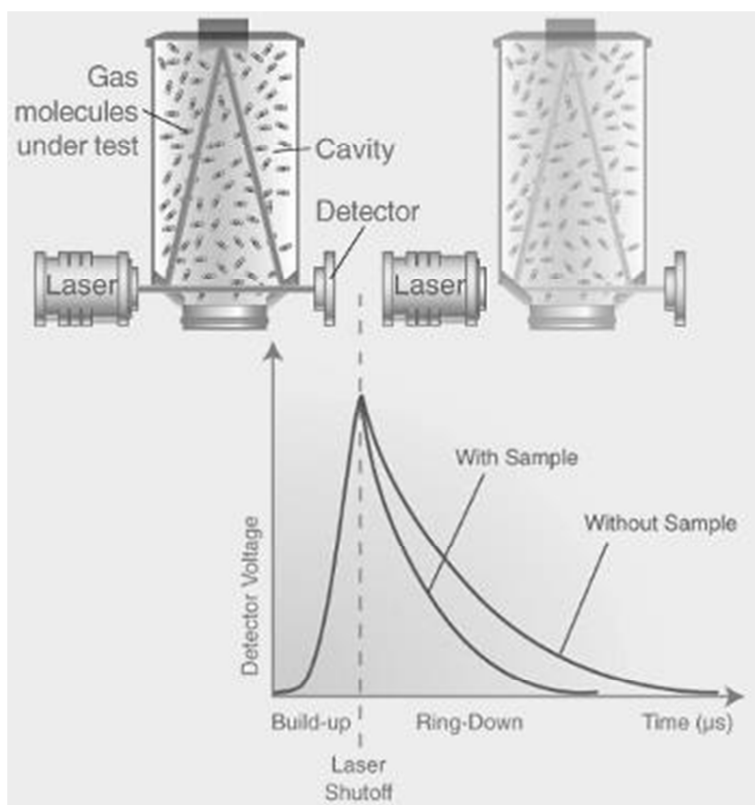
Fig. 10: The setup of CRDS Picarro analyzer is shown in the upper part of the figure. The laser source on the left emits the beam into the cavity piston with the three mirrors at left and right bottom and in the middle at the top. The standing wave is symbolized by the triangular shaped line. The detector unit is placed behind the second mirror of the cavity. In this figure two stages are shown. The first stage on top left shows the build-up of the standing wave until the threshold intensity is reached. Afterwards the laser shuts down and the standing wave gets further reflected by the mirrors what is visible in the top right picture. Dependent on the specific absorption coefficient the sample can be analyzed. A respective diagram can be seen in lower panel. It explains the coherence between ring-down time with and without a gaseous sample in the cavity Figure composed after PICARRO INC. (2016).

Density

Snow density data per single sample was mathematically calculated. For the net weight, the weight of the whirl pack bags was subtracted from the total weight (sample including whirl pack bag). Afterwards the net weight is divided by its volume, which was roughly estimated with 63.62 cm³. Samples with 1 cm width were divided by once the volume, samples with 2 cm divided by twice the volume.

Data processing & correlation operations

Data sorting and management was done with software Microsoft Excel. Simple calculations and ratios were also accomplished with this program. Processing, plots and graphics were compiled with software MATLAB (version R2015b) with license provided by AWI.

Correlation operations were done using Excel for determining basic parameters and MATLAB for calculation and visualization.

Linear correlation after Pearson between two species X and Y was calculated with the mathematical expression

$$r(X) = \left. c(X)_{sample} - average(X) \middle/ var(X) \right.$$

and

$$r(X,Y) = 1/n \sum_{i=1}^{n} r(X)_i \times r(Y)_i$$

with $c(X)$ representing the value of one single sample and $var(X)$ representing the variance of species X. The factor r is called Pearson's r and describes the linear coherence between two values. It can take values between -1 and 1. For $r(X,Y)=0$, species X and Y are not linearly correlated. The closer $r(X,Y)$ is to 1 or -1, it shows more positive or negative linear correlation, respectively.

RESULTS

Overview

Major ion species (Na^+, Cl^-, NO_3^-, SO_4^{2-}, Ca^{2+}, Mg^{2+} and MSA) concentration as well as $\delta^{18}O$ and ^2H-excess values will be presented in the following figures. Some measured species, like ammonium, bromide and fluoride, showed poor data quality and will not be presented. For reasons of clarity and compactness in this paragraph we show two plots of IP1 and the results of IP2, IP3 and IP4 as average values. Graphics of every single sampling day from IP1 to IP4 can be found in the appendix. Both Fig. 11 and Fig. 12 show typical patterns that mirror in most of the daily snow liners of IP1.
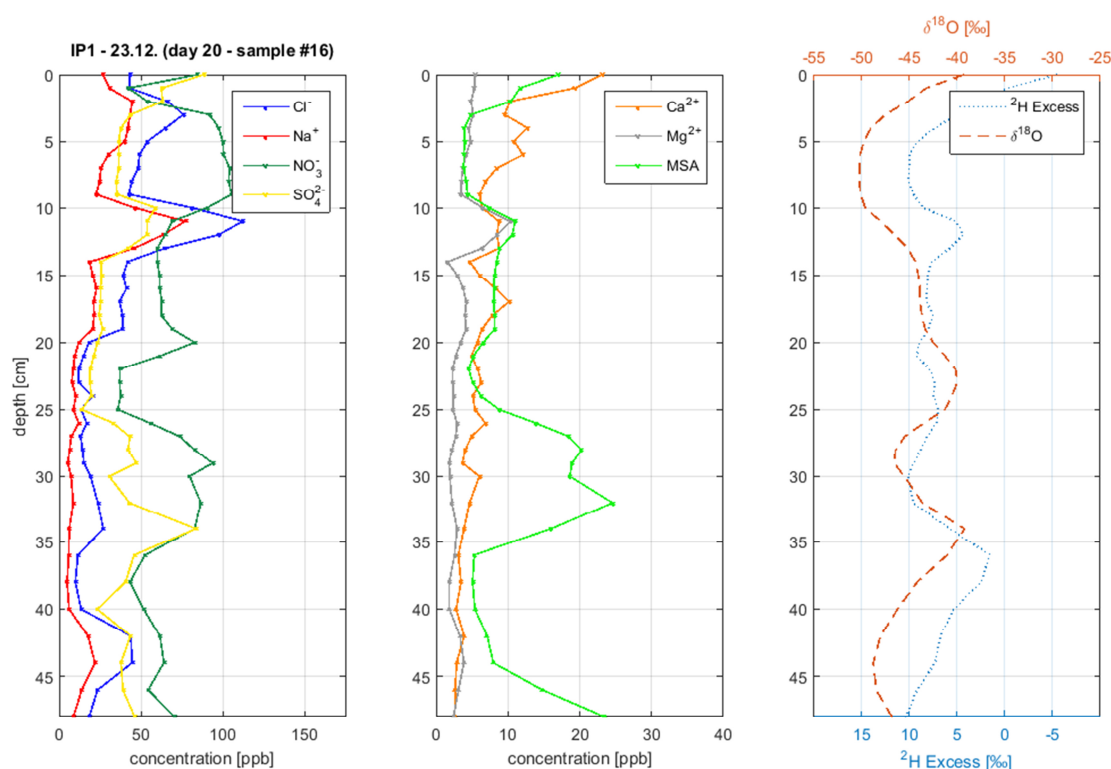
Fig. 11: The two panels at the left and in the middle of this figure show measured concentrations of ion species of sample #16 (comp. Fig. 8) at location IP1, right panel shows $\delta^{18}O$ and ^2H excess. The depth scale on y-axis is identical for all panels. It starts with 0 cm (snow surface) and ranges to 48 cm (top of the last sample per snow liner) with annotations in steps of 5 cm each. Ion species with generally higher concentrations (Na^+, Cl^-, NO_3^- and SO_4^{2-}) are plotted on the left panel, species with lower concentrations (Ca^{2+}, Mg^{2+}, MSA and NH_4^+) in the middle panel. Concentration in parts per billion [ppb] is denoted on the x-axis. Every ion is depicted with a different color; key is placed in the top right corner of each panel. In the right panel $\delta^{18}O$ is shown in red dashed line with according x-scale on top of the panel, deuterium excess in dotted blue line with its scale at the bottom. Mind that the deuterium excess scale is inverted as $\delta^{18}O$ and ^2H-excess show a negative correlation. Both values are given in per mill [‰]. Na^+ and Cl^- show their highest concentrations here around 11 cm depth and pretty constant values between 20 cm and 50 cm depth. Similar behavior with even less variation shows Mg^{2+}. Also sulfate and MSA concentrations seem to run parallel, whereas the sulfate peak in depth of 35 cm is not as wide as the MSA peak. Sulfate maximum coincides with the end of the MSA maximum between 30 cm and 35 cm. $\delta^{18}O$ has a double peak structure with maxima between 20 cm and 25 cm as well as between 30 cm and 35 cm.
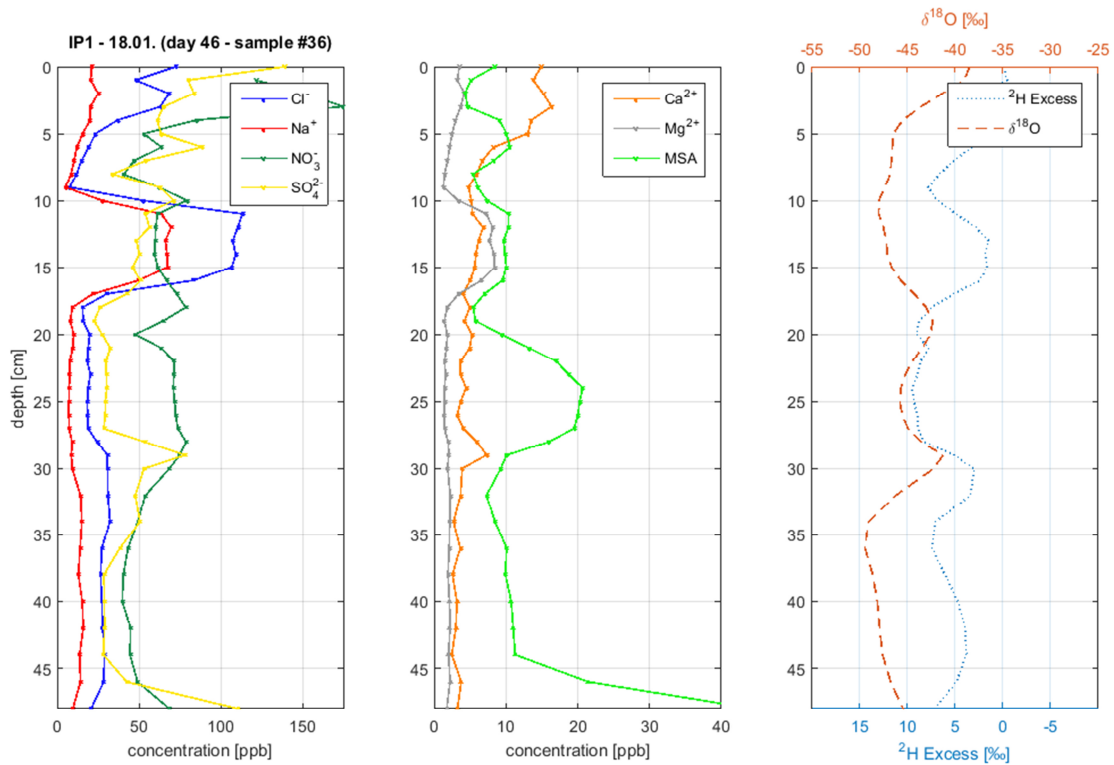
Fig. 12: Daily plot of sample #36 at location IP1 (comp. Fig. 8) confirms several trends observed in sample #16. Axis depiction and scale of this figure are as the same as for Fig. 11. Na$^+$ and Cl$^-$ peak around 12 cm depth is a bit wider than observed in sample #16. Chlorine concentration is constantly slightly above sodium concentration. Again sulfate species run parallel while sulfate peaks seem to coincide with the end of wide MSA maximum. Both sulfate species maxima plot in lower depth than in sample #20. Mg^{2+} peak can be observed at the same depth as Na$^+$ and Cl$^-$. Nitrate shows several peaks and keeps a high level concentration throughout the profile. On the right, again the double peak structure of $\delta^{18}O$ is recognizable. In general the deuterium excess run is subject to high variation. While the $\delta^{18}O$-pattern is highly regular in all IP samples, ^2H-excess patterns may also fluctuate on small scales with sharp gradients. Nevertheless, coherence between $\delta^{18}O$ and ^2H-excess is observable. In the interval of the double peak and below, the deuterium excess seems to be in phase with the $\delta^{18}O$ values while above (0 cm to 15 cm) in some parts both are anti-correlated.

Na$^+$ and Cl$^-$ concentrations show uniform patterns throughout most of the profiles. Their maxima plot in an interval between 9 cm and 17 cm depth. Below, both show pretty constant values between 20 cm and 50 cm with a slight increase at 30 cm depth. Similar behavior with even less variation shows Mg^{2+}. The runs of Na$^+$, Cl$^-$ and Mg^{2+} coincide well. Ca^{2+} has its highest concentrations at the surface, which may be caused by contamination. Further in the profile, the concentration is constant or steadily decreases with a very small peak between 9 cm and 17 cm. Sulfate and MSA concentrations both show a peak in similar depth intervals. Sulfate maxima are in the range of 27 cm to 38 cm depth, while MSA plots in slightly lower depth between 20 cm and 36 cm. It is recognizable that the sulfate peaks seem to start at that point where MSA peaks decrease. Sulfate also shows high concentration at the surface. MSA, on the other hand, has high maxima at the bottom of the outer-left and outer-right snow liners. Nitrate seems to run completely independent from other species with constantly high values. $\delta^{18}O$ run stars with high values at the surface continuing with a low around 7 cm depth. Between 20 cm and 35 cm depth, the curve has a double peak structure with maxima between 20 cm and 25 cm

as well as between 30 cm and 35 cm. This structure is visible in most of the daily plots. Deuterium excess, in contrast to δ^{18}O, shows high variations and has its minimum at the snow surface. The anti-correlation between δ^{18}O and ^{2}H-excess is recognizable at the very top of the snow liners and at the lower part between 20 cm and the bottom. Between 10 cm and 20 cm the signal in many profiles is diffuse.
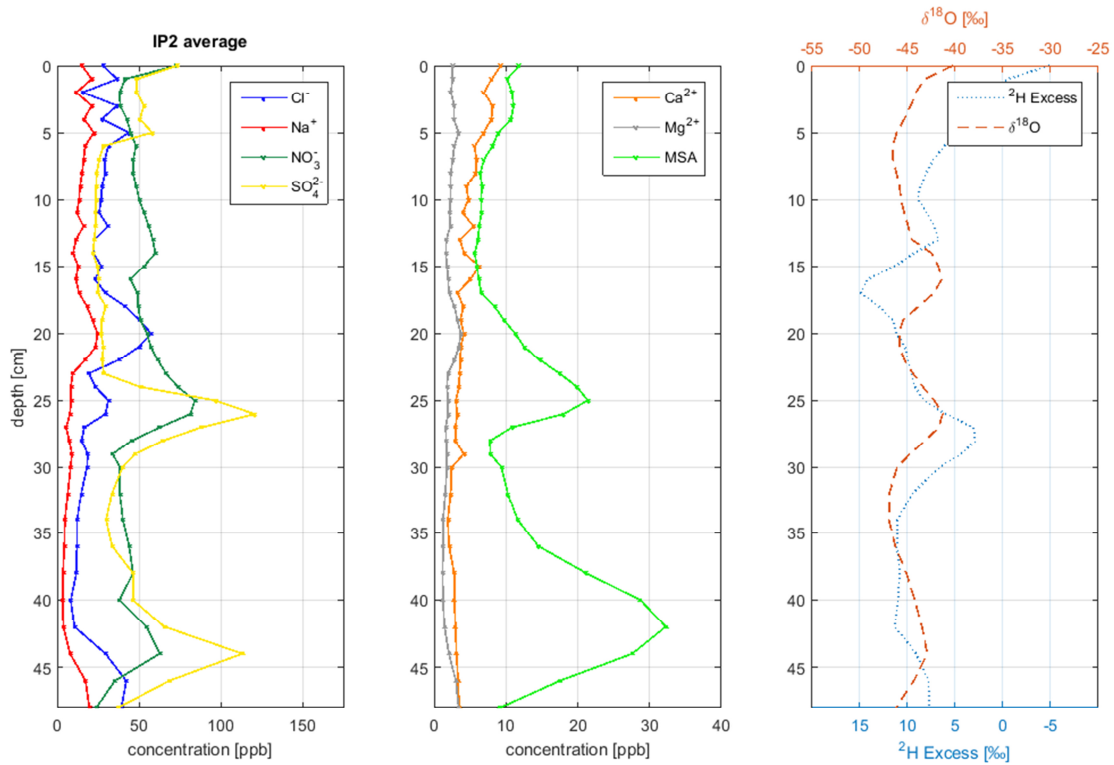
Fig. 13: In samples of location IP2 the sodium and chlorine signal at the top, which is prominent in IP1, is not clearly visible, just a minor peak can be observed. Elevated concentrations of Na$^+$ and Cl$^-$ can be seen in depth of 20 cm. The pattern of nitrate coincides well with IP1 plots. The run of sulfate shows a peak around 25 cm depth, the MSA peaks are in 25 cm and 42 cm depth, which is similar to IP1 snow liners. They have a similar intensity but a more narrow range than seen at IP1. δ^{18}O signal does also show the double peak structure as seen before with high values at the top, at the bottom and two related peaks at 15 and 25 cm depth. Inversed deuterium excess runs parallel to δ^{18}O signal. For axis and annotation explanations see Fig. 11.
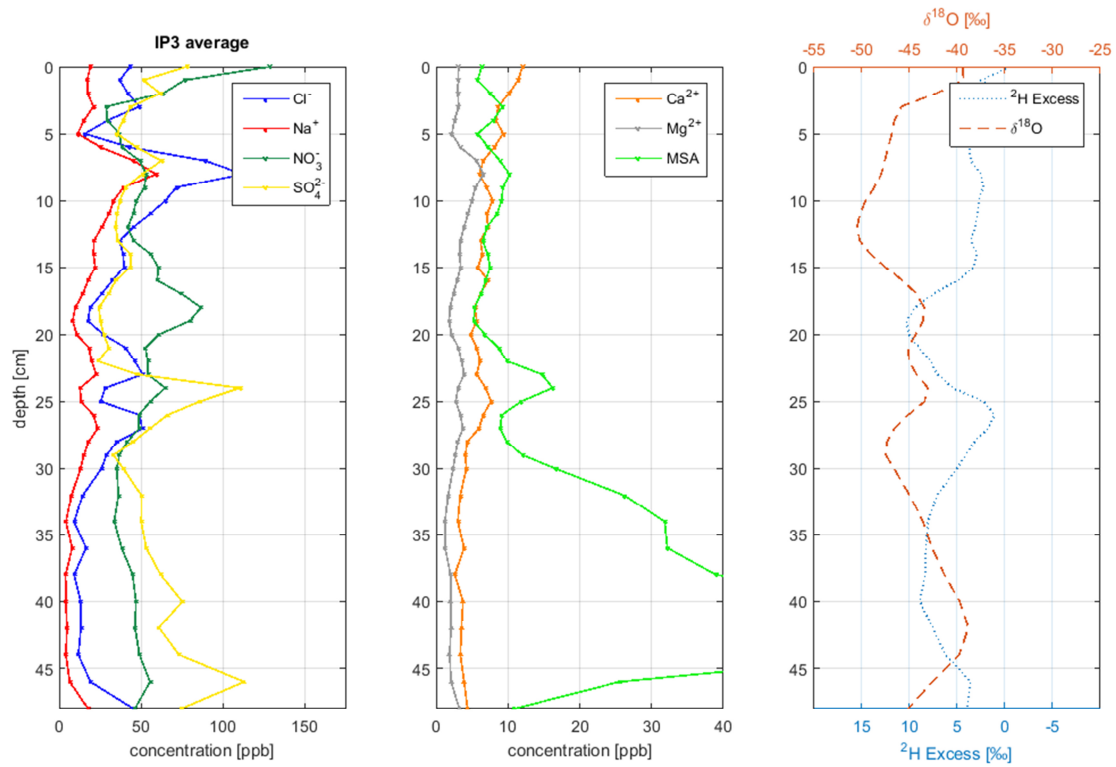
Fig. 14: In IP3 samples Na⁺ and Cl⁻ peaks plot between 7 and 13 cm depth. Like in IP2, another peak structure is visible between 20 and 30 cm depth. Nitrate shows continuously high levels as in every IP location. Sulfate and MSA show the same regular trends as seen before. Whereas MSA peaks in medium depth are slightly lower and at the bottom very much higher than previously seen. δ¹⁸O plot has some differences to the previous ones. The minimum around 10 cm depth has more negative values and the maximum around 40 cm depth more positive values than samples at other locations. The double peak structure in the middle is pretty narrow. Deuterium excess in IP3 seems to be in disharmony with δ¹⁸O unlike in other previously mentioned samples. For axis and annotation explanations see Fig. 11.
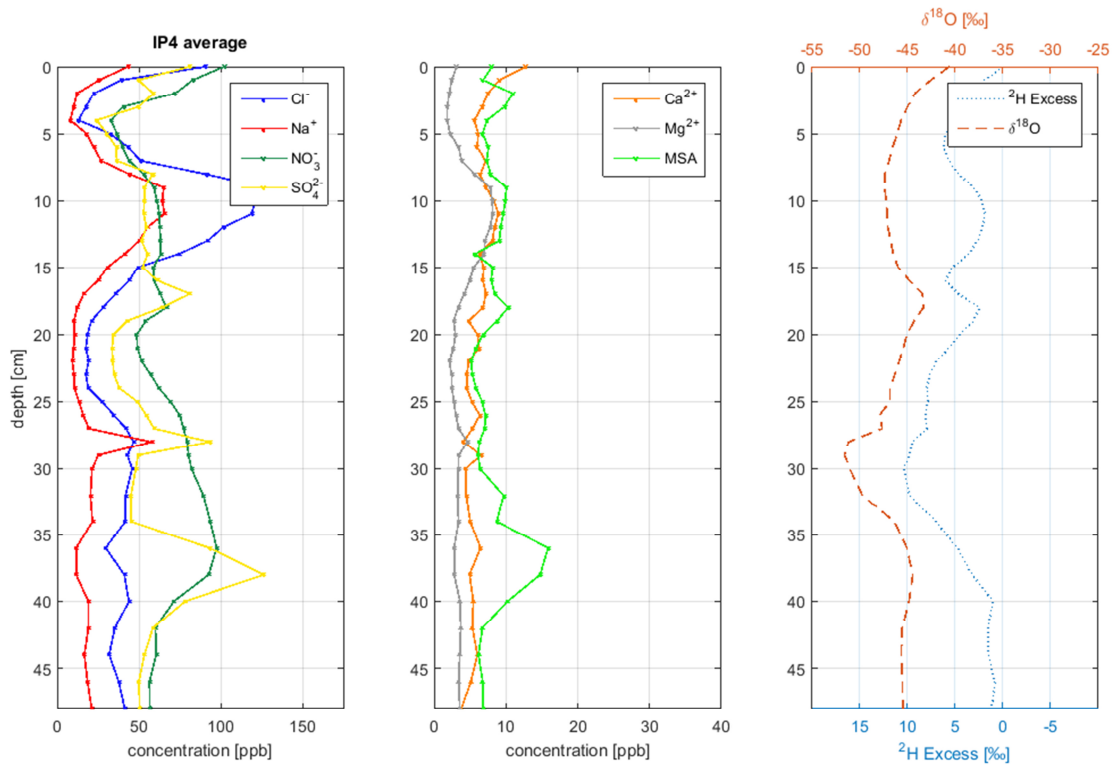
Fig. 15: High Na^{+} and Cl^{-} values at the top of the profiles in IP4 are visible. Increased values around 30 cm occur only in IP4. Mg^{2+} stays constant over the whole snow liner as in IP2 and IP3 with slightly increased values at 10 cm, which is parallel to Na^{+} and Cl^{-}. In IP4 samples there are differences in MSA concentrations. Peaks seem to be shifted upwards and maxima do not show that high intensity. Double peak in $\delta^{18}O$ structure cannot be found at this location, only one peak between 15 and 20 cm is measured. Nevertheless, close harmony between $\delta^{18}O$ and inverted ^2H excess can be observed.

Trace elements

After the overview graphics, we will now present species-dependent graphics with results from location IP1. The figures represent a cross section through the snow column and are color-coded. Bright colors represent high values while dark colors represent low values. For comparison, distinct snow liners, which are presented in Fig. 11 and Fig. 12, are highlighted in the following Fig. 16 - Fig. 21 with red frames. Average values of IP2, IP3 and IP4 are given in Table 1.

Sodium, chlorine, magnesium and calcium

In the snow liner profiles, Na^{+} and Cl^{-} show clear signals with a peak between 5 cm and 20 cm depth (s. Fig. 11 and Fig. 12), in some profiles even increased values between 0 cm and 5 cm. Peaks are diffuse in samples #1 to #11 but get clearer from sample #12 to the end (s. Fig. 16). Maximum width of the peak is 9 cm, thinning to 4 cm width at the end of the profile. Concentration of sodium and chlorine stays constantly low after a slight increase around 30 cm to 40 cm depth. Average concentration of chlorine in IP1 is 42.39 ±32.18 ppb. Values over 175 ppb were considered as outliner and neglected while even values up to 490 ppb for chlorine were measured. High outliner are confined

to distinct days which can be an indicator for contamination of the whole liner (s. Fig. 16, yellow fields). In general Cl^- shows slightly higher concentrations than Na^+ (comp. Fig. 12). Sodium average concentration is 24.57 ± 22.31 ppb. Little amount of sodium samples show concentrations above 150 ppb. Again values over 175 ppb were considered as outliner.
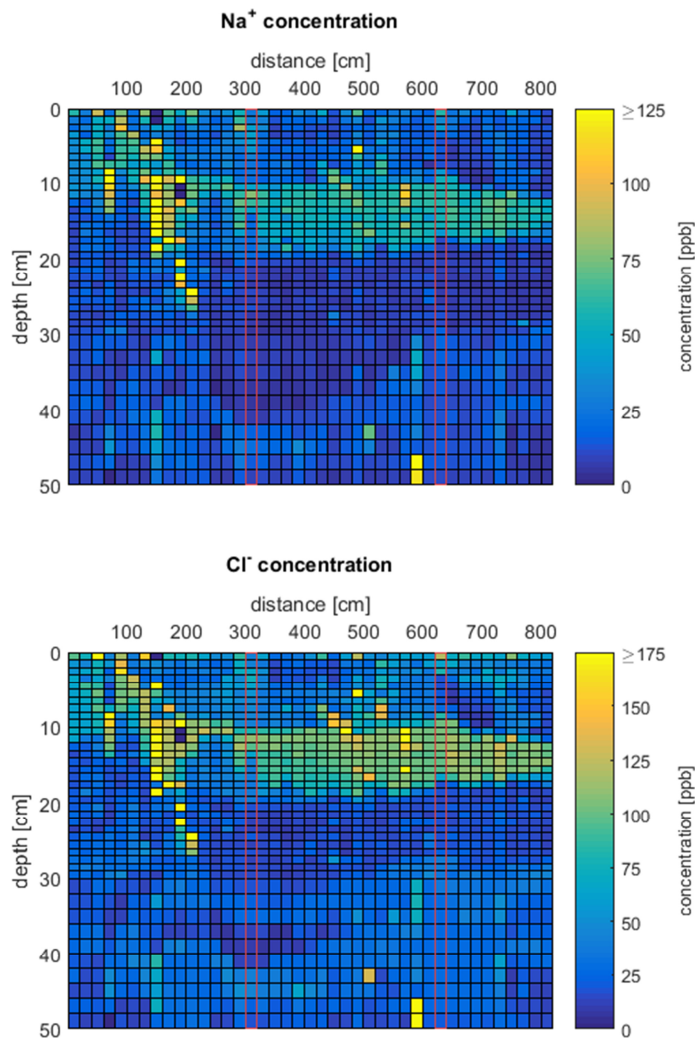
Fig. 16: This color intensity plot shows a vertical profile of IP1 with concentration distribution of one ion species. On the x-axis the distance in steps of 20 cm is notated, equal to the distance between consecutive samples. The y-axis shows the depth from 0 cm (snow surface) to 50 cm. Each vertical column therefore stands for a complete snow liner. Concentration is transferred into a color scale in which dark blue colors symbolize low, bright yellow colors high values (comp. colorbar on the right). In the upper panel sodium concentration is plotted, in the lower one, chlorine concentration. Both species show a layer with increased concentrations in the upper half of the profile. From left to right the lens seems to start at the surface and move downwards between 10 cm and 20 cm depth. At the end it thins out at the right side of the profile. Minimum values can be seen directly below the high concentration lens. It is notable that the lower horizon of Na^+ minimum area drops to 40 cm depth after 240 cm horizontal distance while the lower horizon of Cl^- minimum area stays around 30 cm depth. In this figure the high values at the left side of the profile can be seen clearly which is probably due to contamination.

Magnesium shows similar behavior as chlorine and sodium. Higher values than average can be observed at the same positions as peaks of Cl^- and Na^+ (s. Fig. 11 and Fig. 12). Outliner as well are

limited to certain days. Sample #11 had to be neglected completely due to contamination. Mg^{2+} average concentration is 4.33 ±3.06 ppb. Higher values than 18 ppb were again neglected. Calcium has an average of 8.33 ±9.85 ppb and seems to be very susceptible for contamination. Especially the first twelve samples of IP1 show unlikely high concentrations in the upper 20 cm (s. Fig. 17, yellow fields). As these high values stop abruptly after sample #12 it is very likely attributable to contamination. In most snow liner profiles calcium concentration decreases steadily from top to bottom. Dependent on the initial concentration at the top the decrease can be intense or moderate.

In general data quality for ions Na^+, Cl^-, Mg^{2+} and Ca^{2+} is better in samples #12 to #41 than from #1 to #11 due to contamination, as mentioned before.
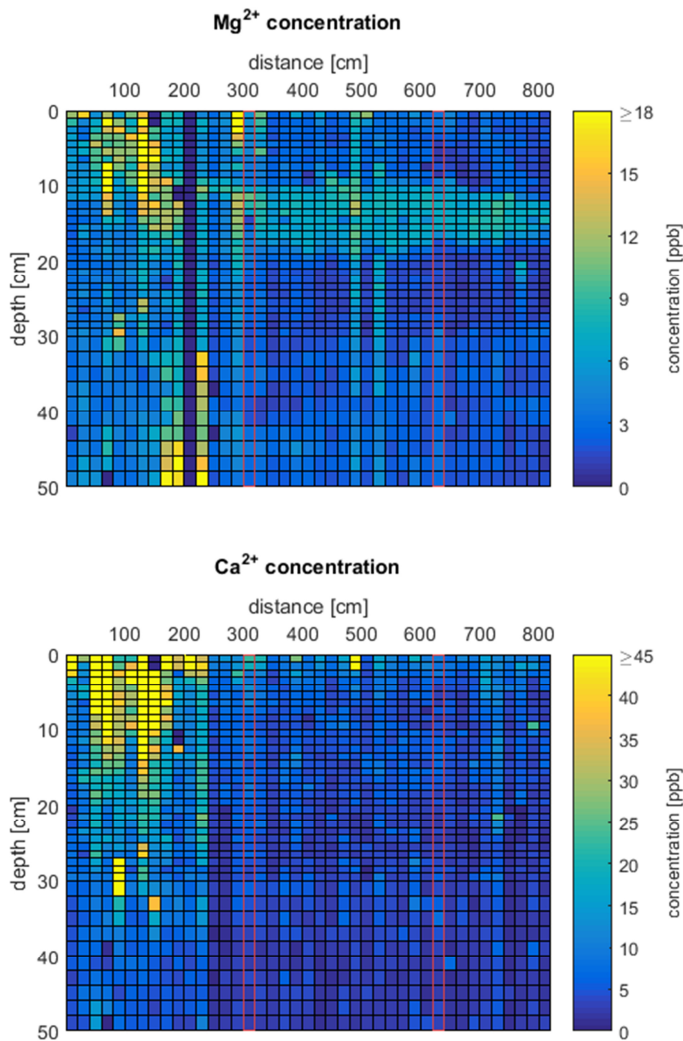
Fig. 17: The color intensity plot for magnesium (upper panel) reveals high similarities to sodium and chlorine. A lens with high concentrations is visible between 10 cm and 20 cm depth, thinning out at the right end and moving towards the surface at the left part. Minimum concentration area stops at about 30 cm depth similar to Cl⁻. Calcium (lower panel) on the other hand does not show similar patterns like sodium, chlorine and magnesium. Slightly higher values at the top than at the bottom of the snow liner can be recognized. First eleven samples seem to be victim of contamination, especially at the surface. See Fig. 16 for axis and annotation explanations.

Sulfur species (sulfate & methanesulfonate)
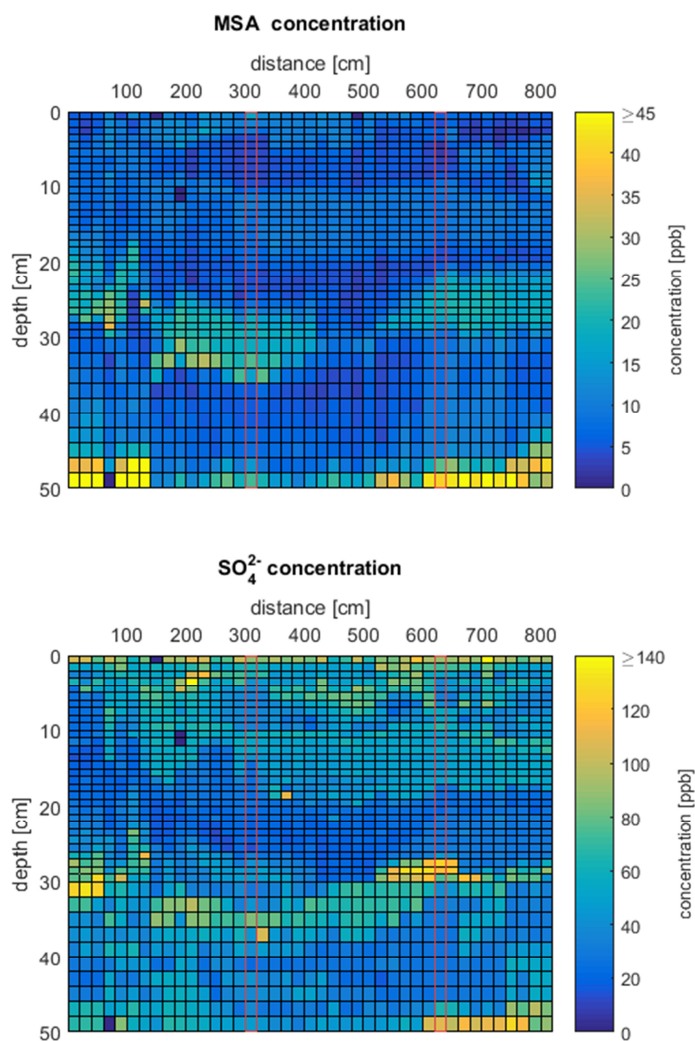
Fig. 18: Maximum concentrations of up to 70 ppb of MSA (upper panel) can be found at the bottom of the snow liner, especially at the left and right part of the profile. The second maximum is located between 20 cm and 36 cm depth with a slightly bent structure. Three areas of high sulfate (lower panel) concentration can be seen in this plot. Highest concentrations occur at the surface of the snow liner. First centimeter of every liner shows high sulfate content. Other areas of high sulfate concentration coincide with MSA. At the bottom of the profile at the left and right end the general concentration is increased. As well the along the horizon between low and high concentration areas in depth of 30 cm the sulfate content is very high. This sharp boundary is unique as no other ion species shows that abrupt transitions between high and low concentrations. Both MSA and sulfate seem to have a lens of intermediate concentrations between 10 cm and 20 cm depth. See Fig. 16 for axis and annotation explanations.

The highest concentration of MSA can be recognized at the bottom of the vertical profiles (s. Fig. 12 and Fig. 18). Peaks in the depth of 50 cm reach concentrations of 50 to 70 ppb. The second maximum can be seen between depth of 18 cm and 35 cm. This maximum reaches values around 15 ppb but can also exceed 30 ppb. Total average of MSA is 10.02 ±6.96 ppb. Sulfate shows higher values than MSA with an average of 45.15 ±21.11 ppb but no extreme outliner occur. It seems to run very parallel with

the MSA concentration (s. Fig. 18). Sulfate does not fall below 12 ppb. It is notable that the uppermost sample (0 to 1 cm) of all snow liner shows increased concentration of sulfate (89.5 ppb).

Nitrogen species (nitrate & ammonium)

Average nitrate concentration of IP1 is 67.63 ±22.28 ppb (IP2: 50.77 ±13.70 ppb; IP3: 52.50 ±19.42 ppb; IP4: 64.24 ±19.48 ppb). Highest values exceed even 150 ppb and are determined in upper 5 cm (s. Fig. 19). Whether this can be explained with contamination or the high values are a interpretable signal will be discussed in the next paragraph. In contrast to other species, nitrate shows a various number of peaks along the snow profile which does not seem to run parallel to any other pattern (s. Fig. 11). Also notable is the fact, that the conentration never falls below 25 ppm.

The data quality of NH_4^+ is very poor. The average concentration of ammonium can be stated with 1.3 ppb although a lot of data gaps exist. For this reason, NH_4^+ concentrations will not be discussed or taken as data basis.
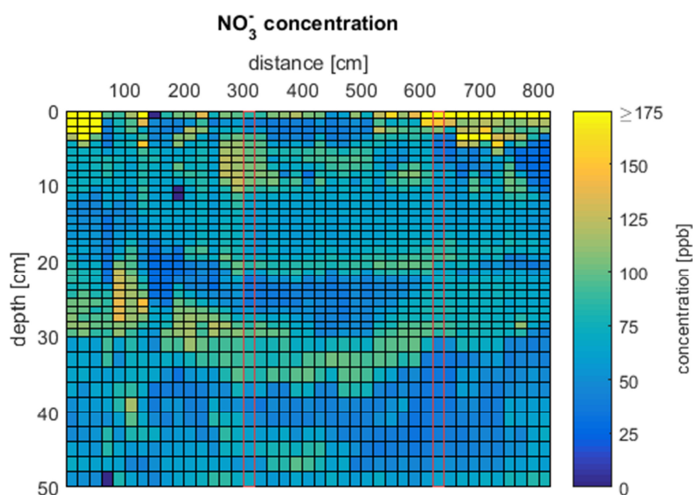
Fig. 19: Nitrate concentration in color scale is shown in this figure. As mentioned in the text, it is conspicuous that NO_3^- is constantly on a higher level than 25 ppb. Highest concentrations occur close to the surface in the upper 4 cm. General patterns of nitrate are similar to sulfate. An area of higher concentration is found between 25 cm and 35 cm depth with a slightly bent structure. Above, a secondary high-concentration layer is visible with large spatial coverage. See Fig. 16 for axis and annotation explanations.

Table 1: Average values of locations IP1 to IP4 for trace elements, isotopes and density are summarized here.

	IP1	IP2	IP3	IP4
Na^+	24.57 ±22.31 ppb	12.67 ±7.04 ppb	17.99 ±12.67 ppb	25.15 ±21.08 ppb
Cl^-	42.39 ±32.18 ppb	27.43 ±14.41 ppb	36.66 ±23.63 ppb	47.10 ±34.73 ppb
Mg^{2+}	4.33 ±3.06 ppb	2.17 ±0.85 ppb	2.99 ±1.35 ppb	3.86 ±2.03 ppb
Ca^{2+}	8.33 ±9.85 ppb	4.33 ±2.45 ppb	6.11 ±2.86 ppb	6.27 ±2.39 ppb
SO_4^{2-}	45.15 ±21.11 ppb	44.21 ±27.24 ppb	50.67 ±22.36 ppb	54.27 ±24.61 ppb
MSA	10.02 ±6.96 ppb	12.06 ±7.10 ppb	15.96 ±16.81 ppb	8.07 ±2.84 ppb
NO_3^-	67.63 ±22.28 ppb	50.77 ±13.70 ppb	52.50 ±19.42 ppb	64.24 ±19.48 ppb
$\delta^{18}O$	-45.36 ±3.22‰	-44.48 ±2.15‰	-45.07 ±3.23‰	-46.06 ±2.47‰
δ^2H	-357.20 ±25.21‰	-348.26 ±17.17‰	-355.79 ±27.08‰	-363.68 ±18.23‰
^2H excess	5.70 ±3.46‰	7.61 ±4.50‰	4.62 ±3.27‰	4.77 ±3.05‰
ρ	0.37 ±0.05 g cm^{-3}	0.36 ±0.04 g cm^{-3}	0.35 ±0.05 g cm^{-3}	0.36 ±0.05 g cm^{-3}

Isotopes (δ^2H, $\delta^{18}O$, ^2H-excess)

Measured $\delta^{18}O$ values range from -37‰ to -53.5‰. Average value of all IP1 snow liner is -45.36 ±3.22‰. Three maxima in $\delta^{18}O$ can be recognized from the plots. First maximum occurs at the snow surface with values around -40‰. Just after the maximum values decrease to around -50‰. After the minimum, the second and third maximum occurs. In the first seven snow liners the double peak structure is existing but less prominent, with the second maximum being higher than the first one. In samples 8# to #28 the two peaks are clearly visible. From sample #29 to #41 the signal diminishes slightly as the difference between both peaks lowers. δ^2H shows a wide range from -295.1‰ to -416.1‰ with an average of -357.20 ±25.21‰. As the patterns of δ^2H and $\delta^{18}O$ are completely congruent, we forgo showing the δ^2H plot in this paragraph. It can be found in the appendix.

^2H excess of the snow liner at IP1 range from -6.7‰ to 13.6‰. Overall average is around 5.70 ±3.46‰. Although daily samples show a lot of variation in deuterium values, three areas with increased values and the same number with decreased values can be found. Lowest values with even negative numbers happen directly at the surface. Three maximum values can be found between 5 to 10 cm, 15 to 30 cm and 40 to 50 cm depth.
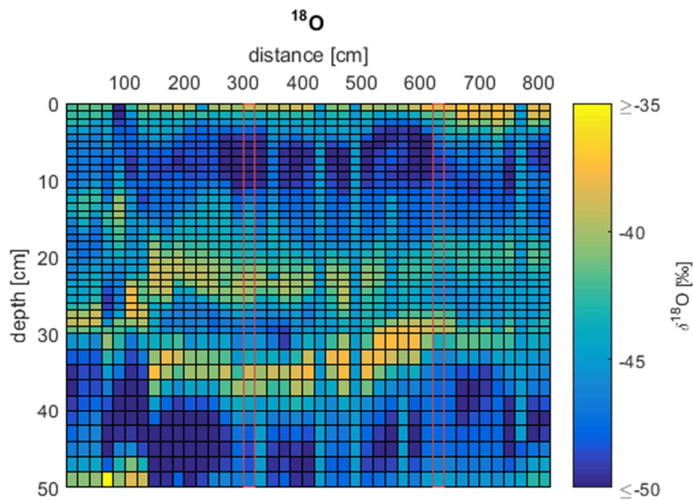
Fig. 20: The color intensity plot of δ¹⁸O again reveals the double peak structure between 20 cm and 40 cm depth- As in Fig. 16 to Fig. 19, horizontal axis displays the distance, vertical axis the depth in centimeter. Higher δ¹⁸O-values are symbolized by brighter colors, lower values by darker colors. Missing values for complete snow liner or intervals were treated with a value of -45‰. From top to bottom the profile starts with increased values around -39.8‰. Values decrease fast to almost -49‰ before the double peak structure appears. In the first seven samples the peak is not as prominent as in the rest of the profile. Below 40 cm depth the second minimum occurs before values increase slightly. Again, lenses seem to be bulgy with convex part towards the bottom of the profile.
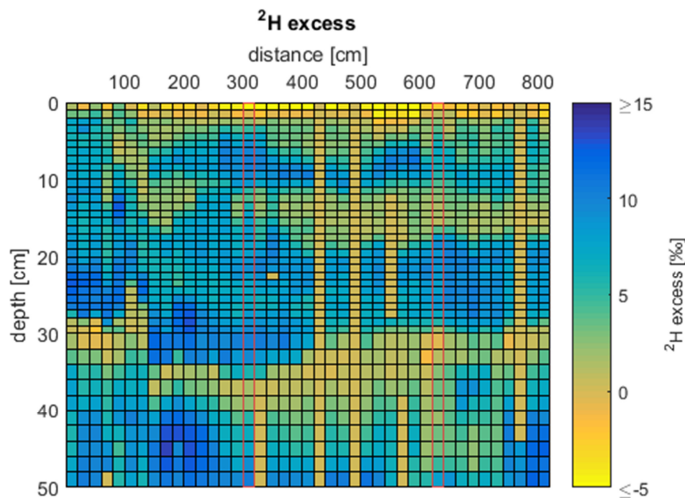
Fig. 21: In the deuterium excess color plot alternating areas with high and low values are visible. Mind that the color key is inverted as was the scale in previous plots. Bright colors represent low values whereas dark colors represent high values in this figure. Horizontal distance is depicted on the x-axis, depth in centimeters is depicted on the y-axis. Several intervals or complete snow liner have not been measured. For optical reasons, missing values were treated as 0‰. Three blue fading to green areas with values around 10‰ can be recognized. Transitions to adjacent orange areas with low deuterium excess values are smooth. Striking element in this plot are negative values in the uppermost samples, especially as the two other areas with low values do not show negative excess values.

Density
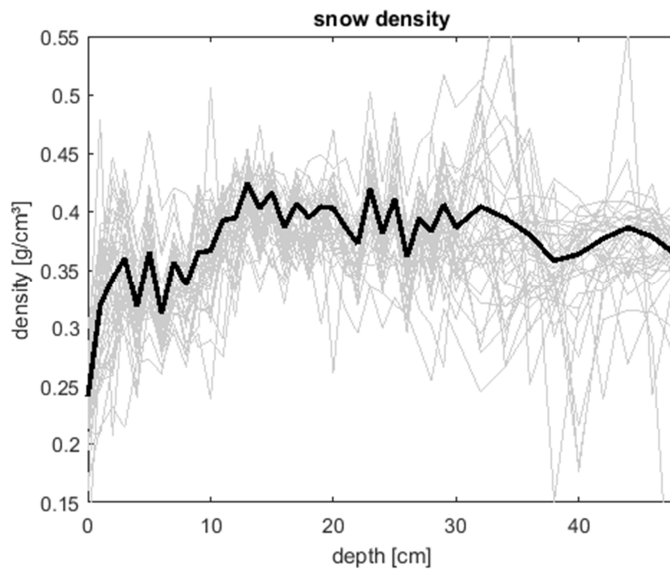
Fig. 22: Density data of snow liner at location IP1 are presented in this plot. Depth scale in this figure is on the horizontal axis from snow surface (left) to 50 cm depth (right). Vertically the density is depicted in g cm⁻³. Grey lines symbolize density trends within single snow liners. Grey area therefore also indicates the density intervals for each depth point. The black line is average density calculated from all IP1 snow liner. Fresh snow at the surface shows high values between 0.19 and 0.30 g cm⁻³. Density steadily increases to a depth of 14 cm. Surprisingly, in average density decreases again until the bottom of the snow liner.

Density values for all snow liner start around 0.24 g cm⁻³ for the first sample. Values increase rapidly until around 0.42 g cm⁻³ in 14 cm depth. Surprisingly, until 50 cm depth the density stays pretty constant or even decreases slightly. At the bottom of the snow liner average density is around 0.36 g cm⁻³. Variations among snow liner are pretty high on that small scale as can be seen in grey shaded lines in Fig. 22. Nevertheless, trends are similar as inferred from parallel slopes. Variations start to get radical after 30 cm depth. Values above 0.5 g cm⁻³ and below 0.25 g cm⁻³, as seen in a little amount of samples, should be due to mistakes during sampling or measuring the weight in the laboratory. Average density is 0.37 ±0.05 g cm⁻³.
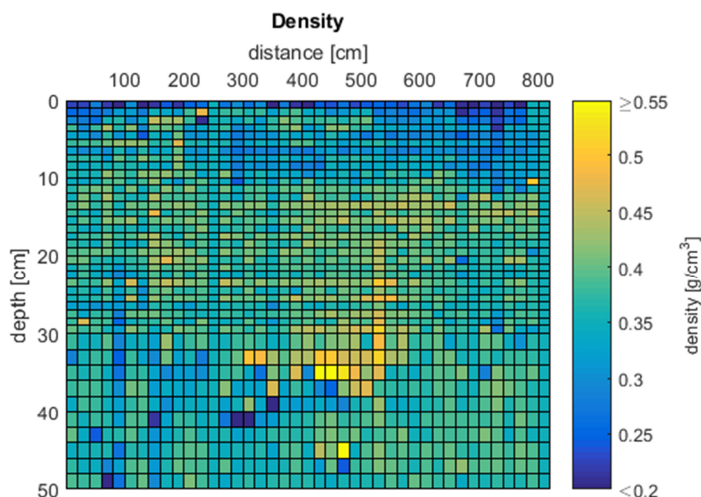
Fig. 23: Color density plot confirms the trend seen in Fig. 22. Low density at the surface increases until 14 cm depth and stays pretty constant until the bottom. With this figure we additionally get insights on the spatial distribution. High density values of the snow liner were measured in the middle of the horizontal profile between 400 and 600 cm distance to the first sample. Increase of densities continues in the middle of the profile to greater depth, highest densities concentrate between 25 cm and 40 cm depth. Like in some trace element plots, in this figure also a downward bent structure can be assumed.

DISCUSSION

Seasonal characteristics – temporal correlation

According to MÜNCH et al. (2015), for representative snow profiles at low accumulation sites several spatially independent samples are needed because the influence of small scale noise at single profiles can be very high. This is also observable in ion concentration profiles of, for instance, sulfate and MSA (s. Fig. 18). With respect to this, we calculated a spatial average from five samples of locations IP1 to IP4. Two samples from location IP1, with spacing of at least four meters, were taken to ensure spatial independence. As at locations IP2, IP3 and IP4 some samples lack of continuous isotopic data, we chose the sample with the best data record at each location (s. annotation of Fig. 24). Values are summarized in Table 4 and Table 5.

OERTER et al. (1999) suggested for the 20th century an accumulation rate interval of 63-74 kg m^{-2}a^{-1} while 64 kg m^{-2}a^{-1} established as standard. Recent field observations on ablation stakes at Kohnen station in season 2013/14 revealed increased accumulation of 29 cm, which is equal to 106 kg m^{-2}a^{-1} water equivalent (also referred to as 106 mm w.e.) based on calculated average density. It is under debate whether the increased accumulation is a real climate effect or to ascribe to the station building which causes a slight dune structure and favors deposition of drift snow around Kohnen (WELLER & KIPFSTUHL, 2016, pers. commun.). At least, model time series of accumulation suggest increasing accumulation for the late 20th century (NOONE et al., 1999). Nevertheless, for a time-depth correlation the more recent accumulation rate was used. For one thing, there is direct link to the samples and the increased accumulation would affect both, ablation stakes and the taken snow liners. For other thing, the increased accumulation better matches the data. We first applied a linear fit of time and depth with two reference points. The top of the snow liner samples was set as starting point representing the 1st January 2014 and, according to the accumulation rate, 29 cm depth of the snow liners was assumed as one year marker representing the 1st January 2013. Depth intervals in between and below were adjusted linearly, assuming a constant accumulation during summer and winter. Hourly temperature record was smoothed with a 48-hour running mean (s. Fig. 33).

We now presume Na$^+$ and Cl$^-$ as reliable proxy for winter and MSA and SO$_4^{2-}$ as proxy for summer months, while MSA deposition is limited to late summer (WAGENBACH, 1996; WAGENBACH et al., 1998a; WELLER & WAGENBACH, 2007; WHITLOW et al., 1992). High and low δ^{18}O values should match witch summer and winter seasons, respectively, as in other areas of Dronning Maud Land (KARLOF et al., 2005). Nonetheless, higher precision is guaranteed in high accumulation areas (LEGRAND & MAYEWSKI, 1997) and representativeness for low accumulation sites is estimated as poor (FISHER et al., 1985; KARLOF et al., 2006; MÜNCH et al., 2015).

In general, the linear fit for the trace element data with temperature seems solid (s. Fig. 33). Na$^+$ and Cl$^-$ peaks can be seen in austral winter with maximum in August. Sulfate maximum plots in late

austral summer. Unfortunately, MSA concentrations in IP1 to IP4 differ tremendously in the lower 20 cm and cannot be used as reliable tracer. Mean nitrate concentration stays continuously on a high level and is also not useful for time reference. On the other hand, summer maxima and winter minima of $\delta^{18}O$ do not plot as previously assumed. Especially high $\delta^{18}O$ is expected to coincide with high surface temperatures in December and January. Here, in Fig. 33, $\delta^{18}O$-maxima plot at the beginning and at the end of the season.

First impressions therefore suggest a strong seasonal dependent behavior of most analyzed species. A linear depth-time-fit might be good for a rough overview, but for precise dating we actually have to take the strong accumulation variability into account. As there is still lack of continuous records about accumulation distribution in Antarctica, for a rough estimate we have to refer to other sources. Grain size growth for snow grains is maximum in summer caused by high surface temperature and high temperature gradients (COLBECK, 1993). Recent satellite microwave investigations revealed that precipitation can disturb the grain growth. A link between accumulation rate and grain size growth postulated less than 1 mm w.e. for a period of 1.5 months during austral summer (PICARD et al., 2012). Field observations at Kohnen confirm very little accumulation whereas it is very difficult to determine an exact value on that scale (KIPFSTUHL, 2016, pers. commun.).

We now present a case study for a snow profile, which correlates depth and time with respect to seasonal accumulation variability. Due to the sampling resolution and to keep things simple, we assume an accumulation rate in summer of 0.5 cm snow each for December and January. This is equal to 1.83 mm w.e. per month and actually still too high for summer compared to findings of PICARD et al. (2012). Further, for the fit, accumulation between March and October was assumed as equally distributed and slightly decreased values were considered for November and February to avoid a sharp gradient in the plots. Again, in the end the 48-hour running mean temperature was added (s. Fig. 24).
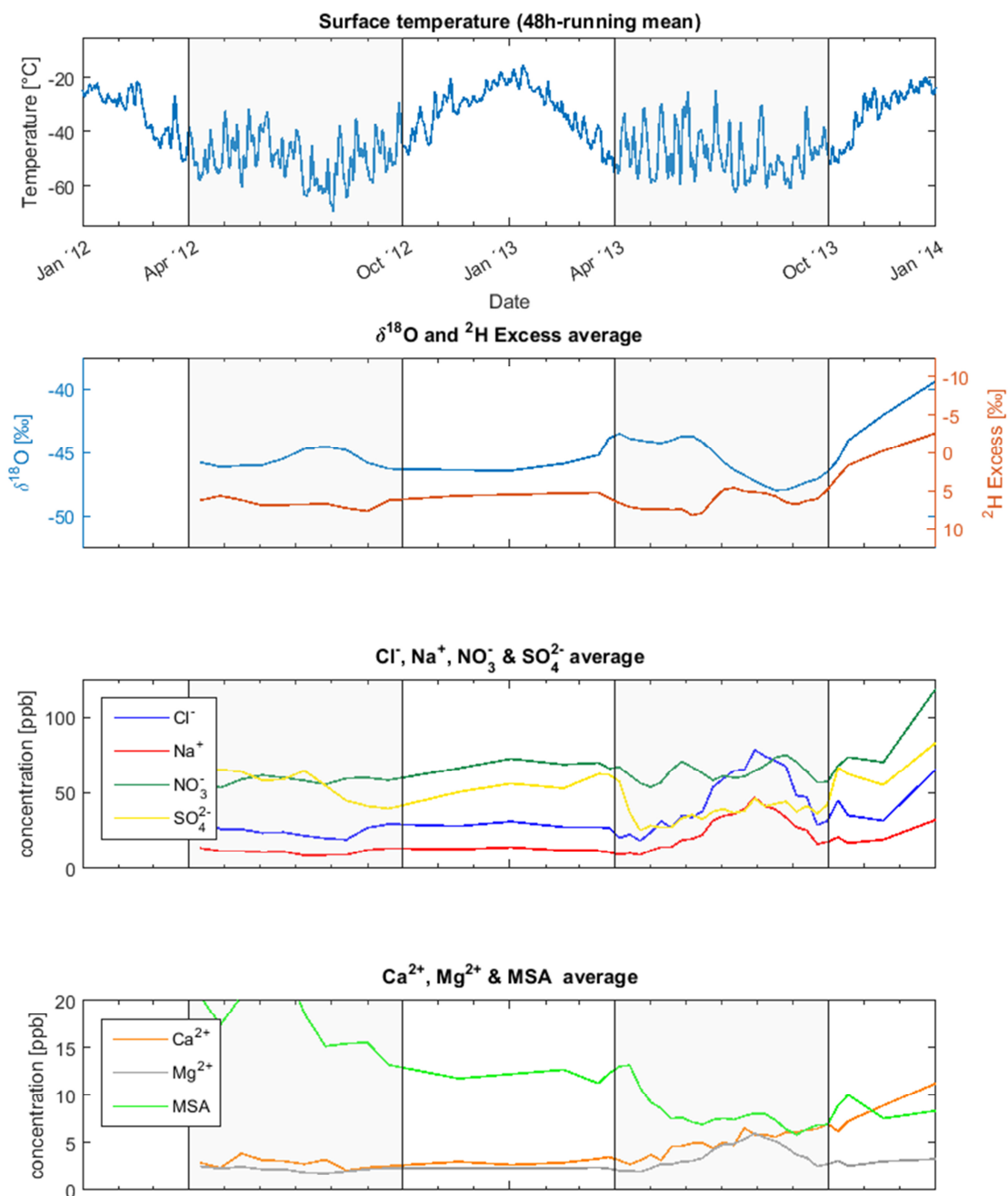
Fig. 24: For this figure, spatial average of five samples was calculated. We used samples #17 and #38 from IP1, sample #3 from IP2 and IP3 as well as sample #1 from IP4. On the vertical axis for all four panels the time interval between January 2012 and January 2014 is shown. The uppermost panel represents 48-hour running mean temperature at Kohnen station in degree Celsius. Summer temperatures stay constant around -20°C without high fluctuations. Winter temperatures can even exceed -60°C but accompanied by high fluctuations of over 30°C within several hours. Isotope plots are shown in the panel underneath. $\delta^{18}O$ plots in blue with its scale on the left, deuterium excess in red with scale on the right side. Ions are separated and presented with same color coding as before with concentration in parts per billion on the vertical axis. Shaded areas divide the years into periods of six months. Grey areas symbolize austral winter seasons (April to October). White areas represent calendrical austral summer months, whereas meteorologically only December and January are classified as summer.

In the following two chapters, the focus will be the on temporal fit of the spatial average as presented in Fig. 24.

Seasonal characteristics – $\delta^{18}O$, δ^2H, ^2H-excess

The maximum of $\delta^{18}O$ and minimum of ^2H-excess at the top of the snow liners fit with surface temperatures although they seem unusually high compared to values in the rest of the curve (s. Fig. 24). Effects that control these values will be discussed in detail in the next passage. From top to bottom, the first minimum (maximum) of $\delta^{18}O$ (^2H-excess) is expected slightly earlier in time referring it to temperature. While the temperature plot shows various fluctuations between April 2013 and October 2013, going further back in time the $\delta^{18}O$ curve steadily increases without any high oscillations. At this point it is important to mention, that the smooth trend in $\delta^{18}O$ is not a consequence of averaging (comp. daily plots in the Appendix or Fig. 27). Relatively high values for winter suggest close relation between $\delta^{18}O$ and positive short-term temperature fluctuations. The latter are mainly caused by cyclones in the Weddel Sea (TURNER et al., 1995) transporting warm marine air masses to Dronning Maud Land (NOONE et al., 1999; REIJMER et al., 2002). These synoptic patterns initiate high-precipitation events, which favor cloud forming and wet deposition (WELKER et al., 2014). Also diffusion of isotopes within the firn matrix may explain the smooth trends observed in every $\delta^{18}O$ profile (VAN DER WEL et al., 2015). High $\delta^{18}O$ in winter can also be product of wind pumping within the firn column, which is said to have an even higher impact on postdepositional alteration of $\delta^{18}O$ (TOWN et al., 2008). Thus, the small-scale fluctuations in Antarctic climate cannot be resolved in $\delta^{18}O$ or ^2H-excess due to the smoothing causes mentioned above.

From firn core records of $\delta^{18}O$ and δ^2H we know the sinus-shaped, seasonal patterns that mirror the temperature of the past (STEEN-LARSEN et al., 2011). The run of $\delta^{18}O$ and ^2H-excess in summer does completely not show this picture. Besides, this is not only an effect of the stretched plot as this feature can also be seen in the linear fit (comp. Fig. 24 and Fig. 33). Low $\delta^{18}O$ values at least cannot be explained here with high surface temperature. Interestingly, after the extended low in $\delta^{18}O$ during summer, values increase again, which does not fit to the temperature curve.

Average δ^2H-excess of the first sample is -2.76‰, which is surprisingly low. In general, low deuterium excess values can be expected from marine air in Antarctica in austral summer (comp. Fig. 7). Modeling of δ^2H-excess in evaporation of Antarctic ocean between December and February state 3-10‰, while between June and August it rises to 12-18‰ (PFAHL & SODEMANN, 2014). Compared to possible ^2H-source suggested by the model, the measured values at the snow surface are still very low. On the other hand, fresh snow usually shows relatively high deuterium excess while evaporation and sublimation effects alter the signal towards negative values. Decreasing ^2H-excess and increasing $\delta^{18}O$ is a postdepositional pattern as ^2H is in favor versus ^{18}O of moving to the evaporate or sublimate phase (STEEN-LARSEN et al., 2014). This effect is empirical tested with snow samples at

Kohnen (KIPFSTUHL, 2016, pers. commun.). Assuming exhibition time of snow at the surface in summer to be very high (PICARD et al., 2012), isotopic fingerprints of snow samples in the top centimeters of the profile run congruent to that observation. With increased residence time at the surface, the excess of ^{2}H gets more and more prominent resulting in negative values. A fresh snow accumulation event, which was not recorded in the field campaign, proves this theory as well. In δ^{18}O (s. Fig. 20), deuterium excess (s. Fig. 21), Na$^+$/Cl$^-$ratio (s. Fig. 26), SO$_4^{2-}$ (s. Fig. 18) but remarkably in NO$_3^-$ (s. Fig. 19) we recognize a prominent deposition event in concentration and ratios close to the surface at top right of the figures. Deuterium excess (δ^{18}O) is decreasing (increasing) in contrast to the same depth in snow liners previously taken. This is an indicator for fresh snow deposition as the residence of snow at the surface was minimal. Interestingly, this theory seems not to apply to snow in summer 12/13, which shows, compared to summer 13/14, quite high deuterium excess. Additionally, coherence between increased aerosol concentrations (in this case Na$^+$/Cl$^-$, NO$_3^-$ and SO$_4^{2-}$) and δ^{18}O suggests a strong coherence between accumulation and the real deposition signal of δ^{18}O on the snow surface.

In general, deuterium excess is said to be dependent on surface temperature, relative humidity as well as wind speed. With these parameters it is also transferable to moisture source regions as modelled by JOUZEL & MERLIVAT (1984). Local temperature seems to have a high impact on deuterium excess (FERNANDOY et al., 2012), especially fast drops in austral winter coincide well with increased ^{2}H-excess. UEMURA et al. (2008) suggested a negative correlation for relative humidity and deuterium-excess. At least this relation cannot directly be confirmed for synoptic weather patterns with high accumulation events (NOONE et al., 1999). The dependence on wind direction for Kohnen station will not be checked as data from the weather station seem not to be reliable. Distinct changes in wind direction are not expected in DML (TURNER et al., 1995). But nevertheless, it is worth observing for future surveys especially in winter in relation to high temperature fluctuations. In general deuterium excess seems to be much more sensitive to short term climatic changes than δ^{18}O. On one hand this is logical due to thermodynamic differences, on the other hand also due to a broader variety of processes controlling the signal (PETIT et al., 1991). Nevertheless, based on the dataset and considering fast modification of the deuterium excess signal by sublimation at the surface (STEEN-LARSEN et al., 2014), at Kohnen ^{2}H-excess is not a reliable tracer for climatic conditions. To what extent that has influences on the reliability on δ^2 is not clear, yet.

Analyzing related δ^{18}O and δ^2H values, which was not graphically presented so far, reveals their strong linear coherence as expected (s. Fig. 25). δ^{18}O/δ^2H-pairs plot on or close to GMWL (s. Isotopes) but the slope of the trendline is lower than for GMWL. Samples at Kohnen therefore are characterized by an evaporational regime (SAHRA, 2005) as it is likely for arid regions (JASECHKO et al., 2013; YUAN et al., 2011). Postdepositional sublimation and evaporation are dominating processes at the surface, what can also be confirmed by the data. Interestingly, the graphically derived deuterium

excess for samples of IP1 is -4.78. It is by far lower than modelled for the GMWL. The weighted deuterium excess average 5.70±3.46‰ for IP1 is distinctly higher.
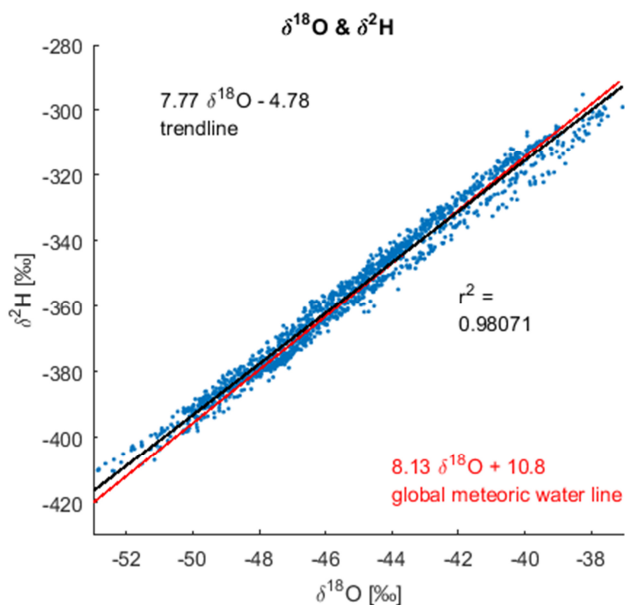
Fig. 25: Strong linear correlation can be seen between $\delta^{18}O$ and $\delta^{2}H$ with a coefficient of determination of 98.07%. $\delta^{18}O$-values are denoted on the horizontal axis and $\delta^{2}H$-values on the vertical axis in per mill. Blue dots symbolize oxygen and hydrogen isotopic pairs as their composition in snow samples of IP1. Black line represents the trend line with a slope of 7.77 and y-intersect of -4.78. In contrast, the GMWL is plotted in red with slope deuterium excess of 10.8 (ROZANSKI et al., 1993). On one hand, the data points plot very close to each other and also very close to the global meteoric water line. On the other hand, the calculated deuterium excess for these samples is very low compared to the standard of the GMWL. This is interesting as the measured average deuterium excess is only 5.70 ±3.46‰. The lower slope of the trendline for investigated samples indicates strong evaporation or sublimation at the snow surface.

We conclude from comparing both isotopic curves with the temperature record that on small scale (seasonal resolution) $\delta^{18}O$ does not match well with surface temperature record. Especially summer patterns suggest high dependence on accumulation, as the temporally fitted curve does not show a specific summer signal. Also high temperature oscillations accompanied by high-precipitation events in contrast to the smooth isotopic record with high $\delta^{18}O$ values implicate strong relation to short term climate variations and strong dependence on accumulation (PERSSON et al., 2011). Of course, snow drift and other postdepositional alteration processes (KARLOF et al., 2005; TOWN et al., 2008; VAN DER WEL et al., 2015) are also an important factor and will be discussed later.

Seasonal characteristics - aerosols

Compared to the isotopic signals in the temporal fit, peak patterns of measured aerosols do plot as expected. High variation at the surface and the bottom as for the isotopes disturb the overall picture. Contamination cannot be excluded but seems to be more likely at the top (CAIAZZO et al., 2016) as all ion species increase rapidly. At the bottom normally only some species show increased values (sulfate and MSA), which is not surely ascribable to contamination.

Signals of sea salt components Na^+, Cl^- and even Mg^{2+} (winter), sulfur species SO_4^{2-} and MSA (summer) (WELLER & WAGENBACH, 2007) plot without significant shifts as observed in $\delta^{18}O$. The most reliable peaks show sodium and chlorine and, with less intensity, magnesium (s. Fig. 24). This is interesting, as these species seem also closely related to short term high-precipitation events caused by intruding marine air loaded with sea-salt aerosol (WELKER et al., 2014). Unfortunately, the summer signal of MSA in January 2014 is not present in the dataset. It was expected to deposit in late January

(WAGENBACH, 1996). On the other hand, it is not surprising if we consider minimum accumulation in summer and presume that MSA is tending to wet deposition (SHI et al., 2012). Also snow liners at the end of January did not show significantly increased MSA values (comp. Fig. 18) but sulfate shows an increase at the surface, which normally is harbinger of MSA. Nevertheless, the reliability of sulfur species is not as high as for sea salt as those aerosols normally are susceptible for postdepositional alteration (WOLFF, 1996a). Nitrate signals seemed to be useful as spring indicator in single samples, but in spatially averaged plots, the variation is too high and postdepositional alteration is very likely (MULVANEY et al., 1998; WAGENBACH et al., 1998b). For both sulfuric and nitrogenic species, the noise level is simply too high, which probably is caused by diffusion (WELLER et al., 2004).

Drift events and postdepositional processes

As mentioned before, spatial and temporal small-scale climatic events have high impact on the aerosol as well as the isotopic record (MÜNCH et al., 2015; PERSSON et al., 2011). In the spatial averaged overview in Fig. 24, smoothing of aerosol signals in particular cannot be avoided. Therefore we now take a look at daily samples and the horizontal intensity plots.

Sodium and chlorine concentrations for summer 13/14 are higher than for summer 12/13 (s. Fig. 11, Fig. 12 and Fig. 27). Average concentration in 0-9 cm depth at IP1 is 51.79 ppb for Cl^- and 24.53 ppb for Na^+. Values are significantly lower by 42.15% (Cl^-) and even 48.31% (Na^+) in 20-50 cm depth. On one hand, lower values can simply be explained with less total dust input in winter 12/13 but can also be signal of diffusivity and re-emission, although sodium is known as conservative species (WELLER & WAGENBACH, 2007). Mg^{2+} concentration, according to WHITLOW et al. (1992) solely limited to sea salt and a quite unreactive species, also shows a loss of 30.84%. Total input, including all species shown in Fig. 24, in winter 12/13 (162.41 ppb) is lower than 13/14 (282.94 ppb) by 42.6%. Compared to total dust inputs from winter 00/01 and 01/02 with roughly 402 ppb (PIEL, 2003), especially the input in winter 12/13 seems very low and cannot be solely addressed to postdepositional losses. Taking a closer look at intensity plots shows a detailed and extended horizontal profile visualizing seasonal layers with characteristic ion signals and isotopic fingerprints (Fig. 16 to Fig. 21, Fig. 23 and Fig. 26). While the winter layer with increased Na^+, Cl^- and Mg^{2+}, low $\delta^{18}O$ and a well-shaped lens structure is remarkably clear (as well as their following low or high, respectively, according to Fig. 24), along the 30 cm isohypsis in several species a more or less prominent horizon is visible. Especially in sulfate concentration the sharp transition from high to low values can clearly be seen in the color coding (s. Fig. 18, bottom). Taking a closer look into overview plot of sampling day 32, the sudden drop also appears in other species, especially nitrate, MSA and calcium as well as $\delta^{18}O$ (s. red stars in Fig. 27). Considering sharp transitions and the parallelism of sudden drops in several species as well as in IP2, IP3 and to a smaller part also in IP4, at 30 cm depth, we expect a former snow surface to be eroded by a strong wind or even storm event. This may also have caused the double peak

structure in isotope fingerprints by eroding the maximum as well as the total low in aerosol concentrations in summer 12/13. Enhanced wind pumping may also have played a major role on $\delta^{18}O$ alteration (TOWN et al., 2008). Density data confirm this theory as this can be assumed as reason for the decrease in density around 30 cm depth. With constant accumulation, density should steadily increase with depth (HERRON & LANGWAY, 1980). As snow drift events should cause high differences in snow density as no continuous densification takes place, jumps in density between 30 cm and 50 cm depth in average (s. black line, Fig. 22) as well as single snow liner (s. grey shaded background, Fig. 22) can be explained. Drift snow directly after settling also is characterized by low densities around 0.33 g/cm³ (BIRNBAUM et al., 2010) and may show different densification patterns. Comparing these findings with meteorological data (Fig. 32) gives unfortunately no correlation with remarkably high wind speeds during the concerning time interval. Explanation for that might be short term squalls that are not detected by the automatic weather station.
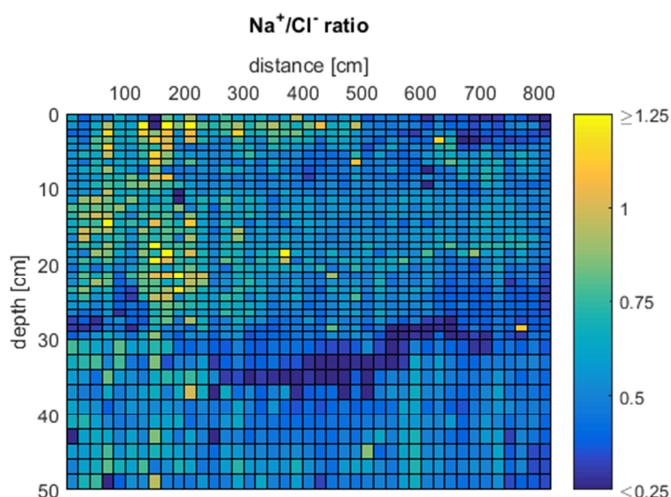
Fig. 26: Also in Na$^+$/Cl$^-$ ratio the erosion horizon between 30 and 36 cm depth can be visually detected. Again, on the horizontal axis distance is depicted, on the vertical axis depth. Color scale represents the dimensionless ratio. Standard value is roughly 0.65. Area with dark blue colors shows extreme sodium depletion. As low Na$^+$ concentration in relation to Cl$^-$ can be signal for stratospheric input (LEGRAND & DELMAS, 1988), we estimate strong katabatic winds to have caused erosion followed up by some millimeters or even centimeters of accumulation. The accumulation event in mid of January interestingly shows a similar fingerprint. High Na$^+$/Cl$^-$ ratios in left part of the figure can be addressed to contamination. Despite that, Na$^+$/Cl$^-$ ratio can also be an indicator for excess Cl$^-$ in form of hydrochloric acid (WELLER, 2015, pers. commun.). No spatial equally distributed loss of chloride can be seen, the ratio even stays pretty constant throughout the profile. Like WELLER et al. (2004), we cannot report a significant loss of Cl$^-$ throughout the profile.
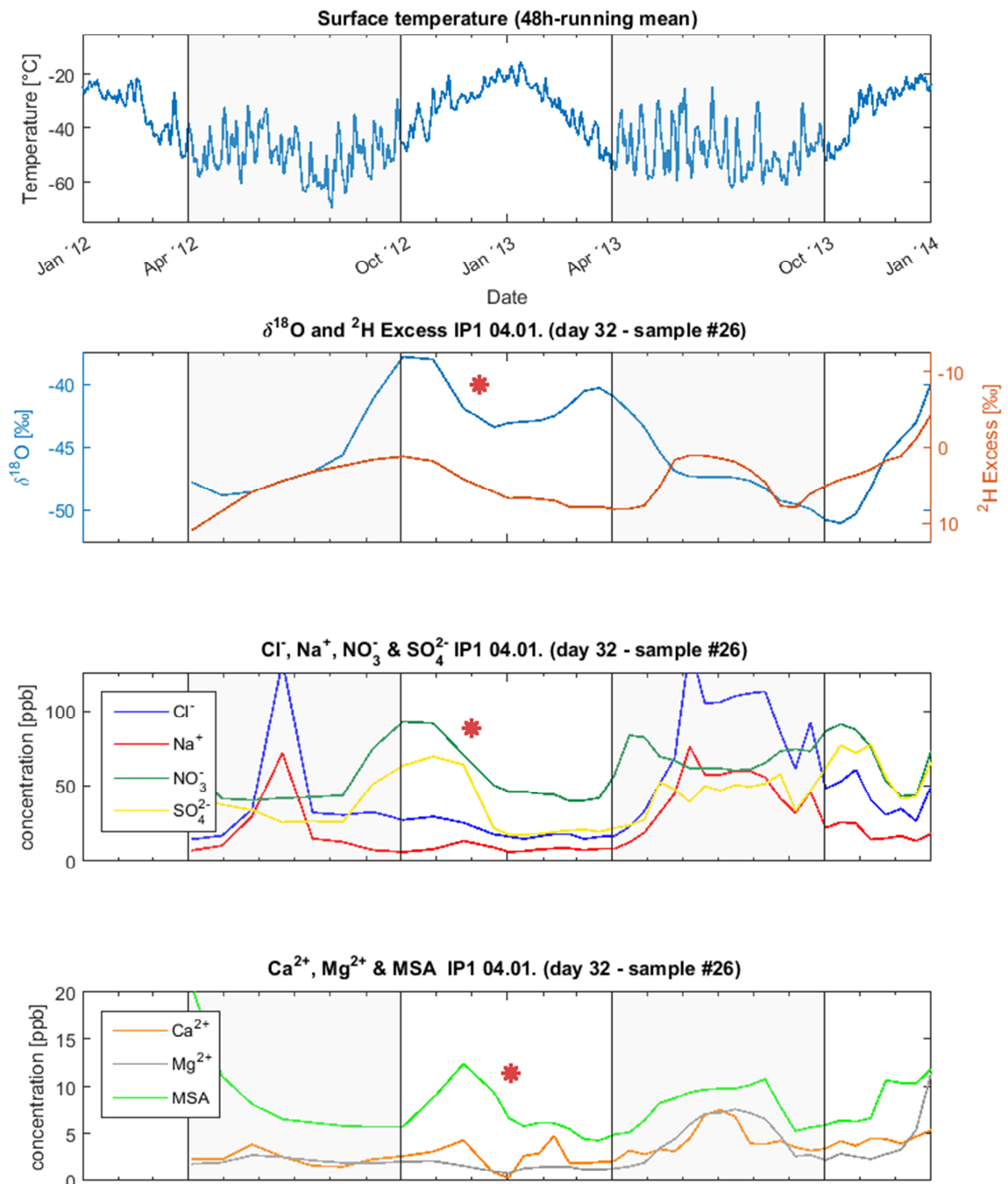
Fig. 27: This plot shows a linear fit of depth and time with the isotope and aerosol record of one snow liner from the 4th of January 2014 (sample #26) at IP1. In contrast to averaged profile in Fig. 24, we note high fluctuations and peaks in all species. Although the temporal fit is poor due to constant annual accumulation rate, peak patterns seem to match better than for spatially averaged plot. Remarkable feature in this plot is the simultaneous and rapid decrease on nitrate, sulfate, MSA as well as $\delta^{18}O$. For some time (or depth, respectively) values remain on the same low level. High Na^+ and Cl^- peaks at the bottom of the profile can be neglected due to contamination (comp. Fig. 16). Red stars indicate the possible erosion event.

Further postdepositional processes are difficult to derive from this dataset. Nevertheless, in $\delta^{18}O$ strong smoothing is visible in strata just below the accumulation event, as mentioned some paragraphs

before, at the right end of the horizontal profile (s. Fig. 20). According to the horizontal axis in Fig. 20, in the middle of the profile in depth between 3 cm and 10 cm centimeters very low values up to 55‰ dominate. Otherwise, at the right side, values in the same depth interval increase by 5‰ below the fresh deposited snow at the surface. According to a diffusion length of ^{18}O in snow and firn of up to 8 cm (VAN DER WEL et al., 2015), the smoothing in $\delta^{18}O$ can be explained by this. It is not clear, whether the diffusion within the snow column can be that fast (TOWN et al., 2008). On the other hand, sublimation of snow samples at the snow surface take place in even shorter time intervals (STEEN-LARSEN et al., 2014).

Additionally high diffusion is stated for chloride, MSA and nitrate (WELLER et al., 2004). Referring to the average concentrations and standard deviations, nitrate shows one of the highest mean values in the dataset and comparably low standard deviation. Relative standard deviation of nitrate ranges from 27-37% whereas chloride shows 53-76% and MSA even 35-105%. This is logical as peaks of Cl^- and MSA are relatively higher than NO_3^- peaks. But another explanation might be high diffusivity hat also explains high nitrate in summer and winter layers. High diffusivity of MSA cannot be confirmed in the horizontal profile of IP1, but is very likely considering the run in Fig. 27. Cl^- excess, which was also not significantly observed in WELLER et al. (2004), does not significantly occur (comp. Fig. 26).

Correlation and coherence of different species

Seasonal snow layers are nicely visible in color intensity plots posted in the Results. Some structural patterns like lenses and horizons repeated in several aerosols as well as isotopic fingerprints. On first sight, patterns seemed that regular that a linear correlation between some species is possible. For that reason, a linear correlation factor was calculated for most of the analyzed species. Calculations were applied like stated in Material & methods.

Like previously expected, sodium and chlorine match with high correlation factor as both originate from sea salt and have the same depositional patterns (LEGRAND & MAYEWSKI, 1997). Nevertheless, a slightly higher factor was expected (s. Fig. 34). A bit lower but still appropriate values show sodium and magnesium (not shown).
Of course $\delta^{18}O$ and δ^2H show very good results as can be already seen in matches on the GMWL in Fig. 25.

Unfortunately no other species has shown significant linear correlation with each other (s. Fig. 28 and Fig. 29). Different from proposed in the hypothesis, we were not able to state a new theory.
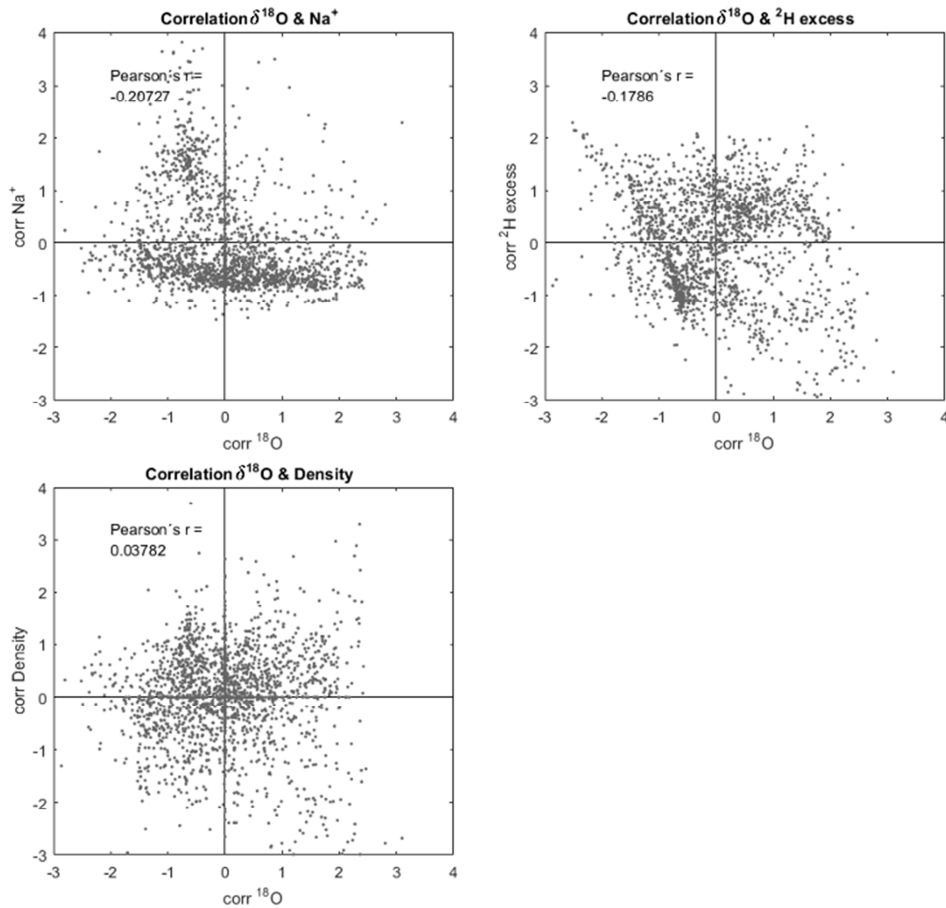
Fig. 28: No high linear correlation exists for $\delta^{18}O$ with Na^+ concentration, ^2H-excess or density. We tested linear correlation according to the formula in the Material & methods. Highest correlation factor still show $\delta^{18}O$ with Na^+.

Nevertheless, some species seem still to show some coherence which is not linear. For further studies therefore a non-linear correlation for several species is suggested.

Linear coherence between calcium (s. Fig. 29) or any other species and density did not show any significance, which is mainly a problem of density data. For a linear correlation a steady increase and annual layers should be visible. Then, in deeper strata, linear correlation between other species than calcium (FREITAG et al., 2013a) might be possible.
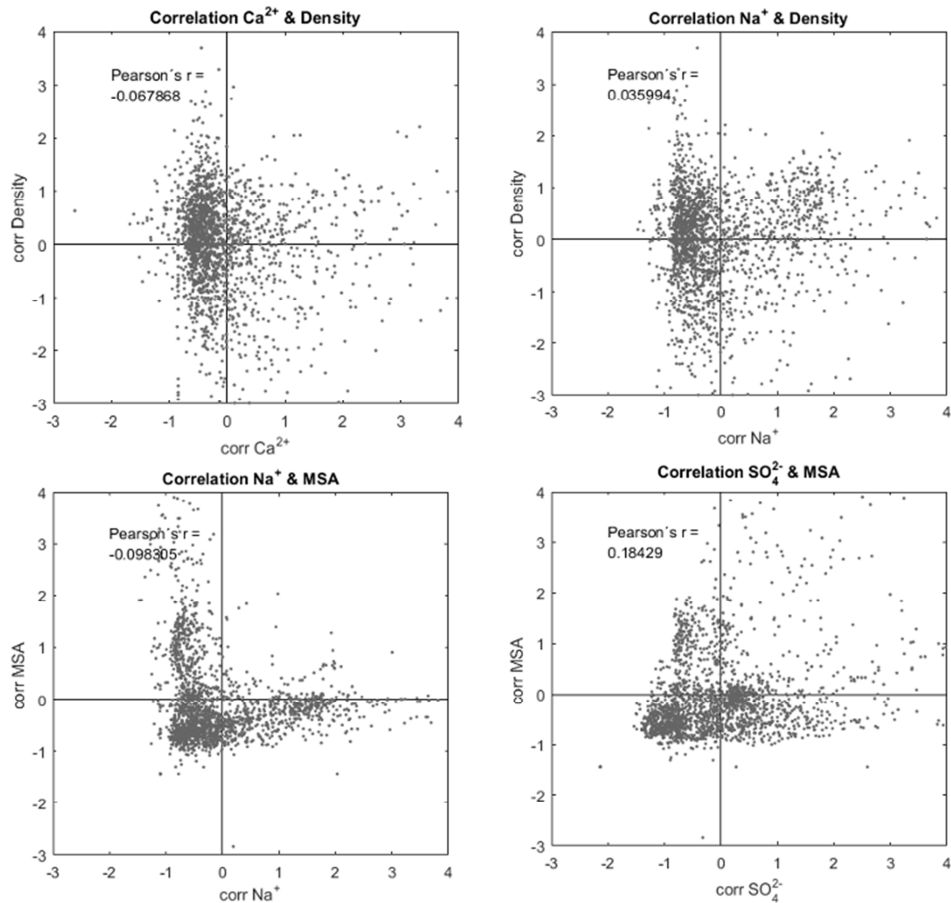
Fig. 29: Correlation plots for calcium with density (top left) as well as sodium and density (top right) show no significant relation which is based on the density data. SO_4^{2-} and MSA (bottom left) do also show no high linear coherence but can be investigated in terms of non-linear correlation. Same accounts for Na^+ and MSA (bottom left).

Spatial and temporal variability

Snow liners were also taken with the intention to analyze and decouple temporal and spatial variability of aerosols and isotopes at a distinct location and area. On the one hand, this investigation helps to take one step further in understanding the origin of seasonal signals, but on the other hand to classify the reliability of single samples or cores (MÜNCH et al., 2015).

Unfortunately, the samples of the horizontal IP1 profile are spatially dependent on each other as samples were taken systematically in a row and not randomly. This makes an approach very difficult to decouple both variability types.

The presented approach is to compare the standard deviation of a spatially independent profile and a temporally independent profile of Na^+ and $\delta^{18}O$. For the spatially independent profile we took the calculations as used before for the temporal fit (Fig. 24). For the temporally independent profile, we used five snow liners along profile IP1 with maximum temporal spacing. For this purpose, we used snow liners of sampling day 1, day 12, day 21, day 31 and day 40. Data basis for both average values can be found in Table 4 and Table 5 (spatially independent average) as well as Table 6 and
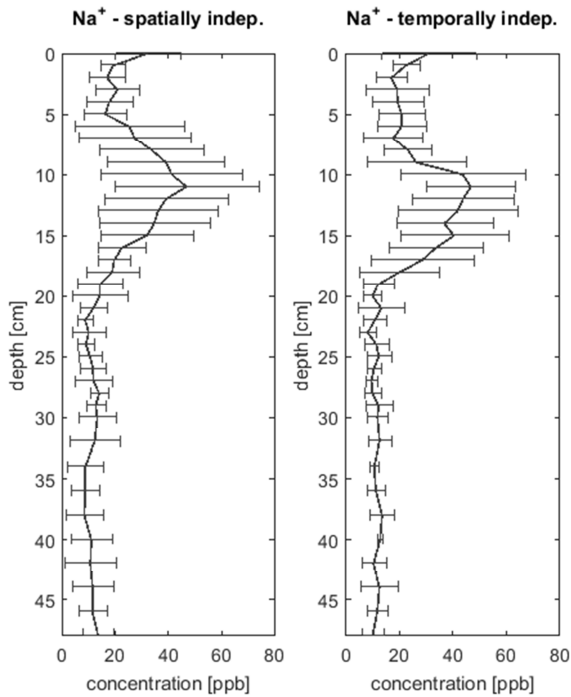
Fig. 30: The spatial and temporal variability of Na⁺ is shown in a plot of concentration on the horizontal axis and depth on the vertical axis. For data basis, see the text above. Error bars indicate standard deviation and symbolize the spatial (left panel) and temporal (right panel) variability.

From variability plots of Fig. 30 and Fig. 31 no extreme differences can be observed. Error bars for spatially independent profiles show more constant error bars than temporally independent profiles. The latter, on the other hand, seem to have higher standard deviation along peak structures. With these two plots we see, how difficult it is to decouple a spatial from a temporal signal on a small scale with low vertical resolution, in this case accumulation rate (MÜNCH et al., 2015). For reasonable analysis concerning variability for ice cores we therefore suggest, to take a high amount of spatially independent samples and repeat the procedure in certain time intervals.

Table 7 (temporally independent average). Nevertheless, both calculations are not perfect and can be influenced by temporal or spatial signals, respectively.

For analyzing spatial and temporal variability, it established to compare the standard deviation of whole site mean (representing spatial variance) with standard deviation of each sampling point, in this case IP1 to IP4 (representing temporal variance) (CAIAZZO et al., 2016). Doing so shows, that temporal variability exceeds spatial one by far. For this specific setup, the calculation is not optimal as for average values a different amount of samples is used and IP1 is smoothed pretty much. Additionally, spatial variance along IP1 is higher than IP2, IP3 and IP4 (s. Table 2 and Table 3).

Fig. 31: For δ¹⁸O the same analysis was done as for Na⁺ in Fig. 30. Error bars in this figure have much more similar size and state, how difficult it is do decouple the spatial and temporal variability on a small scale.
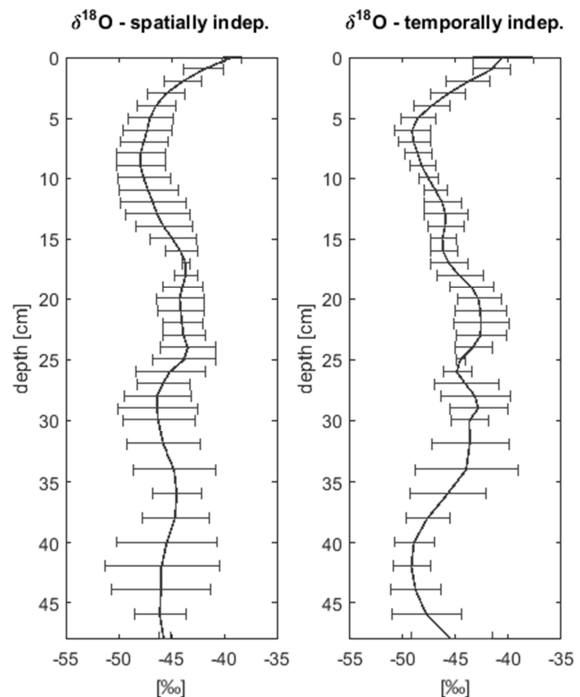
SUMMARY

Conclusion

This master thesis has confirmed a strong coherence between accumulation and the temporal variation of $\delta^{18}O$ signals as well as major aerosol species. With an accumulation-dependent transformation of depth to time and a spatially independent average of several snow liners, $\delta^{18}O$ and ^2H-excess curves were adjusted and with help of conservative trace elements like Na^+ and Cl^-, seasonal signals were confirmed. Assuming a minimum accumulation in austral summer months December and January, we conclude that there actually is no real deposition of a summer isotopic signal. $\delta^{18}O$ deposition is strongly dependent on short term climatic patterns like high-precipitation events. Summer signals therefore can be a smoothing of spring and autumn precipitation by postdepositional alteration like sublimation or diffusion as well as forced by wind pumping. For further specification of the dependence on accumulation, large focus should be put on obtaining continuous annual records of precipitation and accumulation in Antarctica.

In deuterium excess curves sublimation and evaporation processes at the surface were confirmed. Especially in summer months, when snow has a large residence time, this alteration affects δ^2H as well as $\delta^{18}O$.

We further conclude all records, isotopes and trace elements, to be affected by short term temporal and spatial events, which are important for the stratigraphy as well as absolute concentrations. Along a strong concentration gradient in isotope signals as well as ion concentrations, an erosion horizon could be identified. Such snow drift, what we address as the erosion source, as well as high precipitation events may have a larger influence on the continuous ice core records than previously known.

Interestingly, on a large scale and without temporal fitting, signals of trace elements and isotopes seem to mirror the climatic conditions pretty well. The approach of high resolution sampling makes the differentiation of the signals more complicated. Whether these findings have impact on the interpretation of ice cores is beyond the author's estimation. But as suggested in recent publications, findings of this thesis state in ice core records to be more isotopic noise than previously expected. In the aerosol record we used sea salt aerosols as reliable tracer for winter months even in a medium accumulation site. Unfortunately, sulfate, MSA as well as nitrate tend to strong diffusion as can be seen in smooth plots and high mean concentrations throughout all seasons.

Unfortunately, we were not able to derive high linear correlation between several ions or isotopic values, but further investigations on non-linear correlation is strongly recommended, as in horizontal profiles clearly dependence between aerosols and isotopes is visible.

Concluding the thesis, temporal and spatial variability of the samples was analysed. However, with this setup in the field significant statements are difficult as samples are somehow spatially dependent on each other. Nevertheless, we have shown, that with this setup the spatial variability is too high to

resolve temporal-dependent changes of proxies in snow and firn, which should be in the focus of further research in the future.

Outlook

In the recent field season (austral summer 2015/16), a new setup for snow liner sampling was tested. To obtain higher precision for proxies as well as for dating, continuous flow analysis is suggested as analyzing method for the samples to obtain data in higher resolution. Especially the record in the summer months and during periods of high temperature fluctuations may reveal more insights on the sensitivity.

To improve the sampling setup, we suggest taking snow liners along a grid with distinct spacing in every spatial direction within one or two day. This pattern should be repeated in intervals of one week or even more. Of course, the snow liners of the next sampling pattern should be taken as close to the first location as possible. With that setup, temporal and spatial variability might be easier to separate.

Finally, we suggest infrared cameras or other technical support for annual accumulation observation. Despite a single number of accumulation it would also be also good to know the type of accumulation, how it formed and as well as the temporal frame.

REFERENCES

AYERS, G. P., IVEY, J. P. & GILLETT, R. W. (1991): Coherence between seasonal cycles of dimethyl sulphide, methanesulphonate and sulphate in marine air. Nature 349, 404-406.

BARBANTE, C., COZZI, G., CAPODAGLIO, G., VAN DE VELDE, K., FERRARI, C., VEYSSEYRE, A., BOUTRON, C. F., SCARPONI, G. & CESCON, P. (1999): Determination of Rh, Pd, and Pt in polar and alpine snow and ice by double focusing ICPMS with microconcentric nebulization. Analytical Chemistry 71, 4125-4133.

BENDEL, V., UELTZHÖFFER, K. J., FREITAG, J., KIPFSTUHL, S., KUHS, W. F., GARBE, C. S. & FARIA, S. H. (2013): High-resolution variations in size, number and arrangement of air bubbles in the EPICA DML (Antarctica) ice core. J Glaciol 59, 972-980.

BERGIN, M. H., DAVIDSON, C. I., KUHNS, H. D., JAFFREZO, J. L., DIBB, J. E., HILLAMO, R. & MAKELA, T. (1995): The contributions of wet, fog and dry deposition to the summer SO42- flux at Summit, Greenland.

BIGLER, M., SVENSSON, A., KETTNER, E., VALLELONGA, P., NIELSEN, M. E. & STEFFENSEN, J. P. (2011): Optimization of High-Resolution Continuous Flow Analysis for Transient Climate Signals in Ice Cores. Environmental Science & Technology 45, 4483-4489.

BIRNBAUM, G., FREITAG, J., BRAUNER, R., KONIG-LANGLO, G., SCHULZ, E., KIPFSTUHL, S., OERTER, H., REIJMER, C. H., SCHLOSSER, E., FARIA, S. H., RIES, H., LOOSE, B., HERBER, A., DUDA, M. G., POWERS, J. G., MANNING, K. W. & VAN DEN BROEKE, M. R. (2010): Strong-wind events and their influence on the formation of snow dunes: observations from Kohnen station, Dronning Maud Land, Antarctica. J Glaciol 56, 891-902.

BORYS, R. D., DEL VECCHIO, D., JAFFREZO, J. L., DIBB, J. & MITCHELL, D. (1992): Field observations, measurements and preliminary results from a study of wet deposition processes influencing snow and ice chemistry at Summit, Greenland, in: Schwartz, S. E. & Slinn, W. G. N. (Eds.), Precipitation Scavenging and Atmosphere-Surface Exchange. Hemisphere Publishing Corp., pp. 1693-1702.

BORYS, R. D., HINDMAN, E. E. & DEMOTT, P. J. (1988): The Chemical Fractionation of Atmospheric Aerosol as a Result of Snow Crystal-Formation and Growth. Journal of Atmospheric Chemistry 7, 213-239.

BOTTENHEIM, J. W. & BARRIE, L. A. (1996): Chemical Reactions in the Polar Troposhere Relevant to C, S, and N Compounds, in: Wolff, E. W. & Bales, R. C. (Eds.), Chemical Exchange Between the Atmosphere and Polar Snow. Springer Berlin Heidelberg, Berlin, Heidelberg, pp. 201-224.

CAIAZZO, L., BECAGLI, S., FROSINI, D., GIARDI, F., SEVERI, M., TRAVERSI, R. & UDISTI, R. (2016): Spatial and temporal variability of snow chemical composition and accumulation rate at Talos Dome site (East Antarctica). Science of the Total Environment 550, 418-430.

CIAIS, P., WHITE, J. W. C., JOUZEL, J. & PETIT, J. R. (1995): THE ORIGIN OF PRESENT-DAY ANTARCTIC PRECIPITATION FROM SURFACE SNOW DEUTERIUM EXCESS DATA. J Geophys Res-Atmos 100, 18917-18927.

COLBECK, S. C. (1993): THE VAPOR DIFFUSION-COEFFICIENT FOR SNOW. Water Resources Research 29, 109-115.

CRAIG, H. (1961a): Isotopic Variations in Meteoric Waters. Science 133, 1702-1703.

CRAIG, H. (1961b): Standard for Reporting Concentrations of Deuterium and Oxygen-18 in Natural Waters. Science 133, 1833-1834.

CUFFEY, K. M. & PATERSON, W. S. B. (2010): The Physics of Glaciers, 4th ed. Academic press.

DANSGAARD, W. (1964): Stable Isotopes in Precipitation. Tellus 16, 436-468.

DAVIDSON, C. I., BERGIN, M. H. & KUHNS, H. D. (1996): The Deposition Of Particles and Gases to Ice Sheets, in: Wolff, E. W. & Bales, R. C. (Eds.), Chemical Exchange Between the Atmosphere and Polar Snow. Springer Berlin Heidelberg, Berlin, Heidelberg, pp. 275-306.

DIONEX (2015): Dionex - ICS-2100 Integrated Reagent-Free IC System. http://www.dionex.com/en-us/webdocs/73382-Man-IC-ICS2100-Operators-Oct2012-DOC065291-03.pdf (Access: 26.03.2016)

DRÜCKER, C., WILHELMS, F., OERTER, H., FRENZEL, A., GERNANDT, H. & MILLER, H. (2002): Design, transport, construction, and operation of the summer base Kohnen for ice-core drilling in Dronning Maud Land, Antarctica. Ice drilling technology 2000 : Proceedings of the fifth International Workshop on Ice Drilling Technology, 30 October-1 November 2000, Nagaoka University of Technology, Nagaoka, 302-312.

EBINUMA, T. & MAENO, N. (1987): Particle Rearrangement and Dislocation Creep in a Snow-Densification Process. Journal De Physique 48, 263-269.

EPICA COMMUNITY MEMBERS (2004): Eight glacial cycles from an Antarctic ice core. Nature 429, 623-628.

EPICA COMMUNITY MEMBERS (2006): One-to-one coupling of glacial climate variability in Greenland and Antarctica. Nature 444, 195-198.

ETHERIDGE, D. M., STEELE, L. P., LANGENFELDS, R. L., FRANCEY, R. J., BARNOLA, J. M. & MORGAN, V. I. (1996): Natural and anthropogenic changes in atmospheric CO_2 over the last 1000 years from air in Antarctic ice and firn. J Geophys Res-Atmos 101, 4115-4128.

FERNANDOY, F., MEYER, H. & TONELLI, M. (2012): Stable water isotopes of precipitation and firn cores from the northern Antarctic Peninsula region as a proxy for climate reconstruction. The Cryosphere 6, 313-330.

FISCHER, H. (unpublished): Glaziologie, in: Bremen, U. o. (Ed.).

FISCHER, H., SEVERINGHAUS, J., BROOK, E., WOLFF, E., ALBERT, M., ALEMANY, O., ARTHERN, R., BENTLEY, C., BLANKENSHIP, D., CHAPPELLAZ, J., CREYTS, T., DAHL-JENSEN, D., DINN, M., FREZZOTTI, M., FUJITA, S., GALLEE, H., HINDMARSH, R., HUDSPETH, D., JUGIE, G., KAWAMURA, K., LIPENKOV, V., MILLER, H., MULVANEY, R., PARRENIN, F., PATTYN, F., RITZ, C., SCHWANDER, J., STEINHAGE, D., VAN OMMEN, T. & WILHELMS, F. (2013): Where to find 1.5 million yr old ice for the IPICS "Oldest-Ice" ice core. Climate of the Past 9, 2489-2505.

FISHER, D. A., KOERNER, R. M., PATERSON, W. S. B., DANSGAARD, W., GUNDESTRUP, N. & REEH, N. (1983): Effect of wind scouring on climatic records from ice-core oxygen-isotope profiles. Nature 301, 205-209.

FISHER, D. A., REEH, N. & CLAUSEN, H. B. (1985): Stratigraphic noise in time series derived from ice cores. Annals of Glaciology 7, 76-83.

FREITAG, J., KIPFSTUHL, S. & LAEPPLE, T. (2013a): Core-scale radioscopic imaging: a new method reveals density–calcium link in Antarctic firn. J Glaciol 59, 1009-1014.

FREITAG, J., KIPFSTUHL, S., LAEPPLE, T. & WILHELMS, F. (2013b): Impurity-controlled densification: a new model for stratified polar firn. J Glaciol 59, 1163-1169.

GAT, J. R. (1996): Oxygen and hydrogen isotopes in the hydrologic cycle. Annu Rev Earth Pl Sc 24, 225-262.

GKINIS, V., POPP, T. J., JOHNSEN, S. J. & BLUNIER, T. (2010): A continuous stream flash evaporator for the calibration of an IR cavity ring-down spectrometer for the isotopic analysis of water. Isotopes Environ Health Stud 46, 463-475.

HERRON, M. M. & LANGWAY, C. C. (1980): Firn densification - an empirical-model. J Glaciol 25, 373-385.

HÖRHOLD, M. W., LAEPPLE, T., FREITAG, J., BIGLER, M., FISCHER, H. & KIPFSTUHL, S. (2012): On the impact of impurities on the densification of polar firn. Earth and Planetary Science Letters 325-326, 93-99.

HOSHINA, Y., FUJITA, K., NAKAZAWA, F., IIZUKA, Y., MIYAKE, T., HIRABAYASHI, M., KURAMOTO, T., FUJITA, S. & MOTOYAMA, H. (2014): Effect of accumulation rate on water stable isotopes of near-surface snow in inland Antarctica. J Geophys Res-Atmos 119, 274-283.

JASECHKO, S., SHARP, Z. D., GIBSON, J. J., BIRKS, S. J., YI, Y. & FAWCETT, P. J. (2013): Terrestrial water fluxes dominated by transpiration. Nature 496, 347-350.

JOHNSEN, S., CLAUSEN, H. B., CUFFEY, K. M., HOFFMANN, G., SCHWANDER, J. & CREYTS, T. (2000): Diffusion of stable isotopes in polar firn and ice: the isotope effect in firn diffusion, Physics of ice core records. Hokkaido University, Sapporo, pp. 121-140.

JOHNSEN, S. J., DAHL-JENSEN, D., GUNDESTRUP, N., STEFFENSEN, J. P., CLAUSEN, H. B., MILLER, H., MASSON-DELMOTTE, V., SVEINBJÖRNSDOTTIR, A. E. & WHITE, J. (2001): Oxygen isotope and palaeotemperature records from six Greenland ice-core stations: Camp Century, Dye-3, GRIP, GISP2, Renland and NorthGRIP. Journal of Quaternary Science 16, 299-307.

JOUZEL, J., MASSON-DELMOTTE, V., CATTANI, O., DREYFUS, G., FALOURD, S., HOFFMANN, G., MINSTER, B., NOUET, J., BARNOLA, J. M., CHAPPELLAZ, J., FISCHER, H., GALLET, J. C., JOHNSEN, S., LEUENBERGER, M., LOULERGUE, L., LUETHI, D., OERTER, H., PARRENIN, F., RAISBECK, G., RAYNAUD, D., SCHILT, A., SCHWANDER, J., SELMO, E., SOUCHEZ, R., SPAHNI, R., STAUFFER, B., STEFFENSEN, J. P., STENNI, B., STOCKER, T. F., TISON, J. L., WERNER, M. & WOLFF, E. W. (2007): Orbital and millennial Antarctic climate variability over the past 800,000 years. Science 317, 793-796.

JOUZEL, J. & MERLIVAT, L. (1984): Deuterium and oxygen 18 in precipitation: Modeling of the isotopic effects during snow formation. Journal of Geophysical Research 89, 11749.

KARLOF, L., ISAKSSON, E., WINTHER, J. G., GUNDESTRUP, N., MEIJER, H. A. J., MULVANEY, R., POURCHET, M., HOFSTEDE, C., LAPPEGARD, G., PETTERSSON, R., VAN DEN BROEKE, M. & VAN DE WAL, R. S. W. (2005): Accumulation variability over a small area in east Dronning Maud Land, Antarctica, as determined from shallow firn cores and snow pits: some implications for ice-core records. J Glaciol 51, 343-352.

KARLOF, L., WINEBRENNER, D. P. & PERCIVAL, D. B. (2006): How representative is a time series derived from a firn core? A study at a low-accumulation site on the Antarctic plateau. J Geophys Res-Earth 111, 11.

KAUFMANN, P. R., FEDERER, U., HUTTERLI, M. A., BIGLER, M., SCHUPBACH, S., RUTH, U., SCHMITT, J. & STOCKER, T. F. (2008): An Improved Continuous Flow Analysis System for High-Resolution Field Measurements on Ice Cores. Environmental Science & Technology 42, 8044-8050.

LAMBERT, F., DELMONTE, B., PETIT, J. R., BIGLER, M., KAUFMANN, P. R., HUTTERLI, M. A., STOCKER, T. F., RUTH, U., STEFFENSEN, J. P. & MAGGI, V. (2008): Dust-climate couplings over the past 800,000 years from the EPICA Dome C ice core. Nature 452, 616-619.

LANGWAY, C. C. (1970): Stratigraphic Analysis of a Deep Ice Core from Greenland. Geological Society of America Special Papers 125, 180.

LEGRAND, M., DUCROZ, F., WAGENBACH, D., MULVANEY, R. & HALL, J. (1998): Ammonium in coastal Antarctic aerosol and snow: Role of polar ocean and penguin emissions. J Geophys Res-Atmos 103, 11043-11056.

LEGRAND, M. & MAYEWSKI, P. (1997): Glaciochemistry of polar ice cores: A review. Rev Geophys 35, 219.

LEGRAND, M. R. & DELMAS, R. J. (1988): Formation of HCl in the Antarctic Atmosphere. J Geophys Res-Atmos 93, 7153-7168.

LUTHI, D., LE FLOCH, M., BEREITER, B., BLUNIER, T., BARNOLA, J. M., SIEGENTHALER, U., RAYNAUD, D., JOUZEL, J., FISCHER, H., KAWAMURA, K. & STOCKER, T. F. (2008): High-resolution carbon dioxide concentration record 650,000-800,000 years before present. Nature 453, 379-382.

MONAHAN, E. C., SPIEL, D. E. & DAVIDSON, K. L. (1986): A Model of Marine Aerosol Generation Via Whitecaps and Wave Disruption, in: Monahan, E. C. & Niocaill, G. M. (Eds.), Oceanic Whitecaps: And Their Role in Air-Sea Exchange Processes. Springer Netherlands, Dordrecht, pp. 167-174.

MÜLLER, W., SHELLEY, J. M. G. & RASMUSSEN, S. O. (2011): Direct chemical analysis of frozen ice cores by UV-laser ablation ICPMS. Journal of Analytical Atomic Spectrometry 26, 2391.

MULVANEY, R., WAGENBACH, D. & WOLFF, E. W. (1998): Postdepositional change in snowpack nitrate from observation of year-round near-surface snow in coastal Antarctica. J Geophys Res-Atmos 103, 11021-11031.

MÜNCH, T., KIPFSTUHL, S., FREITAG, J., MEYER, H. & LAEPPLE, T. (2015): Regional climate signal vs. local noise: a two-dimensional view of water isotopes in Antarctic firn at Kohnen station, Dronning Maud Land. Climate of the Past Discussions 11, 5605-5649.

NISHIMURA, H., MAENO, N. & SATOW, K. (1983): Initial stage of densification of snow in Mizuho Plateau, Antarctica. Memoirs of National Institute of Polar Research. Special issue 29, 149-158.

NOONE, D., TURNER, J. & MULVANEY, R. (1999): Atmospheric signals and characteristics of accumulation in Dronning Maud Land, Antarctica. J Geophys Res-Atmos 104, 19191-19211.

OERTER, H., DRÜCKER, C., KIPFSTUHL, S. & WILHELMS, F. (2009): Kohnen station - the drilling camp for the EPICA deep ice core in Dronning Maud Land. Polarforschung 78, 1-23.

OERTER, H., GRAF, W., MEYER, H. & WILHELMS, F. (2004): The EPICA ice core from Dronning Maud Land: first results from stable-isotope measurements. Ann Glaciol-Ser 39, 307-312.

OERTER, H., GRAF, W., WILHELMS, F., MINIKIN, A. & MILLER, H. (1999): Accumulation studies on Amundsenisen, Dronning Maud Land, Antarctica, by means of tritium, dielectric profiling and stable-isotope measurements: first results from the 1995-96 and 1996-97 field seasons, in: Jacka, T. H. (Ed.), Annals of Glaciology, Vol 29, 1999, pp. 1-9.

OERTER, H., WILHELMS, F., JUNG-ROTHENHAUSLER, F., GOKTAS, F., MILLER, H., GRAF, W. & SOMMER, S. (2000): Accumulation rates in Dronning Maud Land, Antarctica, as revealed by dielectric-profiling measurements of shallow firn cores, in: Hutter, K. (Ed.), Annals of Glaciology, Vol 30, 2000. Int Glaciological Soc, Cambridge, pp. 27-34.

PALMER, A. S., VAN OMMEN, T. D., CURRAN, M. A. J., MORGAN, V., SOUNEY, J. M. & MAYEWSKI, P. A. (2001): High-precision dating of volcanic events (A.D. 1301-1995) using ice cores from Law Dome, Antarctica. Journal of Geophysical Research: Atmospheres 106, 28089-28095.

PERSSON, A., LANGEN, P. L., DITLEVSEN, P. & VINTHER, B. M. (2011): The influence of precipitation weighting on interannual variability of stable water isotopes in Greenland. Journal of Geophysical Research 116.

PETIT, J. R., JOUZEL, J., RAYNAUD, D., BARKOV, N. I., BARNOLA, J. M., BASILE, I., BENDER, M., CHAPPELLAZ, J., DAVIS, M., DELAYGUE, G., DELMOTTE, M., KOTLYAKOV, V. M., LEGRAND, M., LIPENKOV, V. Y., LORIUS, C., PÉPIN, L., RITZ, C., SALTZMAN, E. & STIEVENARD, M. (1999): Climate and atmospheric history of the past 420,000 years from the Vostok ice core, Antarctica. Nature 399, 429-436.

PETIT, J. R., WHITE, J. W. C., YOUNG, N. W., JOUZEL, J. & KOROTKEVICH, Y. S. (1991): Deuterium excess in recent Antarctic snow. J Geophys Res-Atmos 96, 5113-5122.

PFAHL, S. & SODEMANN, H. (2014): What controls deuterium excess in global precipitation? Climate of the Past 10, 771-781.

PICARD, G., DOMINE, F., KRINNER, G., ARNAUD, L. & LEFEBVRE, E. (2012): Inhibition of the positive snow-albedo feedback by precipitation in interior Antarctica. Nature Clim. Change 2, 795-798.

PICARRO INC. (2016): Cavity Ring-Down Spectroscopy (CRDS). http://www.picarro.com/technology/cavity_ring_down_spectroscopy (Access: 16.03.2016)

PIEL, C. (2003): Variabilität physikalischer und chemischer Parameter des Aerosols in der antarktischen Troposphäre. University of Bremen, Bremen, p. 157.

POURCHET, M., MAGAND, O., FREZZOTTI, M., EKAYKIN, A. & WINTHER, J. G. (2003): Radionuclides deposition over Antarctica. Journal of Environmental Radioactivity 68, 137-158.

RANKIN, A. M., AULD, V. & WOLFF, E. W. (2000): Frost flowers as a source of fractionated sea salt aerosol in the polar regions. Geophysical Research Letters 27, 3469-3472.

RAYNAUD, D., JOUZEL, J., BARNOLA, J. M., CHAPPELLAZ, J., DELMAS, R. J. & LORIUS, C. (1993): The Ice Record of Greenhouse Gases. Science 259, 926-934.

REIJMER, H., VAN DEN BROEKE, R. & SCHEELE, M. P. (2002): Air parcel trajectories and snowfall related to five deep drilling locations in Antarctica based on the ERA-15 dataset. Journal of Climate 15, 1957-1968.

ROZANSKI, K., ARAGUÁS-ARAGUÁS, L. & GONFIANTINI, R. (1993): Isotopic patterns in modern global precipitation, in: Swart, P. K. (Ed.), Climate Change in Continental Isotopic Records, Washington, DC, pp. 1-36.

RUTH, U., BARNOLA, J. M., BEER, J., BIGLER, M., BLUNIER, T., CASTELLANO, E., FISCHER, H., FUNDEL, F., HUYBRECHTS, P., KAUFMANN, P., KIPFSTUHL, S., LAMBRECHT, A., MORGANTI, A., OERTER, H., PARRENIN, F., RYBAK, O., SEVERI, M., UDISTI, R., WILHELMS, F. & WOLFF, E. (2007): "EDML1": a chronology for the EPICA deep ice core from Dronning Maud Land, Antarctica, over the last 150 000 years. Climate of the Past 3, 475-484.

SAHRA (2005): Isotopes and Hydrology - Oxygen. http://web.sahra.arizona.edu/programs/isotopes/oxygen.html (Access: 24.03.2016)

SAVOIE, D. I., PROSPERO, J. M., LARSEN, R. J., HUANG, F., IZAGUIRRE, M. A., HUANG, T., SNOWDON, T. H., CUSTALS, L. & SANDERSON, C. G. (1993): Nitrogen and Sulfur Species in Antarctic Aerosols at Mawson, Palmer Station, and Marsh (King George Island). Journal of Atmospheric Chemistry 17, 95-122.

SCHWANDER, J., SOWERS, T., BARNOLA, J. M., BLUNIER, T., FUCHS, A. & MALAIZE, B. (1997): Age scale of the air in the summit ice: Implication for glacial-interglacial temperature change. J Geophys Res-Atmos 102, 19483-19493.

SCHWEDT, G. (1994): Chromatographische Trennmethoden: theoretische Grundlagen, Techniken und analytische Anwendungen, 3 ed. Thieme, Stuttgart; New York.

SHI, G., LI, Y., JIANG, S., AN, C., MA, H., SUN, B. & WANG, Y. (2012): Large-scale spatial variability of major ions in the atmospheric wet deposition along the China–Antarctica transect (31°N–69°S). Tellus B 64.

SIEGENTHALER, U., STOCKER, T. F., MONNIN, E., LUTHI, D., SCHWANDER, J., STAUFFER, B., RAYNAUD, D., BARNOLA, J. M., FISCHER, H., MASSON-DELMOTTE, V. & JOUZEL, J. (2005): Stable carbon cycle-climate relationship during the Late Pleistocene. Science 310, 1313-1317.

STAUFFER, B., WOLFF, E. & BARNES, P. (2004): The EPICA deep ice cores: first results and perspectives. Annals of Glaciology 39, 93-100.

STEEN-LARSEN, H. C., MASSON-DELMOTTE, V., HIRABAYASHI, M., WINKLER, R., SATOW, K., PRIÉ, F., BAYOU, N., BRUN, E., CUFFEY, K. M., DAHL-JENSEN, D., DUMONT, M., GUILLEVIC, M., KIPFSTUHL, S., LANDAIS, A., POPP, T., RISI, C., STEFFEN, K., STENNI, B. & SVEINBJÖRNSDOTTÍR, A. E. (2014): What controls the isotopic composition of Greenland surface snow? Climate of the Past 10, 377-392.

STEEN-LARSEN, H. C., MASSON-DELMOTTE, V., SJOLTE, J., JOHNSEN, S. J., VINTHER, B. M., BRÉON, F. M., CLAUSEN, H. B., DAHL-JENSEN, D., FALOURD, S., FETTWEIS, X., GALLÉE, H., JOUZEL, J., KAGEYAMA, M., LERCHE, H., MINSTER, B., PICARD, G., PUNGE, H. J., RISI, C., SALAS, D., SCHWANDER, J., STEFFEN, K., SVEINBJÖRNSDÓTTIR, A. E., SVENSSON, A. & WHITE, J. (2011): Understanding the climatic signal in the water stable isotope records from the NEEM shallow firn/ice cores in northwest Greenland. Journal of Geophysical Research 116.

STEINHAGE, D. (2001): Beiträge aus geophysikalischen Messungen in Dronning Maud Land, Antarktis, zur Auffindung eines optimalen Bohrpunktes für eine Eiskerntiefbohrung. Universität Bremen, p. 91.

TAYLOR, K. C., ALLEY, R. B., MEESE, D. A., SPENCER, M. K., BROOK, E. J., DUNBAR, N. W., FINKEL, R. C., GOW, A. J., KURBATOV, A. V., LAMOREY, G. W., MAYEWSKI, P. A., MEYERSON, E. A., NISHIIZUMI, K. & ZIELINSKI, G. A. (2004): Dating the Siple Dome (Antarctica) ice core by manual and computer interpretation of annual layering. J Glaciol 50, 453-461.

TOWN, M. S., WARREN, S. G., WALDEN, V. P. & WADDINGTON, E. D. (2008): Effect of atmospheric water vapor on modification of stable isotopes in near-surface snow on ice sheets. Journal of Geophysical Research 113.

TURNER, J., LACHLANCOPE, T. A., THOMAS, J. P. & COLWELL, S. R. (1995): The Synoptic Origins Of Precipitation Over The Antarctic Peninsula. Antarctic Science 7, 327-337.

UEMURA, R., MATSUI, Y., YOSHIMURA, K., MOTOYAMA, H. & YOSHIDA, N. (2008): Evidence of deuterium excess in water vapor as an indicator of ocean surface conditions. Journal of Geophysical Research 113.

VAN DER WEL, G., FISCHER, H., OERTER, H., MEYER, H. & MEIJER, H. A. J. (2015): Estimation and calibration of the water isotope differential diffusion length in ice core records. Cryosphere 9, 1601-1616.

VAN DER WEL, L. G. (2012): Analyses of water isotope diffusion in firn: Contributions to a better palaeclimatic interpretation of ice cores. University of Groningen, Groningen, p. 146.

WAGENBACH, D. (1996): Coastal Antarctica: Atmospheric Chemical Composition and Atmospheric Transport, in: Wolff, E. W. & Bales, R. C. (Eds.), Chemical Exchange Between the Atmosphere and Polar Snow. Springer Berlin Heidelberg, Berlin, Heidelberg, pp. 173-199.

WAGENBACH, D., DUCROZ, F., MULVANEY, R., KECK, L., MINIKIN, A., LEGRAND, M., HALL, J. S. & WOLFF, E. W. (1998a): Sea-salt aerosol in coastal Antarctic regions. J Geophys Res-Atmos 103, 10961-10974.

WAGENBACH, D., LEGRAND, M., FISCHER, H., PICHLMAYER, F. & WOLFF, E. W. (1998b): Atmospheric near-surface nitrate at coastal Antarctic sites. J Geophys Res-Atmos 103, 11007-11020.

WEIKUSAT, I., KIPFSTUHL, S., FARIA, S. H., AZUMA, N. & MIYAMOTO, A. (2009): Subgrain boundaries and related microstructural features in EDML (Antarctica) deep ice core. J Glaciol 55, 461-472.

WEISS, J., VIDOT, J., GAY, M., ARNAUD, L., DUVAL, P. & PETIT, J. R. (2002): Dome Concordia ice microstructure: impurities effect on grain growth, in: Wolff, E. W. (Ed.), Annals of Glaciology, Vol 35. Int Glaciological Soc, Cambridge, pp. 552-558.

WELKER, C., MARTIUS, O., FROIDEVAUX, P., REIJMER, C. H. & FISCHER, H. (2014): A climatological analysis of high-precipitation events in Dronning Maud Land, Antarctica, and associated large-scale atmospheric conditions. J Geophys Res-Atmos 119, 11932-11954.

WELLER, R., TRAUFETTER, F., FISCHER, H., OERTER, H., PIEL, C. & MILLER, H. (2004): Postdepositional losses of methane sulfonate, nitrate, and chloride at the European Project for Ice Coring in Antarctica deep-drilling site in Dronning Maud Land, Antarctica. J Geophys Res-Atmos 109.

WELLER, R. & WAGENBACH, D. (2007): Year-round chemical aerosol records in continental Antarctica obtained by automatic samplings. Tellus Series B-Chemical and Physical Meteorology 59, 755-765.

WESSEL, P. & SMITH, W. H. F. (1991): Free Software Helps Map and Display Data. EOS Transactions, American Geophysical Union 72, 445-446.

WHITLOW, S., MAYEWSKI, P. A. & DIBB, J. E. (1992): A Comparison of Major Chemical-Species Seasonal Concentration and Accumulation at the South-Pole and Summit, Greenland. Atmos Environ a-Gen 26, 2045-2054.

WILHELMS, F., MILLER, H., GERASIMOFF, M. D., DRÜCKER, C., FRENZEL, A., FRITZSCHE, D., GROBE, H., HANSEN, S. B., HILMARSSON, S. Æ., HOFFMANN, G., HÖRNBY, K., JAESCHKE, A., JAKOBSDÓTTIR, S. S., JUCKSCHAT, P., KARSTEN, A., KARSTEN, L., KAUFMANN, P. R., KARLIN, T., KOHLBERG, E., KLEFFEL, G., LAMBRECHT, A., LAMBRECHT, A., LAWER, G., SCHÄRMELI, I., SCHMITT, J., SHELDON, S. G., TAKATA, M., TRENKE, M., TWARLOH, B., VALERO-DELGADO, F. & WILHELMS-DICK, D. (2014): The EPICA Dronning Maud Land deep drilling operation. Annals of Glaciology 55, 355-366.

WOLFF, E. W. (1996a): Location, Movement and Reactions of Impurities in Solid Ice, in: Wolff, E. W. & Bales, R. C. (Eds.), Chemical Exchange Between the Atmosphere and Polar Snow. Springer Berlin Heidelberg, Berlin, Heidelberg, pp. 541-560.

WOLFF, E. W. (1996b): The Record of Aerosol Deposited Species in Ice Cores, and Problems of Interpretation, in: Wolff, E. W. & Bales, R. C. (Eds.), Chemical Exchange Between the Atmosphere and Polar Snow. Springer Berlin Heidelberg, pp. 1-17.

WOLFF, E. W., FISCHER, H., FUNDEL, F., RUTH, U., TWARLOH, B., LITTOT, G. C., MULVANEY, R., ROTHLISBERGER, R., DE ANGELIS, M., BOUTRON, C. F., HANSSON, M., JONSELL, U., HUTTERLI, M. A., LAMBERT, F., KAUFMANN, P., STAUFFER, B., STOCKER, T. F., STEFFENSEN, J. P., BIGLER, M., SIGGAARD-ANDERSEN, M. L., UDISTI, R., BECAGLI, S., CASTELLANO, E., SEVERI, M., WAGENBACH, D., BARBANTE, C., GABRIELLI, P. & GASPARI, V. (2006): Southern Ocean sea-ice extent, productivity and iron flux over the past eight glacial cycles. Nature 440, 491-496.

YUAN, F. S., SHENG, Y. W., YAO, T. D., FAN, C. J., LI, J. L., ZHAO, H. & LEI, Y. B. (2011): Evaporative enrichment of oxygen-18 and deuterium in lake waters on the Tibetan Plateau. Journal of Paleolimnology 46, 291-307.

DECLARATION

Declaration acc. to § 10 Paragraph 11 Common Part of the Master Examination Regulations

I hereby declare that I wrote my Master Thesis independently and that I did not use other sources and auxiliary means than the ones indicated.

This Master Thesis is not submitted in another examining procedure.

This proposal is my original work and has not been presented for a degree in any other university.

_____

Place, Date   Signature

APPENDIX

Attached disc contains overview plots (in png-format) of each sampling day of IP1, IP2, IP3 and IP4
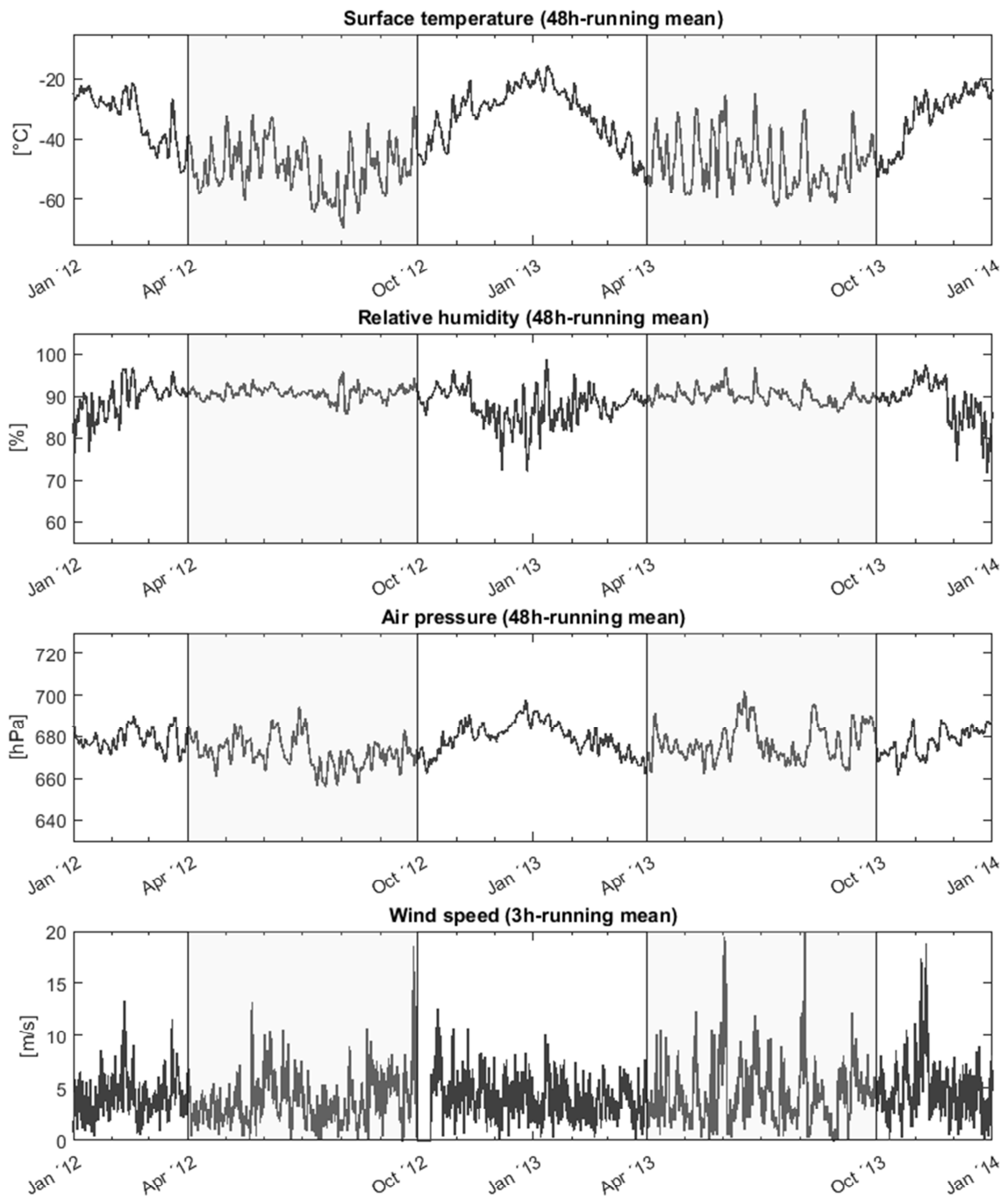
Fig. 32: Three major meteoric parameter surface temperature (upper panel), relative humidity (middle panel) and air pressure (lower panel) measured by the automatic weather station at Kohnen. See unit on the left
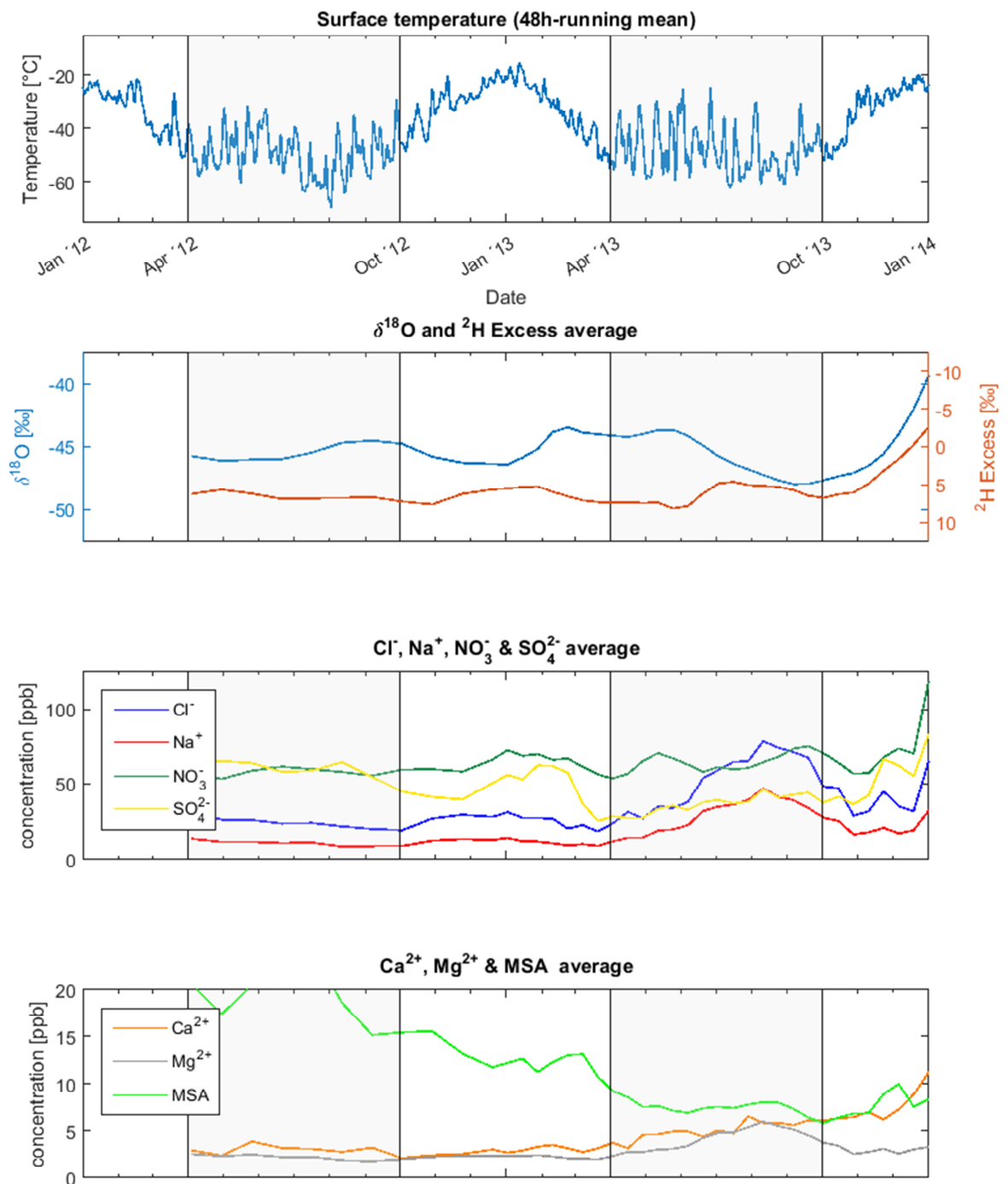
Fig. 33: Linear fit of depth vs. time of spatial average as pointed out in the Discussion
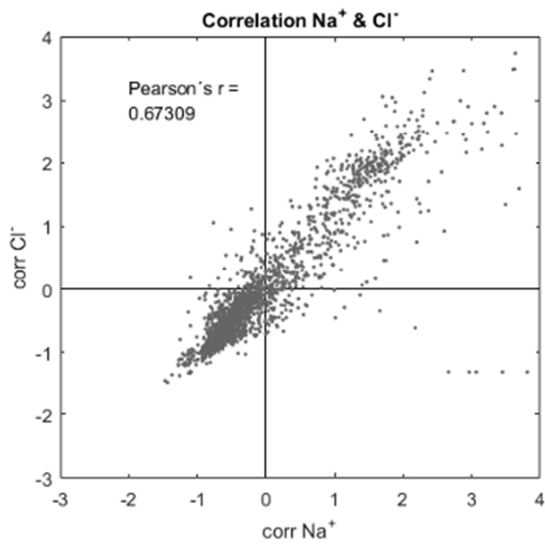
Fig. 34: Linear correlation of Na$^+$ and Cl$^-$

Table 2: Average concentrations [ppb] of aerosols of single snow liner, location means and total mean including standard deviation (SD)

	MSA	SD (MSA)	Cl⁻	SD (Cl⁻)	SO₄²⁻	SD (SO₄²⁻)	NO₃⁻	SD (NO₃⁻)	Na⁺	SD (Na⁺)	Mg²⁺	SD (Mg²⁺)	Ca²⁺	SD (Ca²⁺)
IP1 1204	13.83	11.76	34.57	21.50	41.49	25.97	71.36	18.35	18.78	12.42	4.07	1.92	9.56	11.96
IP1 1206	12.55	11.18	34.38	20.86	42.49	26.33	70.04	19.36	20.09	10.83	4.62	2.25	10.05	5.04
IP1 1207	12.99	11.48	40.08	26.06	43.01	27.30	65.90	15.73	27.68	20.79	4.87	2.51	24.55	16.58
IP1 1208	12.20	7.61	38.51	33.93	45.90	19.50	62.89	21.58	33.68	36.43	7.93	4.55	22.63	21.49
IP1 1209	12.92	9.33	43.49	38.98	44.03	20.88	80.52	28.25	26.05	25.54	6.35	3.50	24.26	15.44
IP1 1211	11.90	12.30	39.68	27.96	46.33	16.37	81.15	22.64	23.01	18.84	5.53	3.08	15.29	11.33
IP1 1212	11.08	9.81	47.08	39.45	48.72	19.68	78.31	26.53	30.70	25.95	8.29	3.92	25.30	18.32
IP1 1214	9.29	4.20	51.35	43.73	44.20	19.54	52.38	14.63	50.68	44.27	7.76	4.33	20.07	14.92
IP1 1216	9.93	5.08	56.00	42.83	49.34	19.44	56.52	16.94	42.63	32.14	7.49	3.83	17.21	12.53
IP1 1217	11.34	6.35	51.44	31.59	47.42	21.31	68.07	25.38	37.28	32.04	8.16	2.70	10.33	8.08
IP1 1218	9.12	6.31	47.06	32.58	53.34	25.95	72.54	23.76	32.63	22.37			11.75	10.51
IP1 1219	9.94	6.12	35.93	22.33	46.10	23.53	73.71	21.35	21.24	11.66	8.16	3.49	17.86	7.94
IP1 1220	9.72	5.76	30.35	19.69	39.46	17.62	63.91	20.12	15.68	10.98	2.72	1.20	3.89	2.25
IP1 1221	9.73	5.67	37.25	23.33	38.77	15.08	81.68	22.60	22.28	14.82	4.07	1.35	4.50	2.93
IP1 1223	8.96	5.23	43.31	28.52	42.49	17.17	83.39	21.97	28.45	21.25	6.95	2.95	6.48	3.87
IP1 1223	9.74	5.80	37.60	24.81	38.67	16.44	69.64	20.62	21.79	17.02	3.66	1.84	7.05	4.24
IP1 1224	9.02	5.38	39.26	28.47	41.81	18.22	68.74	21.14	21.96	17.29	4.72	2.56	5.95	3.43
IP1 1226	9.54	4.22	36.87	30.76	42.73	16.21	66.40	19.47	19.07	15.31	2.75	1.65	3.45	1.39
IP1 1227	8.97	3.98	34.30	28.06	42.77	18.46	63.85	18.70	20.14	18.10	3.23	1.80	5.20	1.87
IP1 1228	8.65	3.34	39.78	30.70	41.41	15.66	65.73	18.04	21.72	17.88	3.53	1.97	6.28	4.46
IP1 1229	8.85	3.41	39.91	30.22	40.90	16.08	62.47	17.85	20.86	18.21	3.29	1.94	4.62	1.93
IP1 1231	7.50	2.89	45.10	33.30	42.25	20.26	66.68	18.18	21.77	17.51	3.42	1.89	4.49	3.01
IP1 0101	8.05	3.47	43.50	38.32	41.07	15.19	58.77	16.87	22.65	20.78	3.27	2.43	3.61	1.78
IP1 0102	7.52	2.96	47.06	40.15	42.78	18.29	61.78	18.28	23.39	20.47	3.27	2.12	5.38	2.83

	MSA	SD (MSA)	Cl^-	SD (Cl^-)	SO_4^{2-}	SD (SO_4^{2-})	NO_3^-	SD (NO_3^-)	Na^+	SD (Na^+)	Mg^{2+}	SD (Mg^{2+})	Ca^{2+}	SD (Ca^{2+})
IP1 0103	5.94	2.47	54.41	37.29	45.76	21.06	64.11	18.21	33.90	30.04	6.93	2.22	5.77	7.99
IP1 0104	8.01	3.04	49.19	37.37	42.09	18.40	61.46	17.04	24.73	20.80	3.22	2.36	3.45	1.54
IP1 0106	6.95	5.07	52.14	39.48	44.90	20.14	67.90	21.13	26.09	20.01	5.67	1.61	6.26	3.17
IP1 0107	8.29	5.49	48.81	32.61	48.14	23.78	68.41	22.58	24.65	18.95	3.48	2.15	4.70	2.09
IP1 0108	8.77	4.61	43.90	33.54	48.90	25.39	69.69	19.45	27.05	26.80	3.02	1.78	4.15	1.73
IP1 0109	8.26	3.90	50.99	31.73	51.30	27.10	70.91	22.69	31.65	28.63	3.49	1.97	5.64	2.93
IP1 0111	9.88	6.82	46.05	29.92	52.26	28.15	69.64	23.70	22.37	17.64	2.98	2.07	4.05	2.31
IP1 0113	10.10	7.13	45.35	34.44	47.52	25.53	65.82	28.36	23.65	18.50	3.12	1.83	4.66	2.04
IP1 0114	11.79	7.39	43.77	35.99	47.54	24.62	64.82	27.29	21.40	20.24	2.84	2.10	3.94	1.64
IP1 0116	11.37	7.81	42.78	32.89	48.93	22.90	64.18	21.00	19.27	16.61	2.51	1.93	3.24	1.77
IP1 0117	11.12	7.04	38.30	30.90	44.56	20.48	70.97	26.45	18.41	18.37	2.69	2.17	3.91	2.04
IP1 0118	11.63	7.18	39.86	31.36	50.59	24.92	68.18	27.35	20.52	19.36	2.96	2.15	6.06	3.83
IP1 0119	10.91	7.03	49.12	31.75	46.24	19.04	70.04	24.79	26.47	19.01	3.44	2.26	8.61	3.74
IP1 0121	11.19	10.13	40.08	32.09	48.73	24.58	70.14	19.92	19.71	18.53	2.73	2.17	3.04	2.33
IP1 0122	9.91	7.21	37.78	27.38	45.50	18.56	66.20	21.45	19.17	15.60	3.09	1.88	4.46	3.24
IP1 0124	12.12	7.12	33.49	27.90	45.85	18.77	58.53	17.79	15.79	14.38	2.39	1.52	4.50	3.85
IP1 0125	11.98	7.58	31.26	25.61	46.41	17.85	54.66	19.60	13.24	12.77	2.08	1.69	3.66	1.89
IP2 1226	12.69	8.16	24.63	12.56	43.86	25.19	51.30	13.71	11.44	6.09	2.51	0.82	5.13	3.31
IP2 0101	12.06	6.53	29.71	15.64	43.57	26.65	49.20	12.85	13.31	7.47	1.86	0.74	4.31	1.26
IP2 0107	11.44	6.63	27.95	14.76	45.18	30.31	51.80	14.67	13.25	7.50	2.14	0.87	3.56	2.14
IP3 1226	15.93	16.69	35.85	22.22	51.27	22.41	54.78	19.52	17.47	11.27	3.44	1.21	6.98	3.11
IP3 0101	15.90	17.10	37.20	24.16	49.88	22.40	51.78	18.68	17.82	12.36	2.83	1.21	6.43	2.89
IP3 0107	16.07	17.07	36.94	25.01	50.86	22.81	50.95	20.30	18.68	14.46	2.69	1.52	4.92	2.15

	MSA	SD (MSA)	Cl⁻	SD (Cl⁻)	SO₄²⁻	SD (SO₄²⁻)	NO₃⁻	SD (NO₃⁻)	Na⁺	SD (Na⁺)	Mg²⁺	SD (Mg²⁺)	Ca²⁺	SD (Ca²⁺)
IP4 1226	8.69	2.80	45.56	35.01	54.65	23.52	67.74	23.98	23.16	18.94	3.63	2.18	6.86	1.92
IP4 0101	7.84	2.80	47.77	35.32	56.01	28.42	62.47	16.65	27.69	25.48	3.96	2.12	7.08	2.00
IP4 0107	7.67	2.89	47.96	34.70	52.14	21.91	62.49	16.89	24.59	18.37	4.00	1.81	4.89	2.58
IP1 mean	10.02	6.96	42.39	32.18	45.15	21.11	67.63	22.26	24.57	22.31	4.33	3.06	8.33	9.85
IP2 mean	12.06	7.10	27.43	14.41	44.21	27.24	50.77	13.70	12.67	7.04	2.17	0.85	4.33	2.45
IP3 mean	15.96	16.81	36.66	23.63	50.67	22.36	52.50	19.42	17.99	12.67	2.99	1.35	6.11	2.86
IP4 mean	8.07	2.84	47.10	34.73	54.27	24.61	64.24	19.48	25.15	21.08	3.86	2.03	6.27	2.39
IP1 - IP4 mean	11.53	3.38	38.39	8.46	48.57	4.75	58.79	8.40	20.09	5.92	3.34	0.96	6.26	1.64

Table 3: Average values of density [g cm^{-3}] and isotopic measurements [‰] of single snow liner, location means and total mean including standard deviation (SD)

	ρ	SD (ρ)		δ^{18}O	SD (δ^{18}O)	δ^{2}H	SD (δ^{2}H)	^{2}H ex	SD (^{2}H ex)
IP1 1204	0.36	0.04		-45.42	2.53	-355.97	19.71	7.35	2.88
IP1 1206	0.36	0.04		-44.93	2.43	-352.18	19.38	7.23	3.15
IP1 1207	0.35	0.04		-44.91	2.54	-351.95	20.37	7.32	3.10
IP1 1208	0.37	0.05		-45.94	2.48	-362.23	18.25	5.31	3.08
IP1 1209	0.33	0.05		-45.38	3.30	-356.31	27.45	6.70	3.57
IP1 1211	0.37	0.04		-45.45	3.94	-358.51	30.68	5.12	3.21
IP1 1212	0.37	0.06		-45.19	3.30	-356.94	26.14	4.61	3.48
IP1 1214	0.37	0.04		-44.49	3.82	-349.98	30.23	5.92	3.37
IP1 1216	0.38	0.05		-45.25	4.05	-356.00	31.22	5.97	3.86
IP1 1217	0.38	0.05		-45.49	3.75	-357.50	28.38	6.39	3.85
IP1 1218	0.37	0.04		-45.77	3.72	-359.06	28.33	7.13	4.03
IP1 1219	0.37	0.05		-45.43	3.54	-356.32	27.64	7.12	3.09
IP1 1220				-45.17	3.21	-354.77	24.83	6.60	2.86
IP1 1221	0.37	0.04		-45.08	3.25	-353.59	25.01	7.04	3.04
IP1 1223	0.34	0.05		-45.45	3.16	-357.43	24.50	6.14	3.15
IP1 1223	0.36	0.05		-45.17	3.32	-354.35	25.43	6.97	3.21
IP1 1224	0.36	0.04		-45.54	3.32	-358.09	25.87	6.21	3.70
IP1 1226	0.34	0.05		-45.03	2.53	-353.96	19.20	6.31	3.33
IP1 1227	0.37	0.03		-45.59	3.22	-358.91	25.14	5.80	3.51
IP1 1228	0.38	0.05		-45.44	3.37	-358.28	26.29	5.24	3.44
IP1 1229	0.37	0.05		-45.48	3.36	-359.02	26.18	4.78	3.43
IP1 1231	0.38	0.07							
IP1 0101	0.39	0.06		-45.19	3.07	-356.98	24.44	4.56	3.16
IP1 0102	0.39	0.06		-44.78	3.79	-353.76	29.95	4.50	3.16

	ρ	SD (ρ)		$\delta^{18}O$	SD ($\delta^{18}O$)	δ^2H	SD (δ^2H)	^2H ex	SD (^2H ex)
IP1 0103	0.38	0.05							
IP1 0104	0.38	0.05		-45.19	3.64	-356.98	28.98	4.52	3.18
IP1 0106	0.40	0.06		-45.32	3.57	-357.66	28.66	4.90	3.90
IP1 0107	0.38	0.05		-46.19	4.04	-365.46	30.56	4.03	3.88
IP1 0108	0.37	0.05		-45.23	3.43	-357.89	27.46	3.95	3.89
IP1 0109	0.37	0.05		-45.80	3.71	-361.44	28.87	4.99	3.57
IP1 0111	0.37	0.04		-45.77	3.31	-362.09	26.91	4.08	3.35
IP1 0113	0.37	0.04		-45.49	2.60	-359.16	21.07	4.74	3.05
IP1 0114	0.37	0.04		-45.33	2.60	-357.29	20.91	5.38	3.28
IP1 0116	0.34	0.05		-45.46	3.04	-358.09	23.54	5.60	3.19
IP1 0117	0.33	0.07		-45.60	2.95	-359.30	23.13	5.49	3.39
IP1 0118	0.36	0.05		-45.38	2.61	-357.75	20.57	5.28	2.85
IP1 0119	0.34	0.07		-45.11	2.70	-355.54	21.21	5.30	3.06
IP1 0121	0.36	0.04		-45.75	3.49	-360.37	26.59	5.60	3.00
IP1 0122	0.36	0.05		-46.34	1.84	-361.61	15.07	9.07	0.38
IP1 0124	0.37	0.04		-45.33	2.84	-356.73	22.13	5.90	3.48
IP1 0125				-45.57	2.71	-359.28	21.27	5.31	3.80
IP2 1226	0.35	0.05		-45.37	2.86	-357.36	22.44	5.59	3.68
IP2 0101	0.36	0.05		-44.24	1.66	-343.55	12.92	10.39	4.61
IP2 0107	0.36	0.03		-43.97	1.63	-345.24	12.54	6.55	3.67
IP3 1226	0.35	0.04		-44.96	3.14	-355.82	26.64	3.83	3.19
IP3 0101	0.35	0.05		-44.96	3.48	-354.56	29.00	5.14	3.41
IP3 0107	0.36	0.05		-45.24	3.14	-356.99	26.16	4.89	3.14

	ρ	SD (ρ)		$\delta^{18}O$	SD ($\delta^{18}O$)	δ^2H	SD (δ^2H)	^2H ex	SD (^2H ex)
IP4 1226	0.36	0.05		-46.53	2.54	-367.56	18.15	4.68	3.32
IP4 0101	0.35	0.05		-46.39	2.39	-366.06	17.58	5.06	2.95
IP4 0107	0.37	0.04		-45.27	1.91	-357.55	14.58	4.60	2.38
IP1 mean	0.37	0.05		-45.36	3.22	-357.21	25.21	5.70	3.46
IP2 mean	0.36	0.04		-44.48	2.15	-348.26	17.17	7.61	4.50
IP3 mean	0.35	0.05		-45.05	3.23	-355.79	27.08	4.62	3.27
IP4 mean	0.36	0.05		-46.06	2.34	-363.68	17.27	4.77	2.89
IP1 - IP4 mean	0.36	0.01		-45.24	0.66	-356.24	6.33	5.68	1.37

Table 4: Spatial average of ions [ppb] calculated from five samples (s. Fig. 24)

	MSA	SD (MSA)	Cl⁻	SD (Cl⁻)	SO₄²⁻	SD (SO₄²⁻)	NO₃⁻	SD (NO₃⁻)	Na⁺	SD (Na⁺)	Mg²⁺	SD (Mg²⁺)	Ca²⁺	SD (Ca²⁺)
Spat_av_1	8.35	3.01	65.55	37.79	83.25	16.00	118.74	32.47	32.21	12.31	3.30	1.05	11.26	1.80
Spat_av_2	7.55	2.98	31.60	8.70	55.22	4.43	70.34	33.05	19.16	4.50	3.06	1.22	8.90	1.08
Spat_av_3	10.03	4.87	34.98	16.84	62.32	25.40	73.68	39.07	16.92	6.93	2.56	0.91	7.27	2.67
Spat_av_4	8.91	4.10	44.90	18.75	66.67	20.63	67.86	39.92	20.73	8.26	3.12	0.88	6.19	1.28
Spat_av_5	6.88	1.56	31.57	18.75	42.26	12.72	57.21	32.40	17.75	8.80	2.77	1.26	6.99	2.11
Spat_av_6	6.84	1.38	28.68	16.08	36.35	9.96	56.79	34.02	16.30	8.02	2.54	1.06	6.46	2.90
Spat_av_7	6.41	1.59	47.10	35.36	41.40	20.58	64.22	36.65	25.20	20.55	3.43	1.81	6.34	2.14
Spat_av_8	5.83	2.31	48.20	36.31	37.39	10.69	70.58	36.43	27.39	21.00	3.77	2.14	6.07	1.97
Spat_av_9	6.41	2.60	67.43	38.01	44.14	15.90	75.27	34.82	33.71	19.53	4.54	2.12	6.11	2.05
Spat_av_10	7.35	2.68	71.30	39.30	42.76	12.68	73.51	27.43	39.05	21.93	5.16	2.52	5.59	1.99
Spat_av_11	7.99	2.58	74.26	43.23	40.86	12.22	68.20	21.96	41.25	26.59	5.51	3.10	5.84	2.11
Spat_av_12	8.08	1.59	78.56	47.48	46.17	18.23	64.56	14.61	46.80	27.08	5.98	3.05	5.84	2.15
Spat_av_13	7.79	2.16	65.24	42.15	37.88	12.65	60.67	12.33	39.18	23.16	5.38	2.89	6.54	2.59
Spat_av_14	7.42	1.86	64.71	39.87	36.75	13.28	59.87	9.62	36.02	22.49	4.88	3.08	4.73	2.90
Spat_av_15	7.56	1.46	59.34	34.31	39.18	15.88	61.29	7.97	34.71	20.81	4.81	2.78	5.07	2.67
Spat_av_16	7.40	1.33	53.82	28.99	37.67	13.12	58.12	11.84	31.78	17.48	4.27	2.39	4.40	2.05
Spat_av_17	6.91	0.85	37.95	10.04	32.58	13.63	62.94	13.75	22.46	9.11	3.42	1.40	4.94	1.65
Spat_av_18	7.15	1.76	33.74	11.22	35.43	22.70	67.06	18.36	19.59	6.23	3.09	1.31	4.94	2.31
Spat_av_19	7.65	3.31	34.84	17.86	33.18	19.20	70.66	16.13	18.90	9.85	3.04	1.50	4.65	2.34
Spat_av_20	7.52	3.16	26.88	20.19	27.33	9.42	65.37	23.49	14.21	8.49	2.76	1.17	4.60	1.68
Spat_av_21	8.58	2.30	31.27	22.29	27.15	4.61	56.83	15.85	14.22	10.55	2.80	1.24	3.17	2.65
Spat_av_22	9.26	3.60	23.75	10.45	28.29	4.63	53.66	8.00	11.82	5.10	2.33	0.73	3.75	1.92
Spat_av_23	10.78	4.90	18.29	4.41	25.22	6.43	56.35	10.76	8.76	2.92	1.98	0.92	3.16	1.43
Spat_av_24	13.14	5.82	22.49	10.55	36.81	20.55	61.50	7.79	9.97	6.27	2.05	1.13	2.75	1.47

	MSA	SD (MSA)	Cl⁻	SD (Cl⁻)	SO_4^{2-}	SD (SO_4^{2-})	NO_3^-	SD (NO_3^-)	Na^+	SD (Na^+)	Mg^{2+}	SD (Mg^{2+})	Ca^{2+}	SD (Ca^{2+})
Spat_av_25	13.04	6.83	20.24	5.93	57.44	44.26	66.95	13.64	9.05	3.09	2.10	0.85	3.16	1.87
Spat_av_26	12.31	4.90	26.91	12.06	61.97	53.45	66.20	17.92	10.58	4.45	2.28	0.72	3.52	2.32
Spat_av_27	11.24	4.45	27.14	14.10	62.38	39.22	69.95	11.03	11.65	4.78	2.42	0.87	3.33	1.93
Spat_av_28	12.69	5.97	27.28	17.15	52.99	17.92	68.84	17.42	11.78	7.17	2.32	0.93	2.92	1.39
Spat_av_29	12.23	5.08	31.03	9.80	56.08	15.89	72.63	29.16	14.01	3.43	2.31	0.34	2.69	0.63
Spat_av_30	11.76	5.24	27.95	10.05	50.52	19.42	66.30	29.39	12.65	3.76	2.33	0.26	3.02	1.13
Spat_av_31	13.20	5.80	29.32	15.29	39.48	7.87	58.32	27.08	13.28	6.97	2.32	0.58	2.56	1.46
Spat_av_32	15.53	10.25	26.90	18.85	41.17	9.94	59.87	30.89	12.27	9.62	2.24	1.20	2.42	1.92
Spat_av_33	15.42	10.14	19.10	9.42	44.73	17.95	59.54	29.32	8.76	6.65	1.99	1.23	2.10	1.80
Spat_av_34	15.14	11.64	19.91	11.42	54.72	31.12	55.52	24.20	8.72	5.16	1.80	0.86	3.23	3.03
Spat_av_35	18.57	14.70	21.64	18.55	64.67	39.22	57.97	25.90	8.39	6.83	1.88	0.95	2.77	2.01
Spat_av_36	24.25	25.12	23.89	13.05	58.86	14.77	59.89	16.43	11.02	7.60	2.24	1.35	3.09	1.49
Spat_av_37	25.04	29.90	23.55	16.89	58.08	12.18	61.59	15.14	10.67	9.58	2.22	1.58	3.18	1.48
Spat_av_38	20.45	23.03	25.92	13.00	64.02	25.51	58.83	8.71	11.49	7.59	2.49	1.29	3.89	2.37
Spat_av_39	17.37	11.10	26.13	10.53	65.38	30.73	53.31	14.12	11.40	5.30	2.31	0.80	2.38	1.18
Spat_av_40	20.54	18.87	31.01	11.31	64.49	36.93	58.43	24.86	13.58	5.75	2.55	0.61	2.95	1.50

Table 5: Spatial average of density [g cm⁻³] and isotopes [‰] calculated from five samples (s. Fig. 24)

	ρ	SD (ρ)		$\delta^{18}O$	SD ($\delta^{18}O$)	δ^2H	SD (δ^2H)	^2H ex	SD (^2H ex)
Spat_av_1	0.25	0.04		-39.35	0.93	-317.42	8.97	-2.59	1.79
Spat_av_2	0.31	0.05		-42.02	1.88	-336.38	15.45	-0.26	1.49
Spat_av_3	0.34	0.05		-44.02	1.76	-350.52	15.62	1.65	1.74
Spat_av_4	0.35	0.02		-45.57	1.76	-361.40	14.02	3.16	1.71
Spat_av_5	0.30	0.03		-46.51	1.86	-367.24	13.43	4.85	2.02
Spat_av_6	0.34	0.04		-47.07	2.12	-370.52	16.09	6.05	2.06
Spat_av_7	0.29	0.01		-47.33	2.31	-372.33	17.81	6.30	2.54
Spat_av_8	0.37	0.04		-47.66	2.30	-374.50	18.01	6.78	2.59
Spat_av_9	0.36	0.03		-47.93	2.33	-376.99	18.34	6.49	2.87
Spat_av_10	0.39	0.03		-47.95	2.31	-377.88	18.81	5.71	3.05
Spat_av_11	0.34	0.03		-47.65	2.47	-375.92	20.42	5.29	2.70
Spat_av_12	0.39	0.02		-47.22	2.82	-372.63	23.82	5.17	2.47
Spat_av_13	0.37	0.02		-46.78	3.09	-369.21	26.53	5.05	2.59
Spat_av_14	0.41	0.03		-46.35	3.06	-366.16	26.55	4.63	2.93
Spat_av_15	0.39	0.03		-45.74	2.69	-361.08	24.16	4.84	3.03
Spat_av_16	0.39	0.02		-44.92	2.24	-353.21	21.02	6.17	3.46
Spat_av_17	0.37	0.02		-44.16	1.52	-345.39	15.18	7.87	3.30
Spat_av_18	0.39	0.04		-43.68	0.38	-341.23	5.03	8.20	2.61
Spat_av_19	0.37	0.02		-43.69	1.07	-342.12	9.32	7.40	3.27
Spat_av_20	0.39	0.02		-44.01	1.87	-344.58	16.28	7.47	3.31
Spat_av_21	0.40	0.03		-44.24	2.26	-346.57	19.02	7.37	2.46
Spat_av_22	0.37	0.03		-44.14	2.20	-345.74	18.43	7.38	1.71
Spat_av_23	0.35	0.03		-44.03	1.89	-344.89	15.60	7.34	0.96
Spat_av_24	0.42	0.02		-43.89	2.00	-343.99	15.76	7.11	0.70

	ρ	SD (ρ)		$\delta^{18}O$	SD ($\delta^{18}O$)	δ^2H	SD (δ^2H)	^2H ex	SD (^2H ex)
Spat_av_25	0.35	0.03		-43.48	2.60	-341.25	20.42	6.57	1.61
Spat_av_26	0.40	0.02		-43.86	2.95	-344.91	22.94	5.96	2.62
Spat_av_27	0.34	0.04		-45.19	3.30	-356.28	24.16	5.23	3.70
Spat_av_28	0.34	0.04		-45.86	2.48	-361.59	18.13	5.31	3.53
Spat_av_29	0.36	0.04		-46.41	3.17	-365.76	23.53	5.51	3.20
Spat_av_30	0.39	0.03		-46.37	3.74	-365.34	27.05	5.64	3.63
Spat_av_31	0.36	0.02		-46.28	3.41	-363.96	24.32	6.24	4.39
Spat_av_32	0.36	0.02		-45.80	3.49	-358.73	27.53	7.66	3.83
Spat_av_33	0.40	0.03		-44.78	3.87	-351.00	29.32	7.26	2.92
Spat_av_34	0.37	0.07		-44.52	2.31	-349.50	17.09	6.67	3.64
Spat_av_35	0.35	0.02		-44.69	3.17	-350.77	25.40	6.79	2.62
Spat_av_36	0.35	0.05		-45.48	4.73	-357.01	37.29	6.83	3.49
Spat_av_37	0.35	0.01		-45.97	5.43	-360.86	42.74	6.92	4.21
Spat_av_38	0.36	0.02		-46.03	4.70	-362.01	36.54	6.20	3.54
Spat_av_39	0.37	0.03		-46.13	2.47	-363.37	16.98	5.66	3.77
Spat_av_40	0.35	0.02		-45.74	0.56	-359.71	5.02	6.25	3.42

Table 6: Temporal average of ions [ppb] calculated from five samples along IP1

	MSA	SD (MSA)	Cl⁻	SD (Cl⁻)	SO_4^{2-}	SD (SO_4^{2-})	NO_3^-	SD (NO_3^-)	Na^+	SD (Na^+)	Mg^{2+}	SD (Mg^{2+})	Ca^{2+}	SD (Ca^{2+})
Temp_av_1	8.47	3.64	65.96	18.40	96.31	8.68	102.75	34.18	31.05	17.96	4.96	3.90	14.19	10.92
Temp_av_2	8.16	4.01	40.17	15.96	61.91	14.71	94.89	45.78	22.41	5.08	4.83	3.06	29.36	27.23
Temp_av_3	8.44	5.62	35.73	12.69	59.14	33.27	81.56	27.66	17.06	5.63	3.78	2.15	19.51	16.22
Temp_av_4	8.22	2.48	35.66	19.61	61.33	9.83	76.15	28.26	19.20	11.73	3.53	2.09	12.85	9.84
Temp_av_5	7.93	3.04	37.46	16.73	47.35	13.95	59.94	15.74	19.37	9.66	3.27	1.67	10.07	7.41
Temp_av_6	7.07	2.38	40.17	14.94	53.80	23.69	66.60	21.57	20.90	8.49	3.45	1.72	9.27	6.81
Temp_av_7	6.70	2.60	38.84	15.62	49.44	21.39	68.98	24.12	20.94	9.00	3.62	1.98	9.32	7.01
Temp_av_8	6.81	2.91	42.39	16.44	41.94	13.27	61.61	18.95	17.74	11.06	3.19	2.12	7.38	6.79
Temp_av_9	7.78	4.11	45.45	12.21	37.31	15.22	61.95	25.83	23.17	8.78	3.22	2.10	7.39	5.96
Temp_av_10	8.88	3.47	61.07	34.61	43.88	19.81	66.02	20.91	26.27	18.48	4.01	2.91	10.98	9.11
Temp_av_11	9.40	0.90	82.94	44.92	47.30	15.36	67.74	11.73	43.78	23.37	6.15	3.68	9.00	4.84
Temp_av_12	9.03	1.38	78.06	24.41	49.45	13.74	66.01	5.81	46.73	16.60	6.58	2.16	7.74	5.09
Temp_av_13	8.97	0.99	75.64	39.12	40.26	15.28	59.15	6.41	43.84	18.96	6.32	1.63	7.24	5.88
Temp_av_14	8.60	1.20	71.24	40.86	38.34	15.91	59.20	7.49	41.79	22.33	6.00	1.90	7.90	7.18
Temp_av_15	8.68	1.36	71.62	39.83	37.85	14.50	59.48	6.48	36.83	18.00	5.12	1.67	8.05	8.41
Temp_av_16	9.32	1.64	70.97	38.51	38.68	13.50	61.31	6.40	40.48	20.18	5.89	1.95	9.28	8.03
Temp_av_17	9.32	1.79	59.04	33.08	38.41	14.72	61.92	7.60	33.64	17.72	5.48	2.07	8.74	7.99
Temp_av_18	8.93	2.73	48.27	32.86	33.99	11.87	67.28	8.25	28.53	19.32	4.96	2.29	9.33	8.16
Temp_av_19	8.30	3.91	33.03	26.60	30.25	8.08	75.19	15.52	20.03	14.84	4.01	2.18	7.41	7.41
Temp_av_20	8.01	5.64	19.74	8.24	27.16	6.42	73.32	11.68	12.10	5.82	2.92	1.47	6.75	6.22
Temp_av_21	8.77	7.06	18.27	3.73	24.39	3.73	69.26	25.22	10.04	3.36	2.60	1.53	6.39	7.17
Temp_av_22	9.74	7.79	20.55	7.22	25.83	6.07	68.44	17.97	13.31	8.69	3.11	2.36	8.05	10.54
Temp_av_23	10.96	6.84	18.44	5.28	25.50	7.49	59.07	17.20	10.88	4.23	3.02	2.33	7.85	8.63
Temp_av_24	10.98	5.94	14.54	2.94	25.47	6.46	58.21	15.12	8.22	3.04	2.92	2.49	6.67	6.46

	MSA	SD (MSA)	Cl⁻	SD (Cl⁻)	SO₄²⁻	SD (SO₄²⁻)	NO₃⁻	SD (NO₃⁻)	Na⁺	SD (Na⁺)	Mg²⁺	SD (Mg²⁺)	Ca²⁺	SD (Ca²⁺)
Temp_av_25	13.37	6.36	22.73	9.00	29.29	8.87	63.56	16.89	11.49	4.67	3.24	2.85	7.51	8.53
Temp_av_26	15.80	4.79	23.93	7.13	31.10	4.60	73.69	19.22	12.34	4.50	3.06	2.24	6.62	6.80
Temp_av_27	18.12	4.08	21.12	3.96	38.93	14.61	80.80	22.02	10.53	2.55	2.99	2.05	6.33	5.60
Temp_av_28	16.39	3.27	23.68	10.58	63.26	39.80	82.66	24.43	9.61	2.32	3.02	2.16	7.12	5.59
Temp_av_29	15.30	5.40	27.19	10.02	68.35	38.08	86.22	19.83	10.03	3.02	3.22	2.42	4.61	2.05
Temp_av_30	13.04	5.43	31.30	14.39	68.36	35.52	80.83	21.30	12.33	5.03	3.29	1.78	6.39	3.10
Temp_av_31	12.51	6.72	24.95	8.91	58.20	40.08	69.17	21.64	11.88	3.84	3.35	1.86	5.50	3.09
Temp_av_32	12.46	10.63	25.93	6.54	58.79	24.21	66.06	24.74	12.63	4.27	5.19	6.09	6.58	4.66
Temp_av_33	7.81	1.74	22.57	5.03	49.75	23.57	62.69	23.32	10.66	1.56	4.74	5.95	5.16	4.78
Temp_av_34	7.01	2.53	22.21	4.27	41.41	12.79	52.32	14.04	11.26	3.23	4.44	4.65	3.90	3.18
Temp_av_35	7.70	2.69	27.62	7.76	33.90	6.05	46.97	8.68	13.59	4.50	4.59	4.41	4.65	2.23
Temp_av_36	8.46	2.87	25.13	2.62	32.27	12.12	45.24	9.67	12.83	0.91	4.17	3.77	4.14	1.72
Temp_av_37	10.68	4.33	25.68	6.70	35.58	11.96	51.49	11.01	10.41	4.52	3.67	3.96	3.25	1.43
Temp_av_38	14.51	8.96	26.00	14.35	42.55	12.20	61.42	15.49	12.57	7.10	4.46	4.38	3.54	1.69
Temp_av_39	21.48	14.66	24.15	4.69	55.38	26.38	66.86	16.06	11.80	3.77	5.08	5.57	4.05	1.91
Temp_av_40	34.88	24.88	20.13	5.68	70.32	24.43	65.17	12.04	10.04	3.91	5.72	7.11	4.75	3.60

Table 7: Temporal average of density [g cm^{-3}] and isotopes [‰] calculated from five samples along IP1

	ρ	SD (ρ)		δ^{18}O	SD (δ^{18}O)	δ^{2}H	SD (δ^{2}H)	^{2}H ex	SD (^{2}H ex)
Temp_av_1	0.24	0.04		-40.55	2.88	-326.43	21.43	-2.03	2.92
Temp_av_2	0.34	0.10		-41.61	1.75	-332.79	13.62	0.11	1.84
Temp_av_3	0.30	0.07		-43.84	2.09	-347.24	18.69	3.50	2.51
Temp_av_4	0.34	0.03		-45.73	1.67	-361.58	14.95	4.28	2.05
Temp_av_5	0.32	0.02		-47.30	1.66	-374.15	14.45	4.22	1.78
Temp_av_6	0.35	0.03		-48.58	1.64	-383.72	14.98	4.90	2.48
Temp_av_7	0.31	0.02		-49.09	1.75	-387.07	15.39	5.68	1.84
Temp_av_8	0.34	0.02		-48.95	1.52	-384.99	12.73	6.62	1.05
Temp_av_9	0.33	0.03		-48.56	1.28	-380.92	9.81	7.59	1.32
Temp_av_10	0.33	0.02		-48.18	1.22	-378.03	8.99	7.42	2.00
Temp_av_11	0.41	0.06		-47.58	0.96	-374.42	7.64	6.21	1.81
Temp_av_12	0.38	0.02		-46.89	1.11	-369.85	10.44	5.26	1.92
Temp_av_13	0.40	0.04		-46.25	1.78	-365.12	17.38	4.88	3.20
Temp_av_14	0.41	0.02		-45.93	2.02	-363.12	19.71	4.35	3.57
Temp_av_15	0.41	0.02		-46.00	1.71	-364.09	16.80	3.89	3.20
Temp_av_16	0.40	0.03		-46.23	1.23	-365.65	12.65	4.23	3.39
Temp_av_17	0.41	0.02		-46.17	1.29	-364.34	11.63	5.01	3.15
Temp_av_18	0.38	0.02		-45.60	1.76	-359.33	14.88	5.47	2.43
Temp_av_19	0.39	0.03		-44.63	2.16	-350.09	18.22	6.93	2.09
Temp_av_20	0.37	0.04		-43.47	2.06	-339.45	16.89	8.32	1.49
Temp_av_21	0.40	0.02		-42.83	2.07	-333.52	16.11	9.13	0.55
Temp_av_22	0.37	0.02		-42.64	2.41	-332.08	18.23	9.03	1.17
Temp_av_23	0.37	0.02		-42.58	2.66	-331.65	19.74	9.01	1.94
Temp_av_24	0.40	0.02		-42.63	2.40	-331.95	18.11	9.10	2.15

	ρ	SD (ρ)		$\delta^{18}O$	SD ($\delta^{18}O$)	δ^2H	SD (δ^2H)	^2H ex	SD (^2H ex)
Temp_av_25	0.38	0.02		-43.36	1.77	-338.00	13.40	8.88	1.92
Temp_av_26	0.38	0.02		-44.55	0.47	-348.18	4.08	8.21	2.04
Temp_av_27	0.35	0.02		-44.87	1.35	-350.96	12.08	7.98	1.73
Temp_av_28	0.38	0.02		-44.04	3.04	-344.93	23.35	7.36	1.36
Temp_av_29	0.39	0.01		-43.14	3.32	-338.95	24.13	6.15	3.25
Temp_av_30	0.38	0.05		-42.86	2.76	-338.00	19.71	4.85	4.05
Temp_av_31	0.39	0.02		-43.68	1.80	-345.63	13.35	3.82	4.37
Temp_av_32	0.34	0.07		-43.65	3.63	-345.93	30.17	3.27	4.08
Temp_av_33	0.35	0.05		-43.98	4.88	-348.96	37.01	2.92	3.01
Temp_av_34	0.36	0.01		-45.75	3.57	-362.10	26.49	3.91	3.10
Temp_av_35	0.34	0.02		-47.66	2.03	-376.10	14.32	5.19	2.72
Temp_av_36	0.37	0.02		-48.92	1.89	-385.15	11.94	6.22	3.47
Temp_av_37	0.37	0.02		-49.17	1.81	-386.32	10.73	7.05	4.24
Temp_av_38	0.37	0.02		-48.76	2.37	-382.52	17.64	7.55	4.43
Temp_av_39	0.38	0.02		-47.73	3.30	-373.61	25.82	8.21	3.60
Temp_av_40	0.38	0.01		-45.41	3.81	-354.07	30.35	9.21	2.65